

HUMA



41st Annual VFS Student Design Competition

Multi-Mission Modular UAS for Disaster Relief

Sponsored by:



Alfred Gessow Rotorcraft Center
Department of Aerospace Engineering
University of Maryland
College Park, MD 20742 U.S.A.



UNIVERSITY OF
MARYLAND



Alfred Gessow Rotorcraft Center
Department of Aerospace Engineering
University of Maryland
College Park, MD 20742

Vivek Uppoor
Graduate Student (Team Lead)
vvuppoor@umd.edu

Batin Bugday
Graduate Student
bugday@umd.edu

Michael Morcos
Graduate Student
mmorcos@umd.edu

Sridatta Satuluri
Graduate Student
satuluri@umd.edu

Dr. Vengalattore Nagaraj
Faculty Advisor
vnagaraj@umd.edu

Logan Swaisgood
Graduate Student
lswaiz@umd.edu

Muneeb Safdar
Graduate Student
msafdar@umd.edu

Victoria Britcher
Graduate Student
vbritche@umd.edu

Dr. Inderjit Chopra
Faculty Advisor
chopra@umd.edu

Dr. Anubhav Datta
Faculty Advisor
datta@umd.edu

ACKNOWLEDGEMENTS

The UMD graduate design team acknowledges the following people for their invaluable discussion, guidance, and support throughout this project.

Industry Professionals

Dr. Andreas Bernhard — Director, Tech Road Maps, Advanced Development Programs, Lockheed Martin Aeronautics

Mr. Eric Greenbaum — Aerospace Engineer, Joby Aviation

University of Maryland Faculty

Prof. James D. Baeder — Igor Sikorsky Distinguished Professor in Rotorcraft, Department of Aerospace Engineering

Prof. Umberto Saetti — Assistant Professor, Department of Aerospace Engineering

Dr. Mrinalgouda Patil — Postdoctoral Research Associate, Department of Aerospace Engineering

Alfred Gessow Rotorcraft Research Center Graduate Students

Spencer Fishman (US Navy Helicopter Pilot)

Matt Arace

Paulo Arias

Nathan O'Brien



Alfred Gessow Rotorcraft Center
Department of Aerospace Engineering
University of Maryland
College Park, MD 20742 U.S.A.

To the Vertical Flight Society:

The members of the University of Maryland Graduate Student Design Team hereby grant VFS full permission to distribute the enclosed Executive Summary and Final Proposal for the 41st Annual Design Competition as they see fit.

Thank you,
The UMD Graduate Design Team

Contents

1	Introduction	3
2	Configuration Selection	4
2.1	Voice of the Customer	4
2.1.1	Design Drivers	4
2.1.2	Analytical Hierarchy Process (AHP)	6
2.2	Candidate Vehicle Configurations	7
2.2.1	Standard Rotorcraft (up to 2 main rotors)	7
2.2.2	Multicopters (3 or more rotors)	9
2.3	Pugh Matrix	10
3	Preliminary Vehicle Sizing	10
3.1	Mission Profiles	10
3.2	Sizing Methodology	11
3.3	Weight Model Validation	12
3.4	Trade Studies	13
3.4.1	Number of Blades	13
3.4.2	Aspect Ratio and Solidity	14
3.4.3	Tip Speed and Disk Loading	15
3.4.4	Wing Parameters	16
3.4.5	Trade Summary	16
3.5	<i>Huma</i> Specifications	17
4	Concept of Operations and Multi-Mission Capability	17
4.1	Modular Add-On Components	17
4.1.1	Center Body Bay	18
4.1.2	Wing Attachment and Removal Mechanism	20
4.1.3	Removable Supply Case	20
4.1.4	Long-Endurance Fuel Tank	21
4.1.5	Procedure for Swapping Modular Add-Ons	21
4.2	Front Payload Bay	22
4.3	Vehicle Storage	23
5	Blade Aerodynamic Design	23
5.1	Design Challenges	24
5.2	An Innovative Methodology	24
5.3	Genetic Algorithm	24
5.4	Aerodynamic Design Objective	24
5.4.1	Design Space	25
5.4.2	Navigating Tradeoffs	25
5.4.3	Optimized rotor geometry	26
5.4.4	Optimized rotor performance	27
6	Blade Structural Design	28
6.1	Structure	29
6.2	Root Flexbeam	29
6.3	Internal Structure, Outboard of the Flexbeam	30
6.4	Blade Manufacturing	31

6.5	Blade Properties	32
6.6	Aeroelastic Stability Analysis	33
6.7	3-D Stress Analysis	34
7	Hub Design	35
7.1	Hub Selection	35
7.2	Hub Assembly	36
7.3	Swashplate Design	36
7.3.1	Swashplate Actuators	38
8	Wing Design	38
8.1	Lift Sharing and Shaft Tilt Angle	38
8.2	Airfoil Selection	38
8.3	Geometric Considerations	39
8.4	Wing Structural Design	39
8.5	Finite Element Analysis	40
8.6	Aeroelastic Analysis	41
9	Tail Rotor Design	42
9.1	Tail Rotor Sizing	42
9.1.1	Diameter	42
9.1.2	Solidity	42
9.1.3	Tip Speed	43
9.2	Aerodynamic Design	43
9.3	Tail Rotor Mounting	43
9.4	Hub Design	44
10	Airframe Design	45
10.1	Overview	45
10.2	Internal Layout	45
10.3	Marinization	47
10.4	Fuselage Structure	47
10.4.1	Load Paths	48
10.4.2	Airframe Material Selection	48
10.5	Lift Rod Design	48
10.6	Empennage Design	49
10.6.1	Horizontal Stabilizer	49
10.6.2	Vertical Stabilizer	49
10.7	Landing Gear	49
10.7.1	Configuration Trade Study	50
10.7.2	Landing Gear Geometry	50
10.7.3	Landing Gear Static Structural Analysis	51
11	Powerplant	51
11.1	Powerplant Selection	51
11.1.1	Turboshaft	51
11.1.2	Piston Engine	52
11.1.3	Engine-Generator and Turbogenerator	53
11.1.4	Hydrogen Fuel Cell	54
11.2	Powerplant Performance	54

11.3 Powerplant Installation and Operation	55
11.4 Fuel System	55
12 Transmission Design	57
12.1 System Overview	57
12.2 Drivebelt Design	58
12.3 Main Rotor Transmission	58
12.3.1 Main Rotor Gearbox	58
12.3.2 Drive Belts and Shafts	59
12.4 Tail Rotor Transmission	60
12.4.1 Tail Rotor Gearbox	61
12.4.2 Drive Belts and Shafts	61
13 Avionics System	62
13.1 Components	62
13.1.1 Sensors	63
13.1.2 Processing and Control	64
13.1.3 Communications	64
13.2 Autonomy	65
13.2.1 State Estimation	65
13.2.2 Ground and Ship Landing	65
13.2.3 Sense-and-Avoid	67
13.2.4 Optical Navigation	68
13.2.5 Optional Remote Piloting	68
13.3 Avionics Integration	68
13.3.1 Data Connections	68
13.3.2 Power Distribution	68
13.3.3 Mounting and Vibration Isolation	68
13.4 Weight, Power, and Cost Summary	69
13.5 Health and Usage Monitoring System	70
13.6 Electrical Power Components	70
14 Weight and Balance	71
15 Flight Dynamics and Controls	72
15.1 Flight Dynamics Simulation Model	73
15.2 Trim Analysis	74
15.3 Stability Analysis	76
15.4 Flight Control Design	80
15.4.1 Controller Architecture	80
15.4.2 Closed Loop Stability and Control	83
15.4.3 Wind and Gust Rejection Simulation	83
16 Vehicle Performance	87
16.1 Component Wise Drag Estimation	87
16.1.1 Fuselage	88
16.1.2 Hub Fairing	90
16.1.3 Wing and Empennage	91
16.1.4 Landing Gear	92
16.2 Hover Download	92

16.3 Airframe Aerodynamic Metrics	93
16.4 Hover Performance	93
16.5 Forward Flight Performance	94
16.6 Range and Endurance	95
16.7 Mission-specific Performance	95
17 Safety Considerations	95
17.1 Engine and Powerplant	95
17.2 Avionics and Electrical	96
17.2.1 Processing Component Failures	96
17.2.2 Sensor Failures	97
17.2.3 Alternator Failure	97
17.3 Additional Safety Features	97
18 Acoustics	97
19 Cost Analysis	98
19.1 Purchase Price	98
19.2 Maintenance Cost	99
19.3 Operational Cost	99
20 Additional Mission Capabilities	99
20.1 Short-Range Deliveries	99
20.2 Monitoring and Surveillance	99
20.3 Additional Modular Equipment	100
21 Summary	100

List of Figures

1.1	<i>Huma</i> operating as an aerial cell relay during a wildfire.	3
2.1	Standard Rotorcraft Configurations Considered	8
2.2	Multirotor Configurations Considered	9
3.1	Mission Profiles	12
3.2	Flowchart of Vehicle Sizing Procedure	13
3.3	Trade study for number of blades	14
3.4	Trade study for blade aspect ratio and solidity	14
3.5	Trade study for main rotor tip speed.	15
3.6	Rotor diameter vs disk loading.	15
3.7	Wing parameters trade study.	16
3.8	Power versus velocity	16
4.1	Center body bay for mounting modular add-ons.	19
4.2	Wing attachment interface inside adapter with locking pins.	20
4.3	Long endurance add-on assembly procedure.	22
4.4	Supplies delivery add-on assembly procedure.	22
4.5	The front payload bay, opened while preparing for long endurance mission.	23
4.6	Hangar storage arrangement, lift compound configuration.	23
4.7	Hangar storage arrangement, SMR configuration.	24
5.1	Genetic Algorithm architecture and sample results	25
5.2	Optimization of competing objectives for multi-configuration design	26
5.3	Pareto Frontier with best designs across generations	27
5.4	Top 11 designs and the selected best	27
5.5	Pareto Frontier: Best weight fraction selection	28
5.6	Optimized main rotor geometry	28
5.7	Profile of the optimized main rotor	29
6.1	Main rotor blade top view	30
6.2	Cross-section of the main rotor blade	30
6.3	Flexbeam to blade transition	31
6.4	Main rotor sectional properties; Ω is rotor speed in hover	32
6.5	Fan plot of the main rotor	33
6.6	Pitch-flap and flap-lag aeroelastic stability margins	34
6.7	3-D Stresses analysis in forward flight (80 knots) using X3D	35
7.1	Hingeless hub assembly	37
7.2	Rotor hub and swashplate exploded views	37
7.3	Swashplate actuators attached to the shaft support collar	38
8.1	Wing airfoil selection	39
8.2	Performance curves of selected airfoils	40
8.3	Finite element analysis of Composite wing spar	41
8.4	Aeroelastic analysis of the wings	41
9.1	Tail rotor mass versus blade loading	42
9.2	Tail rotor planform	43
9.3	Tail rotor optimization	43
9.4	Tail rotor vertical placement	44
9.5	Tail rotor hub components	45
10.1	von-Mises stresses of airframe with load paths	48
10.2	<i>Huma</i> empennage components	49
10.3	Landing Gear Stability Angles	50

10.4	von-Mises stress analysis of landing gear	51
11.1	Candidate turboshaft engines	52
11.2	Candidate piston engines	53
11.3	Candidate engine generators and turbogenerators	54
11.4	Engine SFC vs. Engine Operating Power	55
11.5	UTP50R installation with mount and intake manifold	56
11.6	<i>Huma</i> exhaust manifold	56
12.1	Layout of the main transmission	57
12.2	Interior of the main gearbox	60
12.3	Tail transmission assembly	61
13.1	External sensors.	63
13.2	Processing and communications components.	64
13.3	Avionics and autonomy architecture.	65
13.4	Feature-based ship-deck pose estimation algorithm.	66
13.5	Object detection and optical navigation algorithms.	67
13.6	Diagram showing the placement of avionics and electrical components.	69
14.1	Study of Longitudinal CG Travel	72
14.2	Study of Vertical and Lateral CG Travel	73
15.1	<i>Huma</i> body axis for flight dynamics	73
15.2	Trim variables for off-mission analysis with <i>Huma</i> lift-compound configuration.	75
15.3	Trim forces and moments for long endurance mission analysis with <i>Huma</i> lift-compound configuration.	76
15.4	Trim forces and moments for supply delivery mission analysis with <i>Huma</i> SMR configuration.	77
15.5	Trim control inputs for both missions.	78
15.6	Stability roots for <i>Huma</i> SMR configuration.	78
15.7	Stability roots for <i>Huma</i> lift-compound configuration.	79
15.8	Open loop vs Closed loop response for <i>Huma</i> SMR with 8 m/s side gust at hover	80
15.9	Example of an ACAH DI controller for lateral axis	81
15.10	Time simulation for vertical and forward climb/descend mission segments	84
15.12	1-cos gust with varying lengths	84
15.11	Step response at hover and forward flight at 80 kts	85
15.13	Landing with 8 m/s side gust with duration 3 sec	86
15.14	Landing with 8 m/s side gust with different gust lengths	87
15.15	Gust Rejection during the take-off and landing phases with 8 m/s side gust	88
15.16	Landing with different wind limits and directions	89
16.1	Streamlines, pressure, and skin friction along centre line (80 knots)	90
16.2	Streamlines, pressure, skin friction of re-designed fuselage (80 knots)	91
16.3	CFD of landing gear and hub fairing (80 knots)	92
16.4	HOGE power versus altitude at the designed GTOW (160 kg)	93
16.5	Cruise power versus velocity at the designed GTOW (160 kg)	94
16.6	Lift to drag ratio at various airspeeds and vehicle configurations	94
16.7	Payload-range and payload-endurance diagrams	95
18.1	Overall sound pressure level during hover	98
20.1	Examples of additional applications.	99

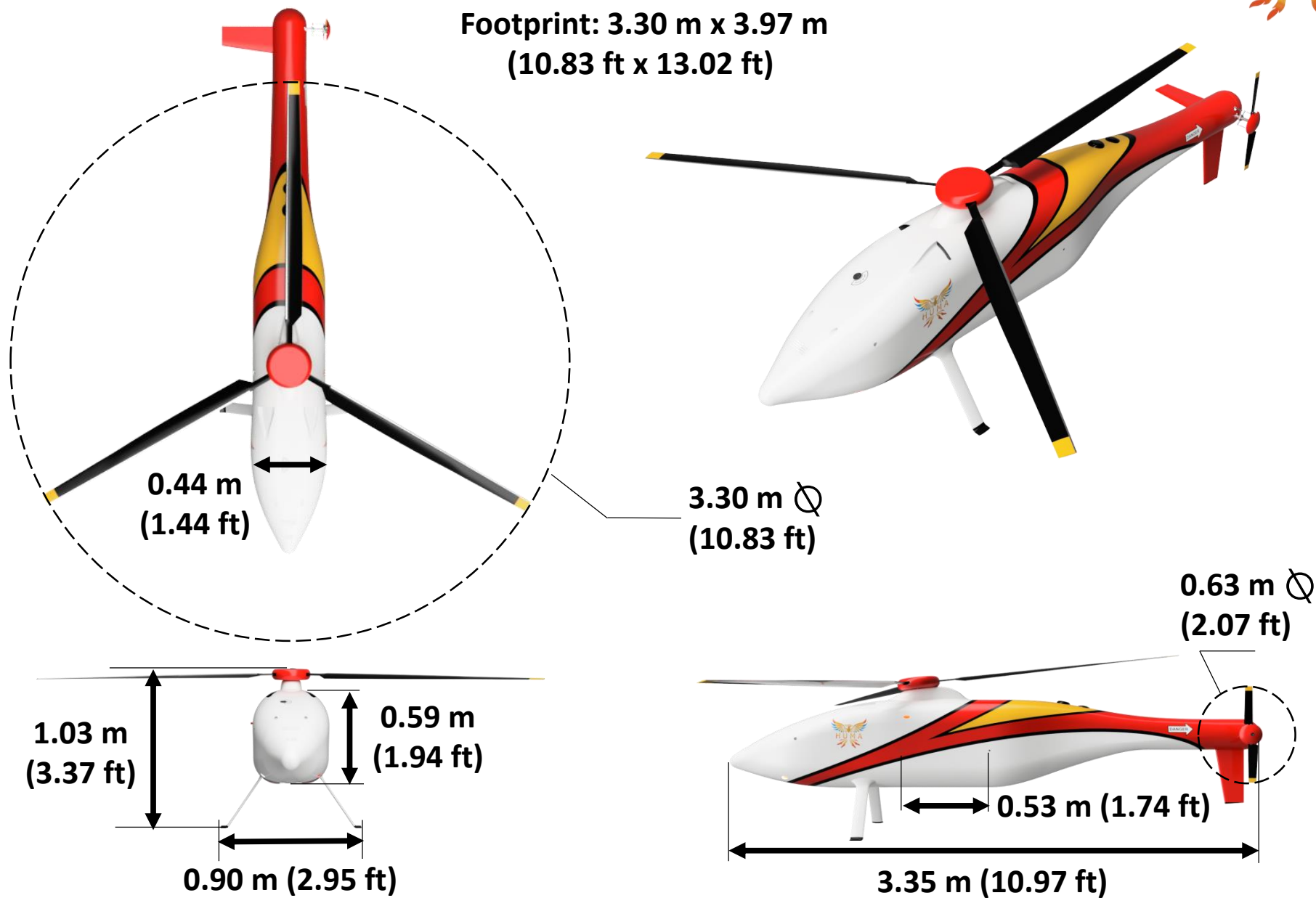
List of Tables

1.1	Overview of <i>Huma</i>	5
2.2	Normalized Priority Vector	6
2.1	Analytical Hierarchy Process (AHP) Matrix	7
2.3	Pugh Matrix for Vehicle Configuration Selection	10
3.1	Component Weight Model Validation	12
3.2	Comparison of vehicle configurations	17
3.3	<i>Huma</i> final selected parameters	18
4.1	Modular components weight summary	19
5.1	Design space for Genetic Algorithm	26
5.2	Optimized main rotor blade	28
5.3	Main rotor performance	28
6.1	Blade frequencies at nominal and lift compound cruise rotor speeds	33
7.1	Hub type selection matrix	35
9.1	Tail rotor diameter trade study	42
9.2	Tail Rotor Parameters	44
10.1	Material selection for structural components	47
10.2	Table summarizing the landing gear trade study	50
11.1	Summary of candidate engine characteristics	52
11.2	Summary of candidate engine characteristics	53
11.3	Summary of candidate generator characteristics	54
12.1	Design parameters for main gearbox bevel gears	59
12.2	Summary of primary belt and pulley data	60
12.3	Design parameters for tail gearbox bevel gears	62
12.4	Summary of primary belt and pulley data	62
13.1	Avionics weight, cost, and power summary	70
13.2	Electrical power components weight and cost summary	71
14.1	Vehicle weight breakdown	71
15.1	Key stability derivatives of <i>Huma</i> in Hover and Cruise	79
16.1	Component-wise drag and flat plate area	92
16.2	Aerodynamic Metrics	93
16.3	Long endurance (lift compound) mission-specific performance data	96
16.4	Supplies delivery (SMR) mission-specific performance data	96

RFP Deliverable	Source	Section/Figure
Trade Studies Configuration choice Rotor design Powerplant selection Transmission design Wing design Fuselage design	RFP 2.4.1	2, 3 2 5, 6 11 12 8 10
Vehicle Performance Total power Aerodynamic power Transmission efficiency Powerplant efficiency Off-mission performance analysis Off-mission trim analysis	RFP 2.4.2	16 16.7 16.7 12 16.7 16.5 15.2
Weight Breakdown Component weight breakdown Weight at each mission segment Center of gravity analysis	RFP 2.4.3	14 14 Fig. 14.1 14
Aerodynamic Metrics L/q , D/q , and M/q at zero degrees vehicle pitch and yaw Component drag breakdown	RFP 2.4.4	16 16.3 16.1
Vehicle Drawings Three-view geometry Fuselage and wing internal layout Modular add-on interfaces	RFP 2.4.5	Page 1-2 Page 46, Fig. 8.1(b) 4
Control Laws Stability and Controllability Ship-board takeoff and landing in high wind and gust Gust rejection	RFP 2.4.6 (grad only)	15.4 15.4 15.4.3 15.4.3

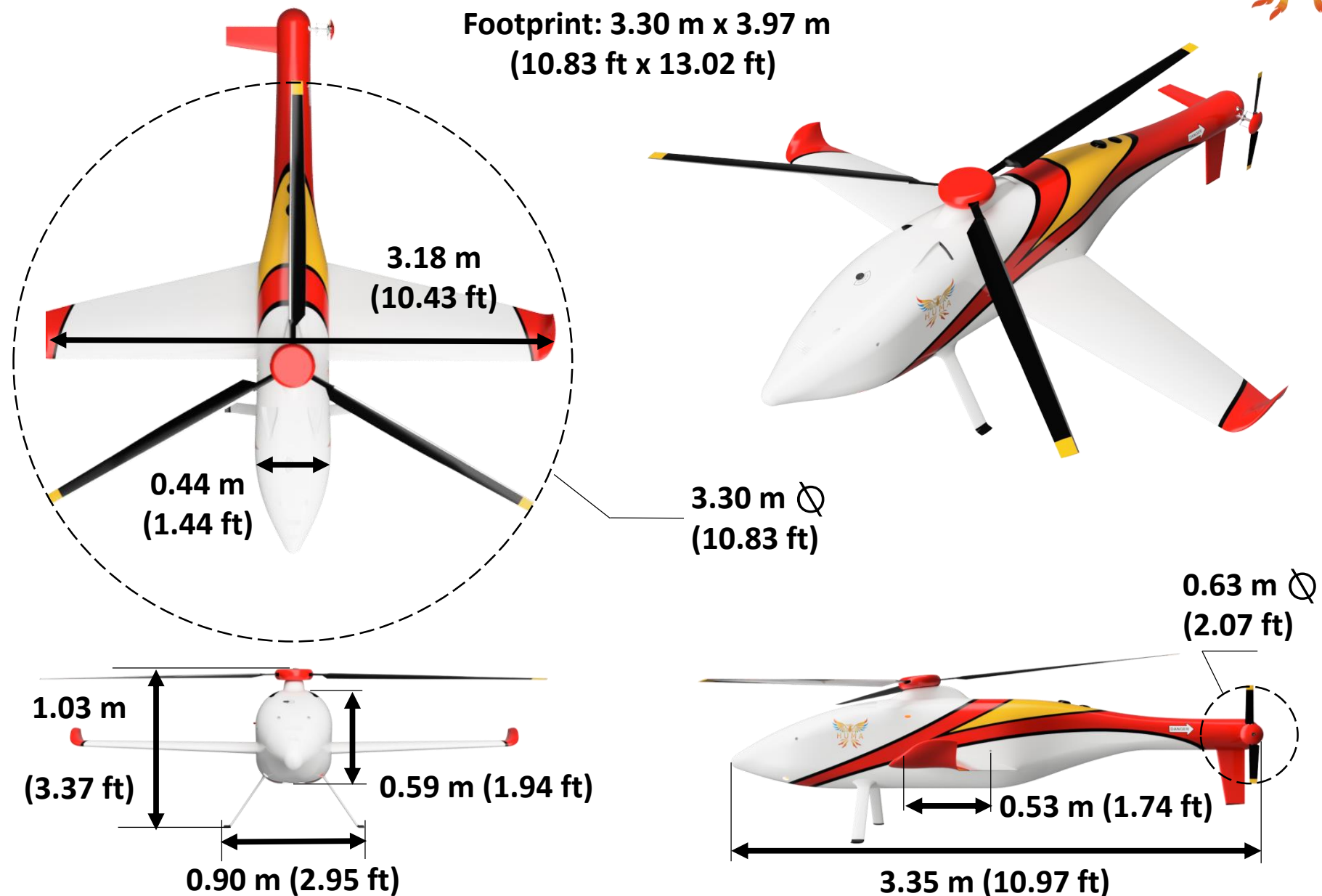


Supplies Delivery Configuration: SMR





Long Endurance Configuration: Lift Compound



1 Introduction

The resilience of a community and national infrastructure is tested in the wake of large-scale disasters. These events create challenging environments for emergency response efforts, recovery strategies, and post-disaster rebuilding. The devastation wrought by disasters such as the earthquakes in Turkey and Syria in Feb 2023, floods in Pakistan in March 2024, and wildfires in Maui in 2023, stands as a stark reminder of the profound disruptions inflicted upon critical communications and transportation networks needed for ground-based emergency response systems.

The 7.8-magnitude earthquakes in Turkey and Syria in February of 2023, with epicenters striking near densely populated regions of Gaziantep, caused the loss of 55,000 lives, rendered roads impassable, and made most communications networks inoperable [1, 2]. 210 million tons of rubble needed clearing before vital aid could be delivered and rebuilding could begin. Similarly in June-Oct 2022, the monsoon rains of unprecedented intensity in Pakistan inundated vast swaths of land and displaced almost 8 million people at the height of the crisis [3]. At least 800 drinking water supply systems were damaged, forcing residents to rely on contaminated water sources for two weeks after the flooding. Similar disasters struck Afghanistan and Pakistan again in March 2024. Some would have benefited from aerial reconnaissance to identify hot spots, while others could have used rapid air delivery from ship to shore.

These disasters illuminate the need for rotorcraft with multi-mission capabilities to perform countless relief tasks including aid package delivery, airborne communications relaying, and disaster imaging. Furthermore, small unmanned rotorcraft are ideal for launching and recovering in confined areas of a disaster zone or a rapid-response ship to swiftly deliver aid. The University of Maryland's Graduate Design Team has developed *Huma* in response to this need prescribed by the 41st VFS Student Design Competition, sponsored by the U.S. Army Research Laboratory. *Huma*, a reconfigurable lift-compounded single main rotor and tail rotor helicopter (SMR), offers unprecedented multi-mission capability in long endurance flight and heavy payload delivery for a VTOL-capable Uncrewed Aerial System (UAS). The mythical bird *Huma*, after which the aircraft is named, originates from Iranian and Turkish folklore near the regions impacted by the earthquakes in 2023. The *Huma*, a bird of fortune, spends its entire life flying high above the earth, spreading blessings and good fortune to those who are touched by its shadow. *Huma*, the UAS, embodies this myth with its long endurance flight and ability to deliver aid to people in desperate need.

The challenging dual-mission requirements of a 10-hour on-station loiter and 50 kg (110 lb) supplies delivery resulted in a uniquely adaptable unmanned helicopter that can transform within 10 minutes from a cruise-optimized Lift-Compounded Rotor configuration with wings (*Huma* LCR) to a Single Main Rotor payload delivery workhorse featuring a large package bay (*Huma* SMR). The design philosophy focused on superior performance for both missions, enabled by a reconfigurable mid-section with special attachments for wings,



Figure 1.1: *Huma* operating as an aerial cell relay during a wildfire.



fuel tank, and payload bay. Digital vehicle design employing modern in-house high-fidelity analysis tools — CFD and CSD — upfront in the design cycle prevented costly design iterations. Recent lift-compounded Mach-scaled rotor wind tunnel tests from the Maryland Compound Rotor Rig guided the design for low vibration and optimal lift share. *Huma* is a 160 kg (353 lb) maximum gross takeoff weight (MGTOW) rotorcraft with a compact 3.3 m (10.8 ft) diameter rotor, enabling five vehicles to fit within a 4 m × 12 m (13 ft × 39 ft) storage bay with the wings attached or seven vehicles with the wings removed. A 3-bladed hingeless hub main rotor eliminates flap and lag hinges which makes *Huma* resilient to gusts up to 15 m/s (29 knots) using high-bandwidth actuators. A pre-shaft tilt and a variable speed rotor prevent the need for an expensive pusher propeller while harnessing wing-compounding to its maximum benefit. Flight control system design focused on reliability and operations in challenging weather conditions using sensor-fusion with dynamic inversion architecture to increase situational awareness for path planning and navigation, obstacle avoidance, and error rejection. The avionics system was specifically designed with redundancy in mind; it uses a combination of eight thermal and visible-spectrum cameras, Inertial Measurement Units (IMUs), and object-tracking radar to create a full three-dimensional topology of the surroundings including moving obstacles. A simple fixed three-point landing gear repurposed the vertical stabilizer to minimize forward flight drag while saving weight by eliminating retraction actuators and linkages. The modular detachable wings and center-body attachments enable a sub-10-minute assembly from a storage state to a winged flight-ready state by two people with merely a dolly and a screwdriver. In general, *Huma* is designed to be a compact rotorcraft while still delivering superior performance for both the long-endurance and supplies delivery missions. An overview of *Huma*'s features is in Table 1.1.

2 Configuration Selection

Huma is designed for high cruise efficiency, low empty weight fraction, rapid gust rejection, and modularity for multiple missions. The design was created using a top-down approach, where the configuration and major components were selected before subcomponents were determined and underwent refinement. Careful attention was paid to the voice of the customer while allowing freedom for creativity. The RFP emphasized modularity: swappable vehicle components to tailor performance to a specific mission profile. A rigorous configuration selection process was conducted to identify four configurations for further detailed analysis in Section 3.

Analysis of the RFP translated the voice of the customer into design drivers which were weighed using the Analytical Hierarchy Process (AHP) [4]. Each driver was scored against another in pairs to determine an ordered normalized priority vector. After ranking the design drivers, a Pugh matrix was developed using the normalized priority vector scaling factors to order the considered vehicle configurations quantitatively [5]. The top four configurations were selected with this method. The final decision, between these four configurations, was made after a detailed sizing analysis for both mission profiles outlined in the RFP.

2.1 Voice of the Customer

2.1.1 Design Drivers

Careful analysis of the RFP determined eight key design drivers. These drivers are listed below in order from highest to lowest importance ranked by the AHP:

1. **Loiter Endurance:** The aircraft must be capable of meeting the 10-hour loiter threshold specified by the RFP. Thus the vehicle should have the lowest minimum power in loiter.
2. **Empty Weight Fraction:** The ratio of the weight, excluding fuel and payload, to the gross takeoff weight. The lower this fraction the more fuel or payload can be carried.



Table 1.1: Overview of *Huma*

Features	Summary
Attachable/removable wings, fuel tank, and center-body payload bay	The 160 kg <i>Huma</i> can tailor its capabilities to the competing requirements of both RFP missions, namely, high L/D wings with the FX 63-137 airfoil for 10+ hr endurance and low empty weight fraction for 50 kg (110 lb) supplies delivery. A center-body bay with bolt-hardpoints implements an interchangeable payload or wings with an auxiliary fuel tank.
Lift compounding during long endurance loiter	A 48% lift sharing to highly efficient wings significantly decreases loiter power and fuel required. Hence, a 13-hr loiter duration exceeding RFP requirements is achieved.
Optimized blade geometry for high FM hover, high L/D lift compound and SMR cruise	The main rotor blade geometry was carefully selected using a genetic algorithm to obtain a 7.5 L/D for long endurance loiter and a 0.81 Figure of Merit. Twist, taper, airfoils, and their transition regions were selected for exceptional performance for both the SMR and lift compound.
Hingeless hub designed for gusty environments	3-bladed hingeless main rotor hub designed for low hub drag and simplicity for ease of manufacturing. Each blade features an integrated flexbeam tailored to balance high control authority and exceptional gust tolerance while being resistant to aeroelastic instability.
Variable rotor speed	Rotor speed reduction by 15% from hover minimizes profile drag and improves L/D during lift compounding in cruise.
Tail rotor designed for high wind and gusts from all directions	The tail rotor was designed for low power consumption while maintaining control authority in high wind. It is free from vortex ring state and stalls from crosswinds up to 8.8 m/s (17 knots), exceeding RFP requirements.
Advanced flight control system	Dynamic inversion control architecture ensures high gust tolerance and stability for all vehicle configurations and flight conditions.
Vision-based ship deck landing algorithm	<i>Huma</i> features an advanced 3D feature-based vision algorithm with inside-out thermal and optical camera tracking to accurately estimate ship deck motion. This enables landing in rough sea states without needing external tracking from the ship.
Robust avionics suite	Multiple sensors fuse data to dynamically maintain full three-dimensional situational awareness. Triple-redundant flight controllers ensure the safe continuation of flight with one failed data stream.
Fixed three-point landing gear	The fixed three-point landing gear repurposes the vertical stabilizer to minimize cruise drag without heavy retractable systems.
Lightweight belt-driven transmission system	Belt driven transmission decreases weight and cost by eliminating gearbox housings, additional gear stages, and complicated oil distribution systems.
Low purchase and operating costs	<i>Huma</i> 's overarching configuration, internal technologies, and material selection are industry-proven. No research and development costs are required. Many components are low-cost commercial off-the-shelf (COTS), including avionics, transmission belts, driveshafts, and bearings.
<5-year entry to service	The SMR configuration is ubiquitous in VTOL operations. The high technology readiness level and safety record of this configuration guarantee maturity and reliability for swift entry to service due to preexisting regulations for certification.



3. **Gust Rejection:** The vehicle must return to equilibrium after a disturbance caused by gusts up to 8 m/s (16 knots). A vehicle with good gust tolerance should be able to accomplish this return to stability as quickly as possible with high spatial accuracy. Configurations that typically express poor gust rejection include features such as large surfaces exposed to the gust.
4. **Shipboard Launch and Recovery Capability:** The vehicle must take off and land on a ship deck. This requirement will encompass agility for launch and recovery. The dynamic characteristics of the ship deck and ship airwake will require high agility to land within the landing footprint. For example, a vehicle with high disk loading could have undesirable effects during a shipboard landing.
5. **Compactness:** Footprints must be limited to the 6×6 m (19×19 ft) helipad constraint and hangar storage constraints. An aircraft with a smaller footprint is easier to store and operate from small helipads.
6. **System Safety and Reliability:** System safety covers the air vehicle operation, ground and ship crew, component redundancy, and emergency termination of flight.
7. **Lifecycle Costs:** Lifecycle cost accounts for the cost of development, production, operation, and maintenance costs. Low cost will ensure large-scale utilization. Less moving parts and simple manufacturing will allow for lower costs.
8. **Technological Maturity:** Vehicles with time-tested maturity are preferred. Maturity is quantified with the NASA/United States Department of Defense (DoD) Technology Readiness Levels (TRLs).

2.1.2 Analytical Hierarchy Process (AHP)

The Analytical Hierarchy Process was used since it allowed the team to consider and narrow down a wide range of vehicle configurations using the voice of the customer. This process ensured that the team effectively analyzed the RFP to determine the characteristics of an ideal configuration for the customer. The AHP matrix produces a weighted priority vector based on the relative importance of design drivers. Each design driver in the left column was assigned a score against another driver in the top row. These scores span from 1/9 to 9 with scores <1.0 indicating the row driver is less important than the column driver and scores >1.0 indicating the opposite. Each team member individually completed an AHP matrix, all of which were subsequently averaged and carefully reviewed to maintain a low standard deviation with the Saaty consistency index, thus reducing the influence of personal biases and interpretations on the voice of the customer. The resulting AHP matrix is shown in Table 2.1. Dividing each table element in a column normalized AHP matrix by its row sum generated the normalized priority vector in Table 2.2. The relative weights of each driver in this vector are used for the configuration selection Pugh Matrix described in the next section.

Table 2.2: Normalized Priority Vector

Design Driver	Weight
Loiter Endurance	29.51%
Empty Weight Fraction	22.31%
Gust Rejection	14.47%
Shipboard Launch & Recovery Capability	11.11%
Compactness	8.99%
System Safety and Reliability	5.61%
Lifecycle Costs	4.46%
Technological Maturity	3.52%
Total	100%

fraction. The fuel savings from efficient cruise may not outweigh additional component weight for the

The ranking indicates that the most important driver for the design is **loiter endurance**. Minimizing loiter power is paramount since the vehicle spends the majority of the long endurance mission in loiter and a significant portion of the supplies delivery mission en route to the destination. Minimizing the amount of energy required increases payload weight fraction. Although cruise efficiency is important, it cannot be at the cost of the second design driver, **empty weight**



Table 2.1: Analytical Hierarchy Process (AHP) Matrix

Design Drivers	Compactness	Empty Weight Fraction	Loiter Endurance	Lifecycle Costs	System Safety and Reliability	Gust Rejection	Technological Maturity	Shipboard Launch and Recovery Capability
Compactness	1	0.29	0.25	3.86	2.24	0.49	3.57	0.95
Empty Weight Fraction	3.58	1	0.72	5.57	4.86	2.57	5.43	3.14
Loiter Endurance	4.43	2	1	6.71	5.43	3.57	6	3.29
Lifecycle Costs	0.28	0.18	0.16	1	0.98	0.66	1.6	0.24
System Safety and Reliability	1.12	0.22	0.2	2.05	1	0.32	2.71	0.49
Gust Rejection	2.86	0.45	0.31	3.48	3.43	1	4.71	3.48
Technological Maturity	0.37	0.2	0.18	1.37	0.5	0.22	1	0.24
Shipboard Launch and Recovery Capability	3.6	0.34	0.35	4.43	3	0.76	4.14	1

shorter supplies delivery mission, thus keeping the empty weight fraction low ensures that the vehicle is effective for both missions. The third most important design driver is **gust rejection**. The rotorcraft is expected to safely and accurately position itself above the ship deck during launch and recovery while experiencing relatively high winds and gusts for the vehicle weight from various directions. The design drivers with lower weights were not omitted from the design process and were important considerations for local analysis of individual components within *Huma* documented later in this proposal.

2.2 Candidate Vehicle Configurations

A study of 12 major configurations was performed using a Pugh decision matrix to select the best one for both mission types. The configurations were ranked with respect to the design drivers. The single main rotor and tail rotor (SMR) helicopter was used as the baseline for comparison owing to its time-tested reliability. A succinct overview of each configuration is provided below, along with their respective advantages and disadvantages. These configurations are separated into two groups based on propulsion and control strategies: 1) Standard propulsion and transmission with swashplate controlled rotors (up to 2 rotors), 2) Distributed propulsion with collective or RPM controls (3 or more rotors).

2.2.1 Standard Rotorcraft (up to 2 main rotors)

The configurations in this category are the following:

- **Single Main Rotor and Tail Rotor (SMR):** The single main rotor and tail rotor uses a single large diameter rotor for lift and propulsion in addition to a conventional open tail rotor to counter the torque of the main rotor. It is the most widely used rotorcraft configuration. This configuration is used as the baseline for comparisons.





Figure 2.1: Standard Rotorcraft Configurations Considered

- **Coaxial:** The coaxial features two vertically separated counter-rotating rotors that naturally cancel the torque without the need for a tail rotor. This configuration is more compact than the SMR but more complex, expensive, heavier, and more challenging yaw control. Furthermore, a taller mast structure to prevent blade strike would cause greater hub drag in forward flight. While suitable for shipboard operations, the coaxial is not well-suited for a 10-hour loiter.
- **Lift Compounded SMR (with wings):** The lift compounded SMR features a fixed wing. This configuration has a greater lift-to-drag ratio (L/D) due to lift sharing by the wing and tip speed reduction [6]. Lift sharing also reduces vibrations in cruise flight. Some weight penalty is incurred and additional thrust of up to 6% may be required due to download [7]. The wings decrease gust tolerance; however, this can be mitigated by moderate lift sharing based on test data from in-house Mach-scaled hover tests.
- **Lift plus Thrust Compounded SMR (with wings and a pusher propeller):** The lift plus thrust compounded SMR adds a pusher propeller. Cruise efficiency is increased further as the propeller relieves the main rotor of propulsive thrust. The empty weight also increases further as an additional transmission is required in the rear. The thrust compound benefit is mainly realized in very high-speed flight which is not required by the prescribed missions [8].
- **Tandem:** The tandem configuration includes two longitudinally offset counter-rotating rotors that naturally produce zero net torque on the aircraft. Gust tolerance is improved by the lack of a tail rotor. The rotor separation increases longitudinal center of gravity (CG) travel tolerance for heavy package delivery. This configuration has a high empty weight due to the second rotor and hub, interconnecting shafts, and support structure. Additionally, rotor overlap is required due to landing area and storage space constraints. The overlapping rotors decrease cruise performance due to high parasitic drag and cause increased vibrations from the rotor-rotor wake interactions.
- **Coaxial Tailsitter with Wings:** This configuration merges the coaxial rotorcraft with a fixed-wing aircraft. It lands on its tail after transitioning 90° from the cruise attitude. Wing-borne cruise flight significantly improves high-speed cruise efficiency but the wing was found to be close to stall in a lower-speed loiter. Counter-rotating rotors eliminate the need for a tail rotor. That also reduces footprint but complicates the hover-to-cruise transition due to poor pitching moment authority. The coaxial system also has weak yaw authority. Additionally, the large vertical wing surfaces diminish gust and steady wind tolerance in hover.

- **Tiltrotor:** The tiltrotor configuration features a fixed wing and wingtip mounted tilting propellers. This decreases empty weight but increases hover download. High cruise L/D is achieved, however, only at very high speeds not required for this RFP.
- **Tiltwing:** The tiltwing configuration features a rotating wing and wing-mounted rotors. Tilting mechanisms and interconnecting drive shafts drastically increase empty weight. It is difficult to meet the operational space limitations and max takeoff weight restrictions together due to the small diameter wing-mounted rotors. Moreover, the rotating wing decreases download in hover but decreases gust tolerance due to a large wing area for wind impingement. This configuration may be viable in high-speed cruise with long hover, neither of which is required for this RFP.

2.2.2 Multirotors (3 or more rotors)

Multirotors (≥ 3 Rotors) distribute power to many rotors. Multirotor swashplate systems are simple as cyclic control is not needed. However, a significant weight penalty is incurred if power distribution is done purely mechanically due to the large number of transmission shafts and gearboxes required. These configurations can also be powered with heavy engine-generator hybrid systems and battery-driven distributed electric propulsion systems. These additional powerplant weights were ultimately deemed to be too heavy for the design weight class, which is discussed in Section 11.1.

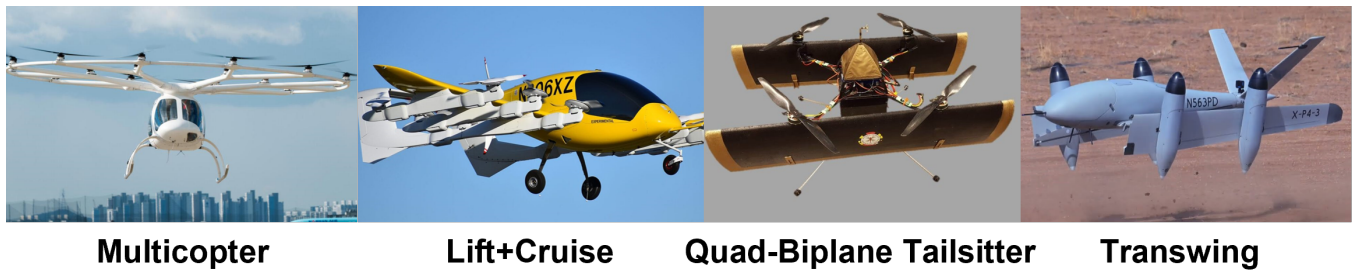


Figure 2.2: Multirotor Configurations Considered

- **Multicopter:** The multicopter configuration distributes thrust to several rotors that provide lift and propulsive thrust. This configuration has favorable hover agility and gust tolerance capability from the multirotor control scheme but suffers from high empty weight, high cost, and poor cruise performance.
- **Multicopter Lift + Cruise (with wings and a pusher propeller):** The lift+cruise configuration alleviates the multicopter's cruise performance issues with a wing and pusher propeller. However, additional components significantly increase the empty weight fraction, which is greatly undesirable for the supplies-delivery mission.
- **Quadcopter Biplane Tailsitter:** The quadrotor biplane tailsitter rotates in orientation between cruise flight and hover/landing. The wing-mounted motors can generate large rolling and pitching moments, thus hover agility and hover-cruise transition ability are improved in comparison to the coaxial tailsitter. However, additional framing and support braces increase the empty weight fraction and decrease cruise efficiency.
- **Transwing:** The transwing configuration transforms between a monoplane in cruise to a quadcopter in hover. The wing-borne flight yields high L/D and the folded configuration allows for impressive hover agility. However, the complicated multi-axis wing folding mechanism significantly increases empty weight. The limited adoption of this conversion mechanism in existing flight vehicles causes this configuration's Technology Readiness Level (TRL) to be low.

All of these configurations are currently viable for small duration and short-range electric flight, not for

long endurance flight where an internal combustion engine or gas turbine engine is essential.

2.3 Pugh Matrix

The team ranked the wide range of considered vehicle configurations using a Pugh decision matrix (Table 2.3) to select the best vehicle configuration. The single main rotor and tail rotor (SMR) configuration was used as the baseline so all its values were set to zero. A grading scale of -5 (very poor) to +5 (very good) with increments of 1 was used to rate each configuration relative to every design driver. The final score was determined by weighting the Pugh matrix result with the normalized priority vector from the AHP to properly account for the voice of the customer.

Table 2.3: Pugh Matrix for Vehicle Configuration Selection

Design Drivers	Weights	SMR	Coaxial	Lift Compound SMR	Lift+Thrust Compound SMR	Tandem	Coaxial Winged Tailsitter	Tilting	Tiltrotor	Multicopter	Lift+Cruise	Quadrotor Biplane Tailsitter	Transwing
Compactness	0.09	0	2	0	-1	0	-2	-3	-3	3	-2	2	2
Empty Weight Fraction	0.22	0	-2	-1	-2	-3	-3	-5	-4	-2	-4	-3	-5
Loiter Endurance	0.3	0	-2	2	3	-1	4	3	3	-5	2	1	3
Lifecycle Costs	0.04	0	-2	0	-1	-2	-3	-4	-3	-1	0	-2	-4
System Safety and Reliability	0.06	0	-1	0	0	-1	-1	-2	-1	2	2	2	-2
Gust Rejection	0.14	0	1	-1	-2	2	-2	-2	-1	3	2	0	1
Technological Maturity	0.04	0	0	-1	-1	0	-2	-4	-1	-2	-2	-4	-5
Shipboard Launch and Recovery Capability	0.11	0	1	-1	-1	0	1	-2	-2	3	-1	1	1
Score	1	0	-0.75	0.09	-0.1	-0.82	-0.07	-1.41	-0.83	-0.92	-0.25	-0.19	-0.25

The Pugh matrix results indicate that the lift compound, SMR, coaxial winged tailsitter, and lift plus thrust compound strongly fit the requirements outlined by the customer. These four were downselected for detailed analysis. The coaxial winged tailsitter and compound configurations better suited the long endurance mission whereas the SMR configuration better suited the short supplies delivery mission. The Pugh matrix included the criteria from both missions so detailed analysis is required to select the best. This is described in Section 3.

3 Preliminary Vehicle Sizing

Huma is intended to have a low empty weight fraction, be gust tolerant, and be highly cruise efficient. A thorough sizing analysis was conducted to select the final configuration from the four downselected options.

3.1 Mission Profiles

The two missions are shown in Figure 3.1. There are five segments in each mission.

1. Ground idle, takeoff and climb



- a) 5 minute ground idle at 0 m.
 - b) Vertical takeoff and climb to 10 m (33 ft) mean sea level altitude (MSL).
 - c) Cruise-climb to 500 m (1640 ft) MSL in ≤ 4 min with range credit.
2. Cruise for the 185 km (100 nm) in ≤ 1.25 hrs to the target location/destination
3. Once arrived, there are two options
- **Long endurance:** Loiter for ≥ 10 hours carrying a 20 kg (44 lb) payload.
 - **Supplies delivery:** Deliver a higher payload of 50 kg (110 lb)
 - a) Loiter for 20 mins.
 - b) Cruise-descent to 10 m (33 ft) MSL in ≤ 4 min with range credit.
 - c) Vertical landing on helipad (0 m), offload all payload (50 kg, 110.2 lbs).
 - d) Vertical takeoff from helipad to 10 m (33 ft) MSL.
 - e) Cruise-climb to 500 m (1640 ft) MSL in ≤ 4 min with range credit.
4. Return 185 km (100 nm) over any time
5. Descent and land
- a) Cruise-descent to 10 m (33 ft) MSL in ≤ 4 min with range credit.
 - b) Vertical landing onto ship deck (0 m).

The two missions were simulated for all four vehicle configurations to find the best that serves both missions. Note that the RFP gives only the minimum loiter time for the long endurance and minimum payload for the supplies delivery. They were maximized to provide the customer with the best vehicle.

3.2 Sizing Methodology

The configurations were modeled using an in-house sizing code. It uses blade element theory with airfoil decks and propulsive trim solutions for performance analysis. Input parameters specified are gross takeoff weight (GTOW), loiter altitude, powerplant specific fuel consumption (SFC), flap frequency, and aerodynamic drag factors. Trade studies were performed by varying rotor and wing geometries to select the best values for each configuration before comparing them. The key parameters were disk loading, rotor and wing aspect ratio, rotor tip speed, and wing loading. Figure 3.2 illustrates the sizing flowchart. The iterative procedure began by initializing the mission-specific payload specified by the RFP: 50 kg (110 lb) for the supplies delivery mission and 20 kg (44 lb) for the long endurance mission. Calculations were performed for each mission segment separately. The power required for each dictated fuel weight. Cruise speed was selected as the velocity for best range (V_{BR}) for the cruise segment if it was more than the minimum speed specified by the RFP or velocity for best endurance (V_{BE}) for the loiter segment. Fuselage drag calculations used the Harris equation (Equation 1) with the factor, κ , typically 2.5 for modern helicopters and 1.5 for proprotor-driven fixed-wing aircraft and tiltrotors. This factor was taken as 1.2 for the tailsitter and 2.5 for the SMR and compounds.

$$F \text{ in ft}^2 = \kappa \left(\frac{W_{\text{in lb}}}{1000} \right)^{\frac{2}{3}} \quad (1)$$

Hover and vertical climb/descent download were considered as 3%, 6%, 12%, and 15% of the GTOW for the tailsitter, SMR, lift compound, and lift plus thrust compound respectively. Transmission efficiency and engine installation losses were also included as constant 2% and 5% respectively.



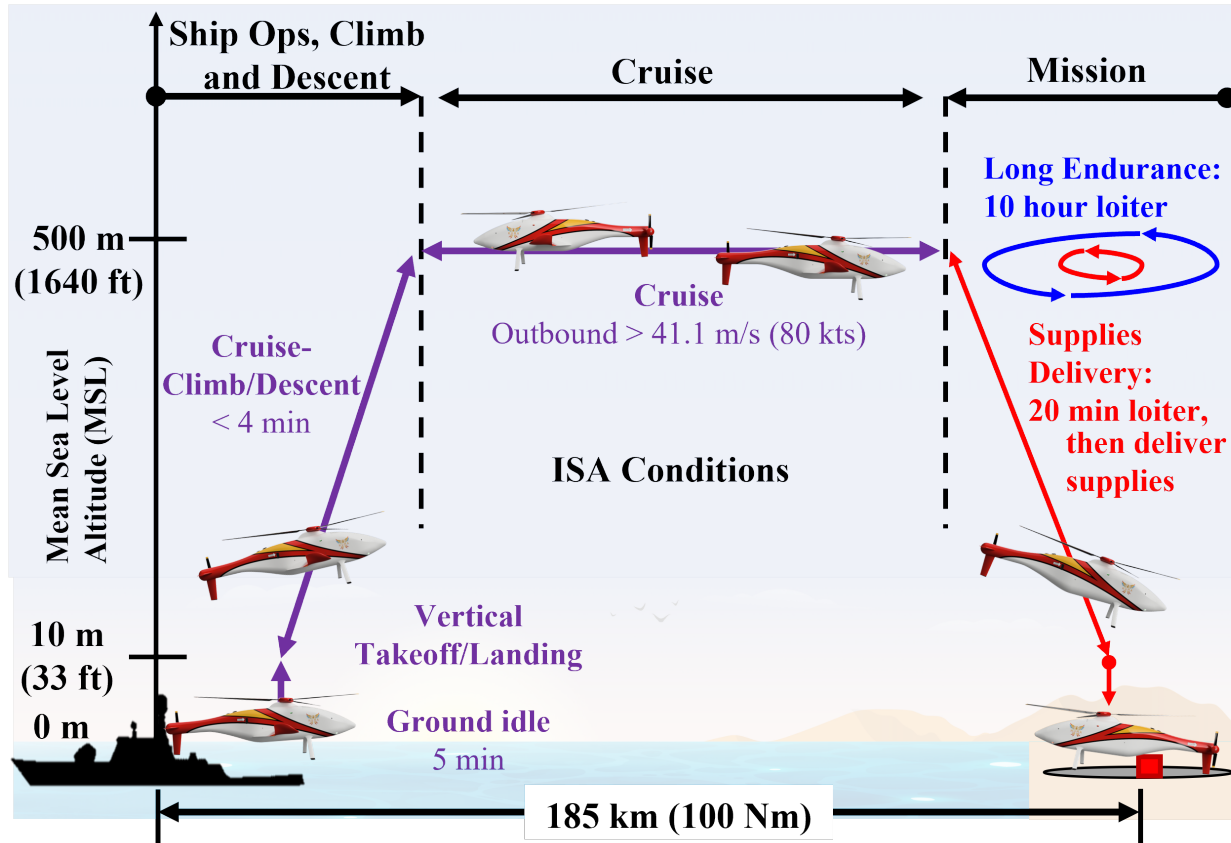


Figure 3.1: Mission Profiles

Weights were calculated using Tischenko models as well as U.S. Army Aeroflightdynamics Directorate (AFDD00) models [9]. Technology factors were used from NASA Design and Analysis of Rotorcraft (NDARC) for rotorcraft components [9] and Raymer for the wing [10]. One departure from these models was the UAV-scale engines which have lower power-to-weight ratios (details in Section 11).

Since the RFP specified the gross takeoff weight (GTOW) as 160 kg (353 lb), the payload was iterated on. Payload greater than the required values was credited to additional fuel for the loiter mission but retained as payload for the supplies delivery mission.

3.3 Weight Model Validation

The Tischenko and AFDD weight models are based on helicopters much larger than the vehicle requested by the RFP. Hence, the model was validated on the Robinson R-22, a SMR helicopter near the UAV weight class. The weight models had good agreement with the major R-22 components as shown in Table 3.1. Thus the models and technology factors were validated.

Table 3.1: Component Weight Model Validation

R-22 Component	Estimated Weight, kg (lb)	Actual Weight, kg (lb)	Percent Error
Main Rotor	37 (82)	36 (79)	3%
Fuselage	68 (149)	60 (133)	12%
Landing Gear	18 (40)	16 (35)	13%
Empty Weight	347 (766)	359.6 (794)	-4%

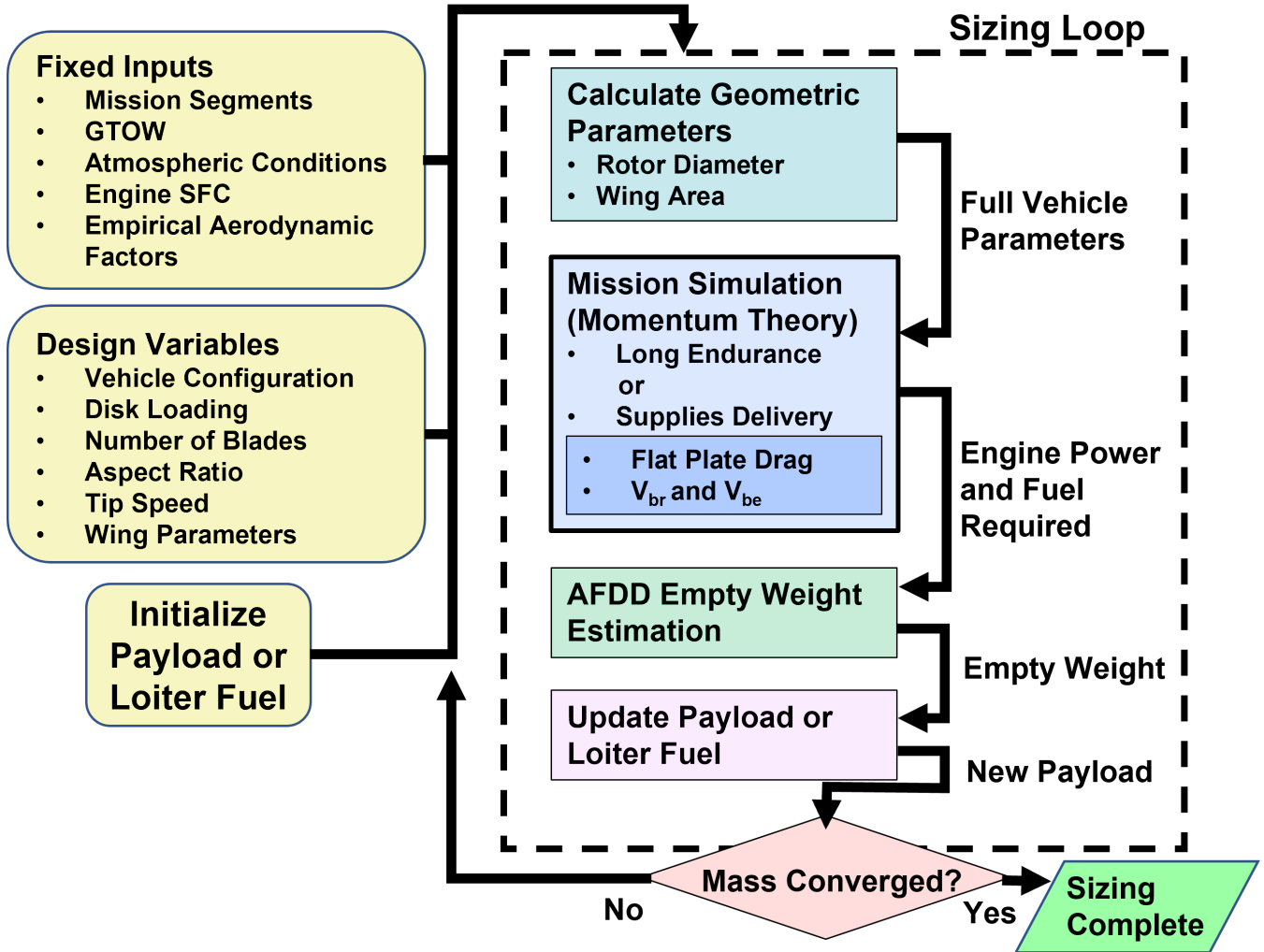


Figure 3.2: Flowchart of Vehicle Sizing Procedure

3.4 Trade Studies

Trade studies were conducted for all configurations; only the lift compound configuration study for the long endurance mission is described for brevity. The input parameters define the rotor and wing geometries and therefore affect available payload weight, power required, and vehicle size. The results of the complete analysis are tabulated in Section 3.4.5.

3.4.1 Number of Blades

The number of rotor blades (N_b) was varied from 2 to 5 while keeping solidity, tip speed, and wing parameters constant. Figures 3.3(a) and 3.3(b) show the effect on maximum payload weight for solidities $\sigma = 0.048$ and 0.075 respectively and for $V_{tip} = 182.8$ m/s (600 ft/s). Note that rotor radius and power do not change with N_b for a given solidity. Increasing N_b increases payload by reducing rotor mass as a decrease in chord more than offsets the increase in blades. However, when $\sigma = 0.048$, rotors with 4 or 5 blades have aspect ratios that are structurally too slender. When solidity is increased to $\sigma = 0.075$, the benefits from increasing N_b diminish due to increased blade weight and engine power. $N_b = 3$ appears to be optimal, as increasing it further yields diminishing returns. Fewer blades also decreases vehicle manufacturing and purchasing costs. Hence, the 3-bladed rotor was selected.



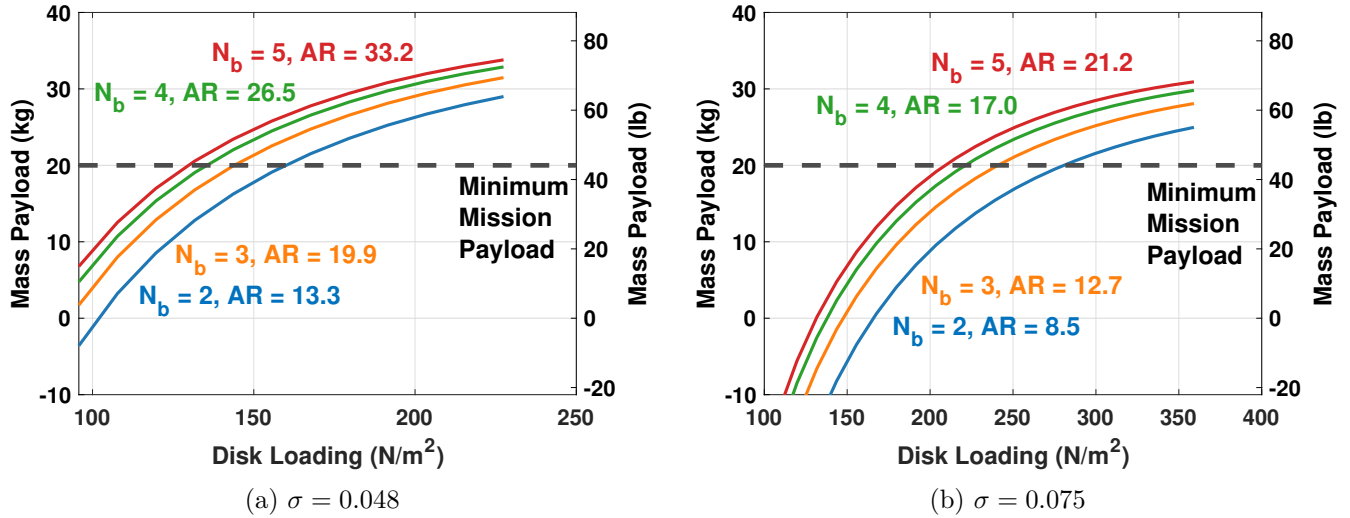


Figure 3.3: Trade study for number of blades

3.4.2 Aspect Ratio and Solidity

With the number of blades selected, trade studies were performed to fine-tune the blade aspect ratio (AR). Aspect ratio variation with a selected blade number changes the rotor solidity. Analysis was performed at $V_{tip} = 182.8$ m/s (600 ft/s). The aspect ratio trade study is shown in Figure 3.4. Higher AR is better for performance due to lower profile drag and tip losses but is limited by blade slenderness and flexibility.

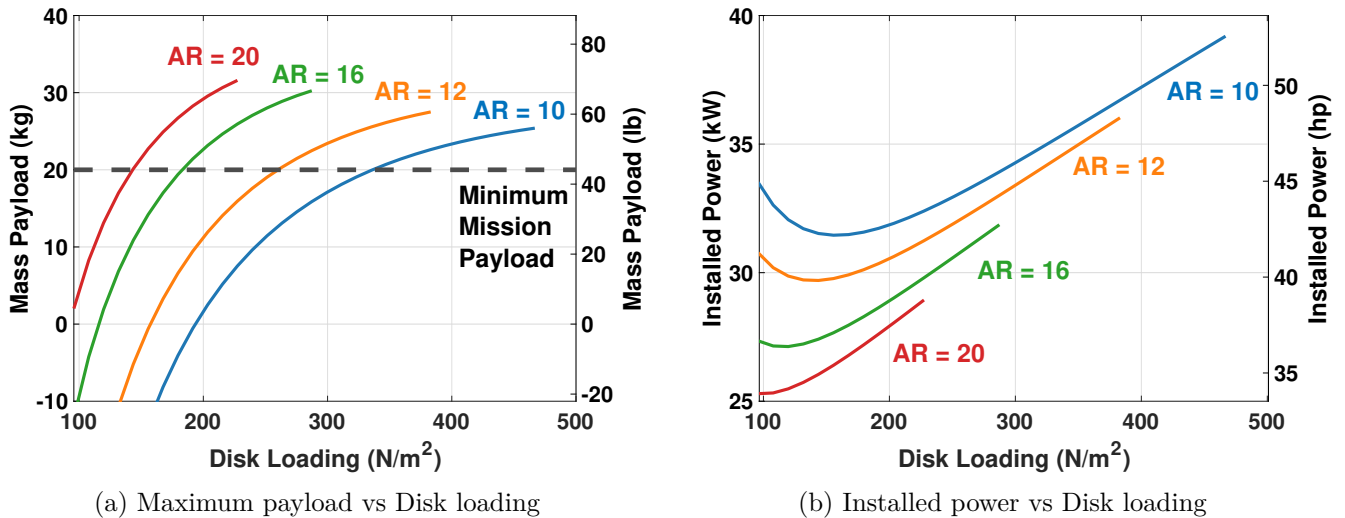


Figure 3.4: Trade study for blade aspect ratio and solidity

Blade loading C_T/σ limits very low solidity. The McHugh stall boundary [11] indicated a hover limit of $C_T/\sigma = 0.16$. It was limited to 0.12 here to keep some margin for maneuvers and gusts.

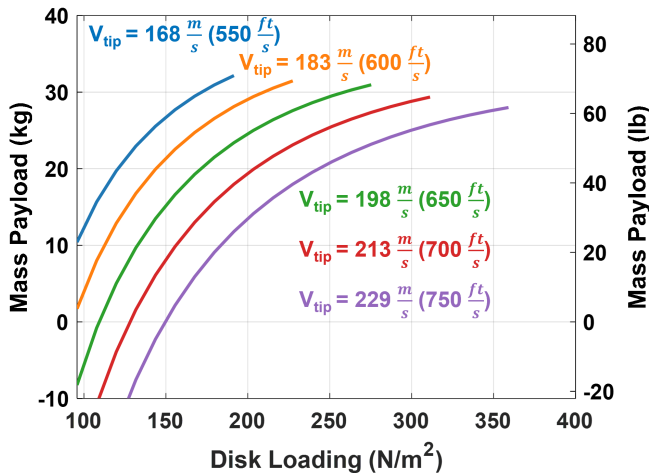
The rotor with the highest aspect ratio yielded the highest performance with the low power required. The lower solidity rotor decreases profile drag, hence a significant decrease in power and fuel burn is observed as increased payload. The highest structurally feasible aspect ratio, 20, was selected for best performance.

3.4.3 Tip Speed and Disk Loading

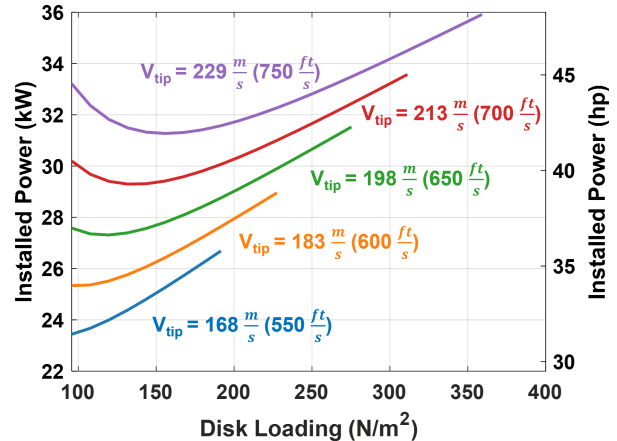
With the number of blades and solidity selected, the tip speed and disk loading were fine-tuned to minimize power and ensure that the helicopter fit within the hangar storage area prescribed in the RFP.

High rotor tip speed decreases hover blade loading and reduces reverse flow region in forward flight. However, it produces high profile drag due to compressibility effects on the advancing side.

The effect of tip speed is shown in Figure 3.5. Figure 3.6 shows rotor diameter versus disk loading. A disk loading of 203 N/m^2 (4.25 lb/ft^2) was the minimum that would accommodate the vehicle within the 4 m (13.1 ft) short hangar dimension. This allowed four aircraft to fit within the hangar without needing tail-boom or blade folding mechanisms. With this disk loading, the maximum payload was achieved with a tip speed of 600 ft/s. Any lower tip speed raised blade loading above 0.12.



(a) Maximum payload vs Disk loading.



(b) Installed power vs Disk loading.

Figure 3.5: Trade study for main rotor tip speed.

The best performance is obtained below maximum blade loading at $C_T/\sigma = 0.103$, which corresponds to the lowest feasible tip speed and disk loading, 183 m/s (600 ft/s) and 203 N/m^2 (4.25 lb/ft^2). This leads to the near-maximum payload without a significant increase in power from drag at a high angle of attack.

In forward flight, the wing sharing decreases rotor thrust. To minimize profile power, the rotor tip speed is reduced to 85% nominal RPM (NR) in cruise, to again near hover blade loading. An increase in rotor efficiency was observed for higher reduction, consistent with UH-60 experiments [12]. A 72% NR would return the blade loading to hover (48% lift sharing by the wing) but this ideal condition was impractical due to efficiency loss of the turboshaft engine. Also, the 85% NR turned out to be beneficial as the loiter advance ratio was pushed up to 0.19, outside of the free-wake dominated high vibration regime.

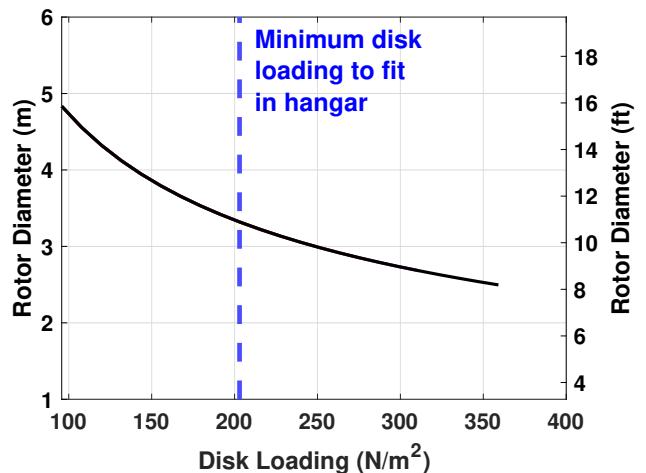


Figure 3.6: Rotor diameter vs disk loading.

3.4.4 Wing Parameters

The wing parameters were determined next. A fixed-wing aircraft typically features L/D values near 12-15 [10] whereas SMR L/D only reaches 4.5 [13]. Lift compounding aims to bridge this gap by offloading the rotor to the more efficient wing. However, the wing share could not exceed 48% without a pusher propeller to maintain a sensible longitudinal shaft tilt angle (α_s). Note that the propulsive thrust is still provided by the main rotor. The forward shaft tilt limit was set at 10° to minimize rotor and fuselage flat plate drag and decrease undesired large blade flapping angles. The outbound 41 m/s (80 knots) fast-cruise segment encountered the highest rotor shaft tilt and set the maximum lift share. Thus, the maximum L/D in loiter was for 6.5° tilt with the rotor fixed at 6.5° relative to the fuselage so that the body pitch angle was zero.

The wing geometry trade study is shown in Figure 3.7. The wing loading was set as 479 N/m^2 (10 lb/ft^2) to achieve a suitable balance of wing area between minimizing hover download and maximizing cruise efficiency. At this wing loading, aspect ratios between 6-10 yielded the same payload mass. Hence, an aspect ratio of 6 was selected to minimize wing structural weight and decrease wing span to aid hangar storage. Additionally, small winglets were added to increase effective AR with a shorter span.

3.4.5 Trade Summary

The SMR, lift compound, lift plus thrust compound, and coaxial winged tailsitter are compared in Table 3.2.

All configurations met the long-endurance mission requirements. The maximum loiter time increased with wing share percentage as cruise L/D increased. Figure 3.8 shows that the lift and thrust compound and tailsitter configurations have the lowest power required at V_{BE} . The tailsitter is operating near stall at V_{BE} , which means minimal margin in gusts. Hence, this configuration was discarded.

The supplies delivery mission payload capacity naturally decreased with increasing empty weight fraction. The larger wings coupled with a propeller for the lift plus thrust compound are heavier than the fuel saved during the short supplies delivery mission. Hence, the lift plus thrust compound configuration was ruled out even though its long endurance mission performance was exceptional.

The final vehicle decision relied upon configuration modularity. The long endurance and supplies delivery missions had competing objectives, therefore selecting a configuration that could have both high lift offloading and low empty weight fraction was paramount. The SMR configuration has the lowest empty weight fraction and is an excellent candidate for multi-mission modularity. Lift compounding can be achieved

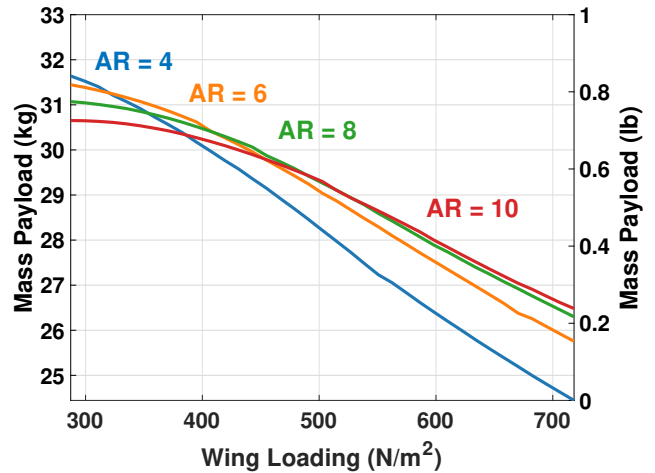


Figure 3.7: Wing parameters trade study.

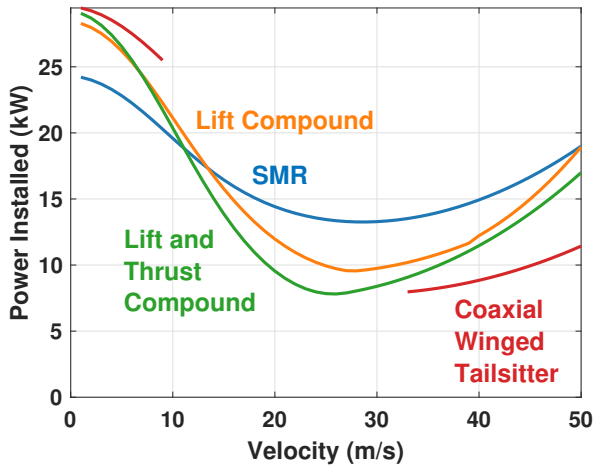


Figure 3.8: Power versus velocity

Table 3.2: Comparison of vehicle configurations

Parameters	SMR	Lift Compound	Lift+Thrust Compound	Coaxial Winged Tailsitter
Disk Loading [N/m ² , (lb/ft ²)]	192 (4)	204 (4.25)	206 (4.3)	252 (5.25)
Number of Blades	3	3	3	3 per rotor
Blade Aspect Ratio	19.9	19.9	19.9	19.9
Rotor Solidity	0.048	0.048	0.048	0.048 per rotor
Rotor Tip Speed [m/s, (ft/s)]	182.9 (600)	182.9 (600)	182.9 (600)	198.1 (650)
Hover M_{tip}	0.53	0.53	0.53	0.58
Rotor Radius [m, (ft)]	1.65 (5.41)	1.65 (5.41)	1.67 (5.48)	1.01 (3.31)
Wing Aspect Ratio	-	6	6	8
Wing Loading [N/m ² , (lb/ft ²)]	-	478.8 (10)	478.8 (10)	718.2 (15)
Wing Share in Loiter	-	48%	80%	100%
Harris Factor	2.5	2.5	2.5	1.2
Hover Download, %GTOW	6%	12%	15%	3%
Empty Weight Fraction	0.57	0.60	0.63	0.64
Long Endurance Loiter Time [hours]	11.6	13.4	13.8	14.0
Supplies Delivery Payload [kg, (lb)]	56.9 (125.4)	53.6 (118.2)	50.1 (110.4)	51.2 (112.8)
Max. Power Required (Seg. 2) [kW, (hp)]	25 (33)	27 (36)	28 (37)	28 (37)

by adding components to the standard SMR. Lift compounding enhances the SMR's loiter time by 15.5% with wings that can be easily attached to the sides of the vehicle by two people in 10 minutes. Therefore, a modular SMR with optional lift compounding was selected as it offered a low empty weight fraction for superior supplies delivery mission payload capacity, exceptional performance for the long endurance mission, and simple modular interfaces for wing attachment and removal by two people within 10 minutes.

3.5 Huma Specifications

Huma is a three-bladed single main rotor helicopter (SMR) that can be reconfigured with wings to become lift compounded. The final configuration specifications are summarized in Table 3.3. *Huma* can loiter for 13 hours and deliver a 58 kg payload, exceeding RFP performance requirements by 30% and 16% for the two missions respectively.

4 Concept of Operations and Multi-Mission Capability

Huma must be capable of completing two missions with significantly differing requirements. The long-endurance mission requires a long loiter endurance, while the supplies mission requires a high payload. The vehicle has been designed around a reconfigurable center body bay that allows a ground crew to attach and detach specialized components that overhaul the aircraft's endurance or payload capacity without the need for specialized tools or a complicated assembly procedure.

4.1 Modular Add-On Components

Huma is allowed a total of 24 kg (52.9 lbs) of add-on weight that can be added to a baseline vehicle before it undertakes either of its two missions. For *Huma*, these modular components must completely change the aircraft from an SMR for the supplies delivery mission, to a lift compounded SMR for the long endurance



Table 3.3: *Huma* final selected parameters

Parameter	Value
Rotor Radius	1.65 m (5.41 ft)
Disk Loading	204 N/m ² (4.25 lb/ft ²)
Number of Blades	3
Aspect Ratio	20
Solidity	0.048
Hover Blade Loading	0.1034
Hover Tip Speed	183 m/s (600 ft/s)
Lift Compound Cruise Tip Speed	155 m/s (510 ft/s)
Wing Area	1.25 m ² (13.45 ft ²)
Wing Aspect Ratio	6
Figure of Merit, Lift Compound	0.80
Figure of Merit, SMR	0.81
Lift Compound Loiter L/D	7.5
SMR Cruise L/D	6.0
Design GTOW	160 kg (353 lb)
Empty Weight (Long Endurance)	95.8 kg (211.2 lb)
Long Endurance Loiter Time	13 hours
Fuel Weight (Long Endurance)	44.2 kg (97.4 lb)
Loiter Velocity (Long Endurance)	28 m/s (55 knots)
Empty Weight (Supplies Delivery)	91.5 kg (201.1 lb)
Supplies Delivery Payload	58 kg (127.9 lb)
Fuel Weight (Supplies Delivery)	10.5 kg (23.2 lb)
Power Required (SL, ISA)	25.7 kW (34.5 hp)
Power Installed	36.8 kW (50 hp)

mission. In addition to the airframe, the interior of the vehicle must subsequently change to carry the appropriate amount of payload and fuel needed to complete the selected mission. In the SMR configuration, the primary modular component is a payload carrying case. Detachable panels for the enclosure skin must also be installed to cover the holes intended for the I-beam spar of the other configuration's wings. In the lift compounded SMR configuration, the modular components include a detachable fuel tank and quick disconnect fuel lines [14], two lightweight composite wings, and an aluminum mounting structure, referred to henceforth as the wing adapter, into which the wings are secured to the airframe. The customer specifies that all add-ons must be swapped out by two crew members with minimal equipment. All modular add-ons can be attached and removed from the base vehicle with one screwdriver and a dolly. The screwdriver is used to loosen and tighten the quarter-turn fasteners that retain the enclosure skin, and affix modular components to their mounting hardpoints. A castering dolly that can be raised or lowered can greatly assist with the maneuvering of the vehicle on a ship deck. It can also be used to hold larger components like the fuel tank and payload case in place during installation, ensuring a rapid installation procedure that requires negligible effort from a trained crew. All the add-ons for both missions are described with their component weights in Table 4.1.

4.1.1 Center Body Bay

The center body bay is located directly beneath the engine firewall, and aft of the forward payload bay. The reinforced structural members of the ceiling were designed to withstand the flight loads and maneuvering



Table 4.1: Modular components weight summary.

Mission	Component	Weight (kg)	Weight (lb)	GTOW Fraction (%)
Long-Endurance	Wings	3.88	8.55	2.43
	Wing Adapter	0.76	1.68	0.48
	Fuel Tank	4.11	9.06	2.57
	Total	8.75	19.29	5.47
Supplies Delivery	Supplies Case	4.40	9.7	2.75
	Enclosure Skin Panels	0.05	0.11	0.03
	Total	4.45	9.81	2.78

loads and serve as mounting hard points for the modular add-ons: wing adapter, long duration fuel tank, and supplies delivery payload case. The bolt pattern is arranged within the thicker structural members of the fuselage, and all of the add-ons mount to the same pattern. Components are affixed to the hardpoints with stainless steel M6 bolts and rubber washers to minimize the vibrations transferred from the fuselage to the wings or payload. This bolt pattern is displayed in Figure 4.1(a).

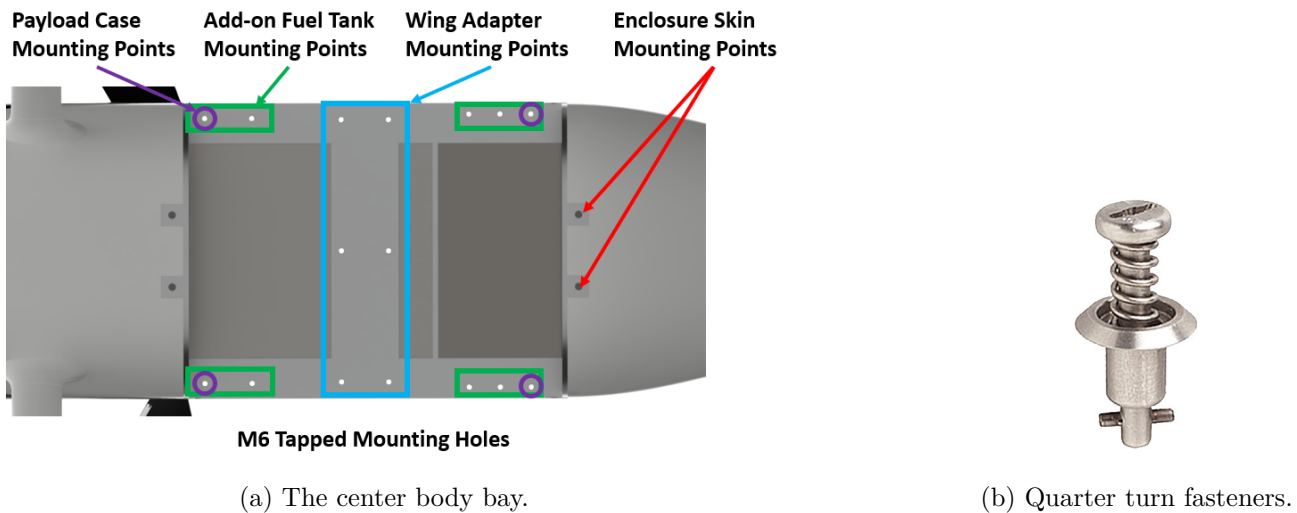


Figure 4.1: Center body bay for mounting modular add-ons.

The center body bay enclosure skin is attached to the fuselage by eight quarter-turn fasteners located on the sides and bottom of the vehicle. These fasteners are commonly used for panel or cowling attachment on general aviation aircraft and can be locked or unlocked rapidly when turned 90° by a screwdriver. These Camloc fasteners are made of corrosion-resistant steel and are spring-loaded, exhibiting exceptional vibration resistance and anti-corrosion properties. The enclosure skin is constructed with two cut-out sections to allow the wing spar to pass through the fuselage. When undertaking the supplies delivery mission, two panels of kevlar are affixed by M6 screw to the structural longerons of the enclosure skin, sealing the holes for the wing.

During the supplies delivery mission, ground crew will need to remove the enclosure skin to access the payload stored in the center body bay. Since *Huma* is meant to serve areas ravaged by disaster all across the world, it cannot be expected that every ground crew will be trained, understand a common language, or have a screwdriver to open the center body bay. Therefore, *Huma* will carry laminated pictographic instructions in the front mission payload bay, which is simply accessible by a latching handle on the door. The instructions guide the ground crew on how to remove and replace the enclosure skin for access to the

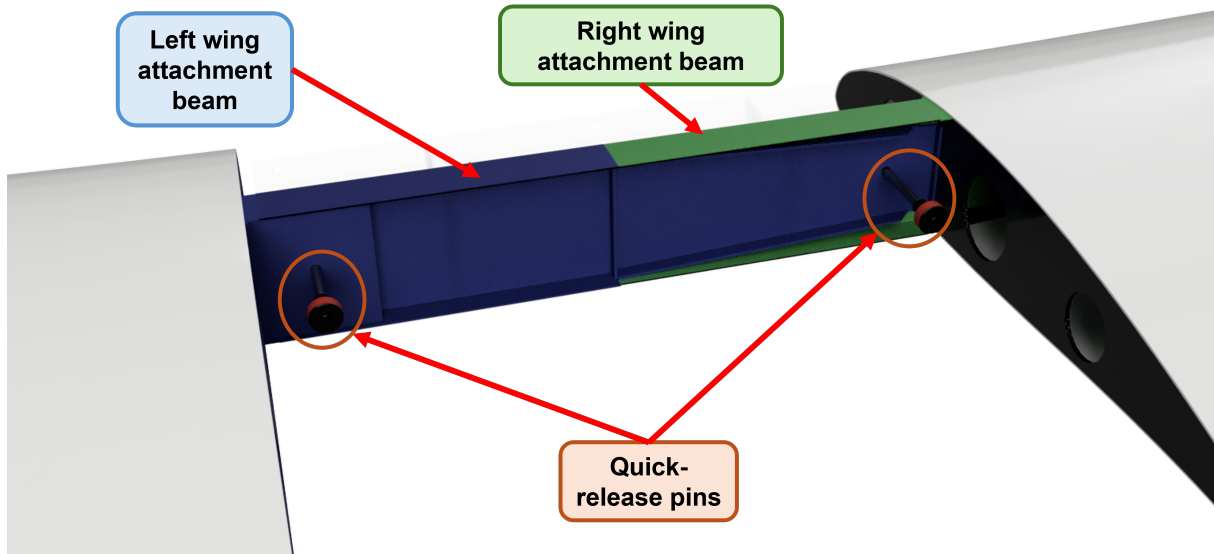


Figure 4.2: Wing attachment interface inside adapter with locking pins.

center body payload. A set of screwdrivers is included in the front payload bay to assist in removing the enclosure skin.

4.1.2 Wing Attachment and Removal Mechanism

Huma is a lift compounded SMR for the long endurance mission, so the wings are designed to quickly attach to the fuselage, and detach for the supplies delivery mission. Each wing is removed and attached separately for ease of handling and compactness. Weighing only 1.9 kg (4.3 lb) entirely comprised of carbon fiber composite, each wing is easily handled by one person.

During assembly, each wing is inserted into an aluminum rectangular channel. The I-beam spar of each wing extends beyond the wing root, reaching halfway into the adapter. The flanges of the I-beams fit tightly in the channel to prevent unwanted movement. A plate extends out of the web, past the I-beam on the opposite side of the interface as its partner plate. When the wings are attached, this plate overlaps with the I-beam of the opposite wing, shown in Figure 4.2. Both wings are secured using quick-release pins inserted into the left and right sides of the channel. Quick-release pins are ideal for rapid assembly as they can be unlocked or secured in place by pressing a single button on the pin. The interface design ensures that each pin secures both wings simultaneously. This simplifies assembly, as only two pins are needed, and provides redundancy if one pin fails in flight. To mitigate galvanic corrosion, the interior of the adapter is covered in a layer of Cerakote coating, and the pin holes are lined with a layer of fiberglass.

The adapter can be removed when the wings are not in use, providing additional space in the center body bay for the mounting of the supplies delivery payload case.

4.1.3 Removable Supply Case

For the supplies delivery mission, the payload bay is equipped with a removable supplies case made of waterproof nylon. This case can hold a payload volume of $0.2 \text{ m} \times 0.2 \text{ m} \times 0.5 \text{ m}$ ($7.9 \times 7.9 \times 19.7$ in), corresponding to 20 kg (44.1 lb) of supplies using the density specified in the RFP. The case attaches to four mounting points in the payload bay. It can be opened from the side for rapid access to the supplies at the delivery site without needing additional tools. This configuration allows the supplies to be added

or removed with the case still mounted to the aircraft.

4.1.4 Long-Endurance Fuel Tank

Given the significant difference in fuel required between the supplies delivery and long endurance missions, *Huma* stores fuel in two tanks in the lift compound configuration. One fuel tank is permanently mounted to the vehicle, forward of the front payload bay, while an auxiliary tank can be mounted to the hardpoints of the center body bay. The add-on tank shape was designed to interface with the center body bay while allowing space for the wing adapter to mount to the fuselage ceiling. The fuel tank can be refueled through a port on the vehicle's right side, allowing it to be installed when empty, making it easier to handle due to its lighter weight. This auxiliary tank is attached to the collector sump and fuel pump assembly with quick-disconnect fuel lines. More details about the tank and fuel architecture are discussed in Section 11.4.

4.1.5 Procedure for Swapping Modular Add-Ons

Specific procedures are followed to outfit *Huma* for either the long-endurance or supplies-delivery mission. These procedures are designed to be completed by two crew members within the span of 10 minutes.

For the long-endurance mission, the following steps are carried out, illustrated in Figure 4.3:

1. The crew members unlock the eight quarter-turn fasteners securing the center body bay skin, and then remove the skin. Afterwards, they remove the two panels in the enclosure skin to provide an opening for the wing spars.
2. One crew member connects the fuel tank to the collector sump using quick disconnect fuel lines.
3. One crew member supports the wing adapter on a raising dolly and raises it to the correct position in the center body bay. The second crew member then mounts the wing adapter to the center body bay mounting hardpoints.
4. The crew members each simultaneously take a single wing and insert the attachment beams into the wing adapter. After the wings are fully inserted, each person then inserts one of the two quick-release pins to secure the wings.
5. One crew member supports the fuel tank on a raising dolly and moves it into position. The second crew member then mounts it to the center body bay.
6. The fuel tank can be mounted either empty or filled with fuel. If the tank is not filled, a crew member can then fill it with Jet-A fuel using the right side fuel port. As the fuel port is covered by the center body bay skin after assembly, this step must be completed before reattaching the skin.
7. The crew members then reattach the center body bay skin.

The following procedure is completed for the supplies-delivery mission, illustrated in Figure 4.4:

1. The crew members unlock the eight quarter-turn fasteners securing the center body bay skin, and then remove the skin. Afterwards, they replace the openings in the enclosure skin with its two panels by bolting them to the structural frame.
2. One crew member supports the empty supply case on a raising dolly and holds it in the correct position in the center body bay. The other crew member then mounts the empty supply case to the center body bay mounting points.
3. A crew member then opens the payload case from the side using the case latches, and places a 20 kg (44 lbs) portion of the supplies payload inside. Afterwards, the crew member closes the case and secures the case latches.



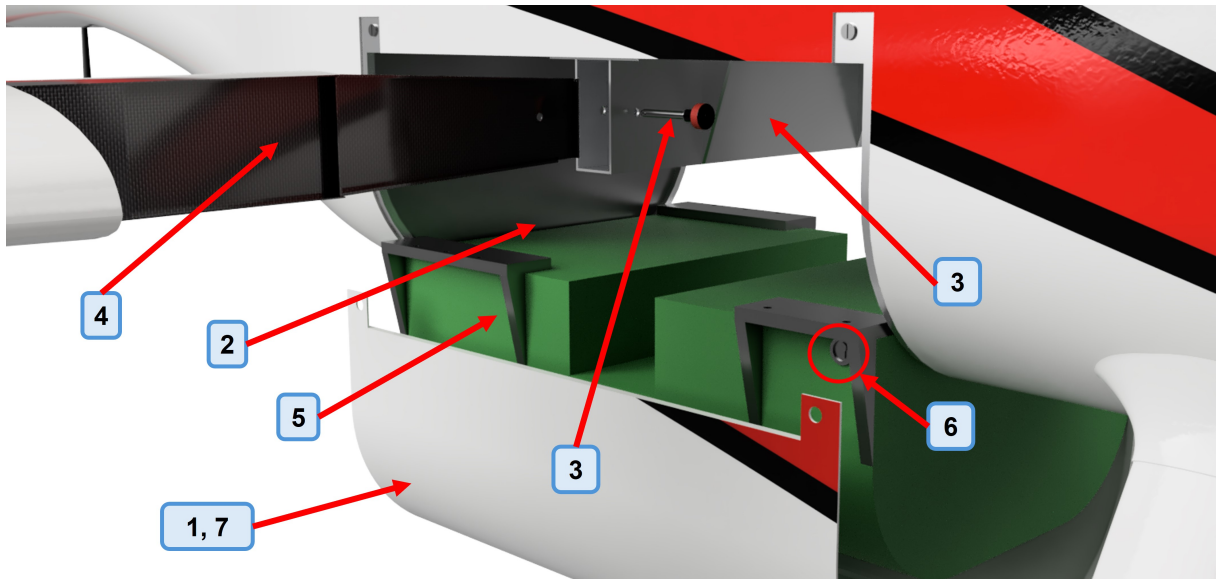


Figure 4.3: Long endurance add-on assembly procedure.

4. The crew then reattaches the center body bay skin.

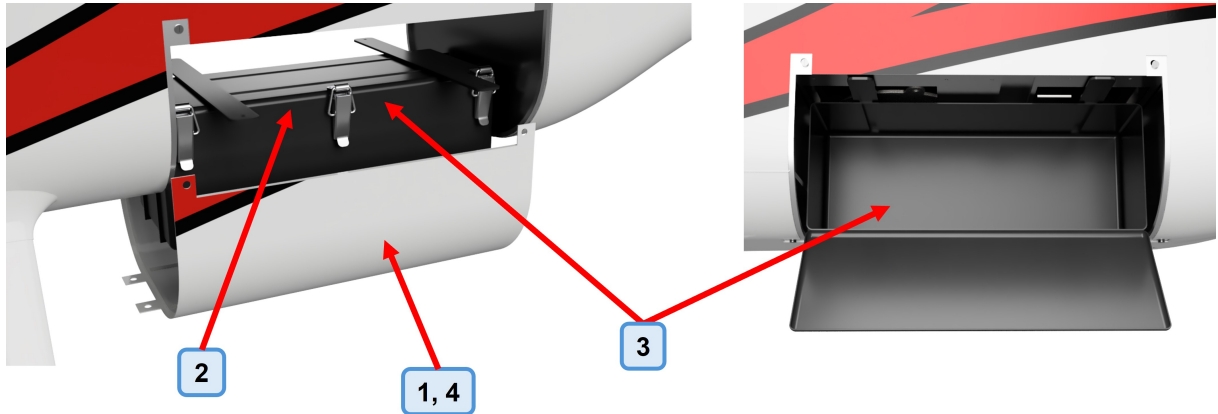


Figure 4.4: Supplies delivery add-on assembly procedure.

4.2 Front Payload Bay

Huma can be outfitted with a carrying case that expands its payload capacity, but the fuselage contains a dedicated hatch-accessible payload bay, accessible through a door in the right side of the fuselage, as shown in Figure 4.5. This compartment has enough volume to store 0.05 m^3 (1.77 ft^3) of payload by volume, with a width, height, and depth of 0.39m (1.28 ft). A forward and aft firewall separate the payload bay from the forward fuel tank and engine deck, and this bay's aluminum floor is supported by the bulkheads and longerons which mount the landing gear to the fuselage.

During the long endurance mission, the RFP prescribed 20 kg payload is stored in the forward payload bay during the mission duration. During the supplies delivery mission, the remaining 38 kg (83.78 lbs) of payload that cannot be stored in the payload carrying case is stored in the forward payload bay.



Figure 4.5: The front payload bay, opened while preparing for long endurance mission.

4.3 Vehicle Storage

Four vehicles must be stored in a $4 \times 12 \times 6$ m ($13.1 \times 39.4 \times 19.7$ ft) hangar, including all modular add-on components, as specified by the customer. Due to its modular design, *Huma* can be packed into the hangar using one of two ways: Figure 4.6 describes the storage of five aircraft in their lift compounding SMR configuration, with the modular supply payload cases stored in a corner of the hangar. If there is infrastructure in the hangar that allows for the upright storage of wings, seven aircraft and their modular add-ons can fit into the hangar in their SMR configuration, as per Figure 4.7. A castering 4-wheeled dolly helps move these vehicles across the aircraft's lateral axis, ensuring that only two crew members can easily maneuver the aircraft on a ship deck, and compactly arrange multiple aircraft in the hangar.

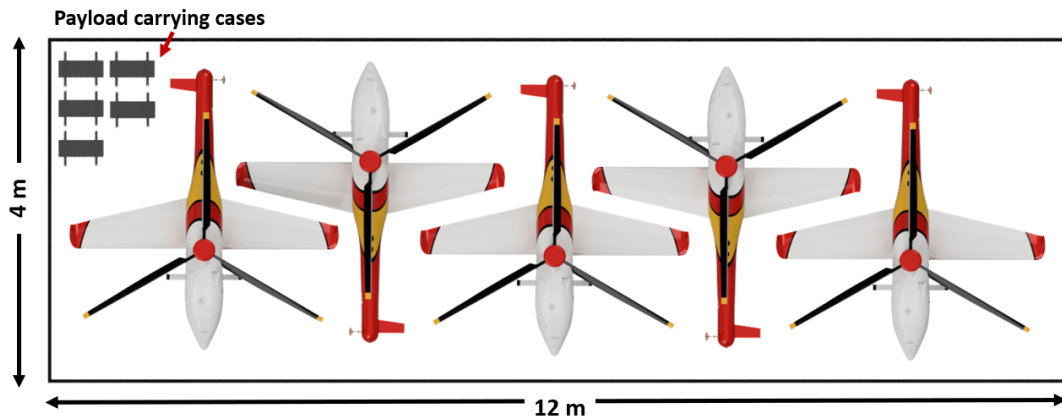


Figure 4.6: Hangar storage arrangement, lift compound configuration.

5 Blade Aerodynamic Design

The multi-configuration design makes rotor aerodynamic design especially challenging. Blade optimization was performed to maximize Figure of Merit (FM) and Lift-to-Drag ratio (L/D).

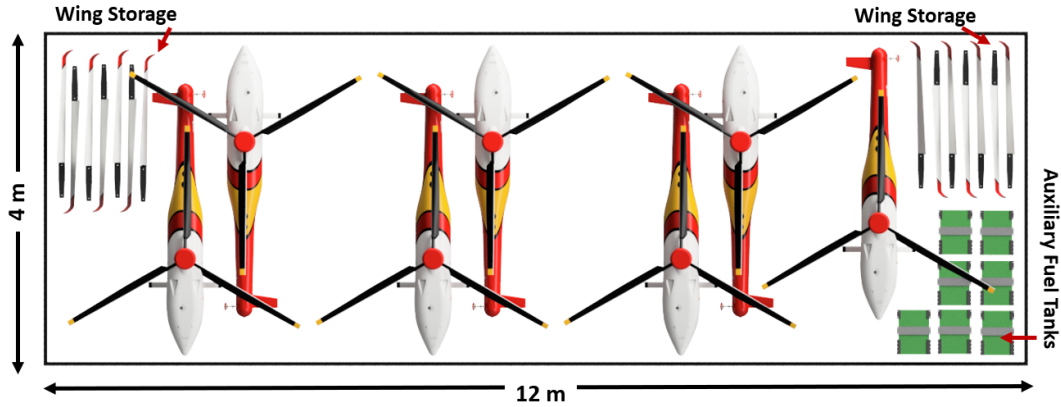


Figure 4.7: Hangar storage arrangement, SMR configuration.

5.1 Design Challenges

Traditional optimization becomes prohibitively expensive for modern designs when the configuration changes due to a vast design space. The presence of local optima poses additional challenges [15]. Achieving a balance between conflicting objectives requires a multiobjective optimized design.

5.2 An Innovative Methodology

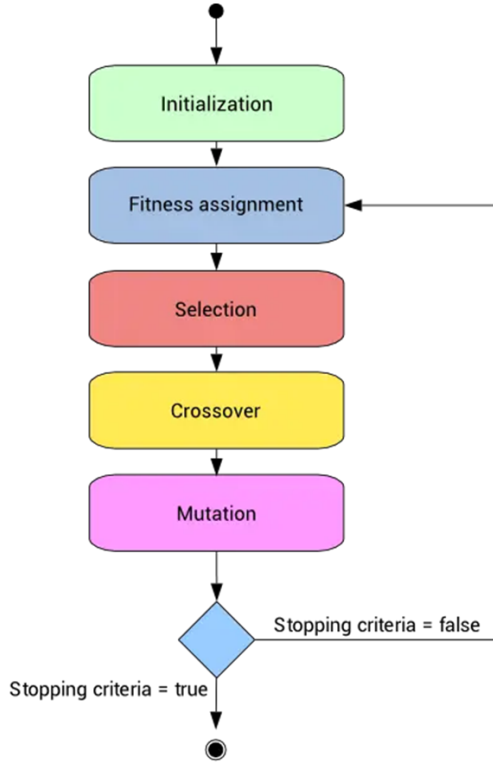
To remedy these challenges, a new and innovative approach was adopted. A Genetic Algorithm with global optimization was developed. A multi-objective optimization was employed to account for all three mission segments: hover, cruise and loiter. A code based on Blade Element Momentum Theory (BEMT) was used with the algorithm to evaluate performance parameters while mitigating computational costs with reasonable accuracy.

5.3 Genetic Algorithm

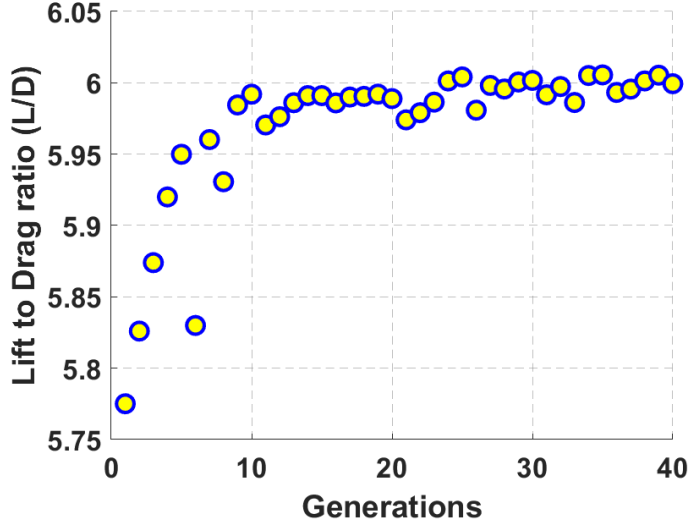
A Genetic Algorithm draws inspiration from natural selection. It begins with a randomly generated population of potential solutions. Each solution is evaluated using a fitness function. Based on these fitness scores, individuals are selected to form a mating pool, with better solutions having a higher chance of being chosen. Selected individuals undergo crossover and mutation to create a new population, mimicking genetic diversity and combining good traits. This process of selection, crossover, and mutation is repeated over many generations, allowing the population to evolve toward optimal or near-optimal solutions. The algorithm terminates when a predefined criterion, such as a maximum number of generations or a satisfactory fitness level is met [16]. The algorithm is outlined in Figure 5.1(a).

5.4 Aerodynamic Design Objective

The problem requires simultaneous optimization for three key objectives: the FM, L/D for the SMR, and L/D for the LCR. Each objective is assigned a normalized weight which influences the compromise between the competing objectives. Designers sometimes explicitly define these weights based on the relative importance of each objective. We did not restrict ourselves to a fixed set of weights; instead, we explored various combinations of objective weights. The overall combined objective was defined by Equation 2.



(a) Genetic Algorithm



(b) SMR L/D evolution through Generations

Figure 5.1: Genetic Algorithm architecture and sample results

$$J = w_1 \cdot (FM)_{\text{Lift Compound}} + w_2 \cdot \left(\frac{L}{D} \right)_{\text{SMR}} + w_3 \cdot \left(\frac{L}{D} \right)_{\text{Lift Compound}} \quad (2)$$

Here, w are the weights with $w_1 + w_2 + w_3 = 1$. The FM of the lift compound is used as it includes the effect of rotor download.

5.4.1 Design Space

To ensure optimal efficiency of the main rotor, we defined eight design variables. These were the outer and inner twist, transition location, taper, taper location, inner and outer airfoils, and airfoil transition. The upper and lower bounds for these variables were selected judiciously as shown in Table 5.1. A pool of ten rotorcraft airfoils was selected encompassing a range of thickness ratios. Constraints were imposed on solidity, maximum root chord, and minimum tip chord for structural and manufacturing considerations.

5.4.2 Navigating Tradeoffs

The normalized weight fractions were varied over a wide range to determine the best balance (Figure 5.2). For each weight fraction, and at each generation, the algorithm sampled 200 geometries. From these samples, the best geometry was selected, improving over successive generations. This process led to an optimized geometry for each weight fraction. The sequence was repeated for a range of weight fractions, providing the best geometry for each fraction. Throughout the entire blade design process, a total of 88,000 cases were executed on parallel cores to meet the design timelines and find the global best.

Table 5.1: Design space for Genetic Algorithm

Geometric Variables	Lower bound	Upper bound	
Inboard twist rate (deg)	0	20	
Outboard twist rate (deg)	0	20	
Twist junction (r/R)	0.4	0.7	
Taper ratio	1	3	
Taper location (r/R)	0.4	0.7	
	NACA0012	OA212	RC4-10
Inboard & Outboard	OA209	RC3-8	SC1012R8
Airfoils	SC1095	SSCA09	VR12
	VR15		
Airfoil transition	0.3	0.9	

For 11 different weight fractions, the 11 best performing geometries are shown in Figure 5.4. These selections led to a Pareto frontier, as illustrated in Figure 5.5. The Pareto frontier displays the best solution for each weight fraction thus further guided us to the final design selection.

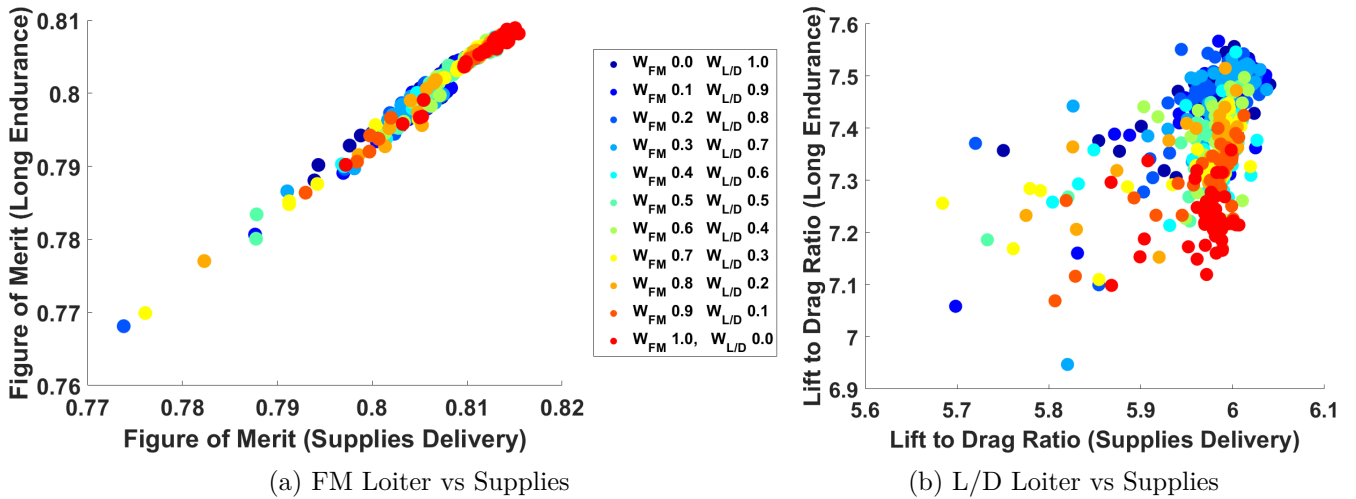


Figure 5.2: Optimization of competing objectives for multi-configuration design

5.4.3 Optimized rotor geometry

From the 11 top-performing design solutions, the one with the highest L/D for both the supplies and loiter missions was selected. This optimal geometry corresponded to a weight distribution of 0.1 for FM and 0.45 for L/D of the two modular configurations. This ratio reflected the cruise-dominated RFP missions. The optimized blade geometry is shown in Figures 5.6 and 5.7 and the variables are listed in Table 5.2.

The optimized geometry features a higher twist rate ($-18.90^\circ/\text{span}$) inboard due to low dynamic pressure and a lower twist rate ($-16^\circ/\text{span}$) in the outboard to avoid negative lift and transonic drag with transition at 0.44R. The angle of attack is higher at the root and reduces towards the tip to maintain a near-uniform spanwise inflow which helps mitigate tip losses and enhances aerodynamic efficiency.

The algorithm optimized the taper ratio such that the root chord is extended over a large radius then gradually reduced. The algorithm selected a thicker airfoil, the ONERA OA212, for the inboard regions



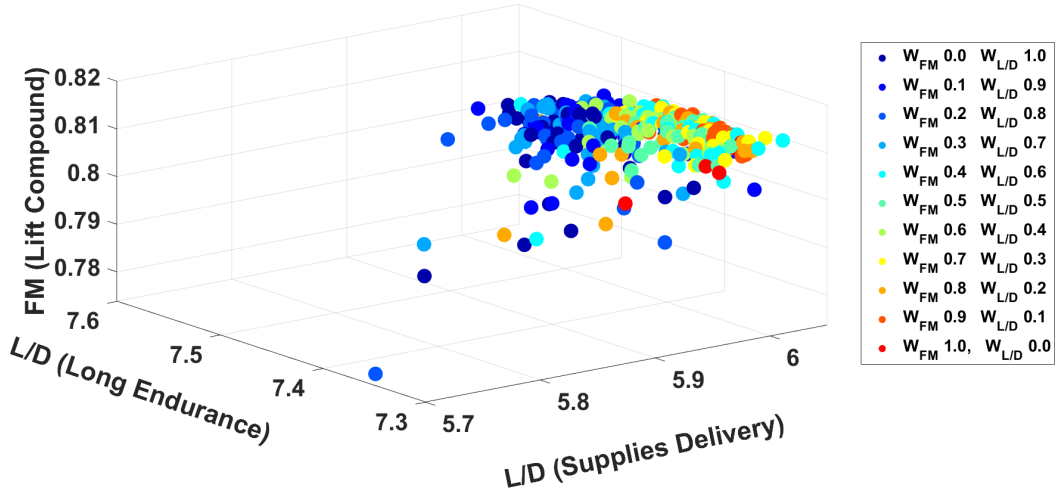


Figure 5.3: Pareto Frontier with best designs across generations

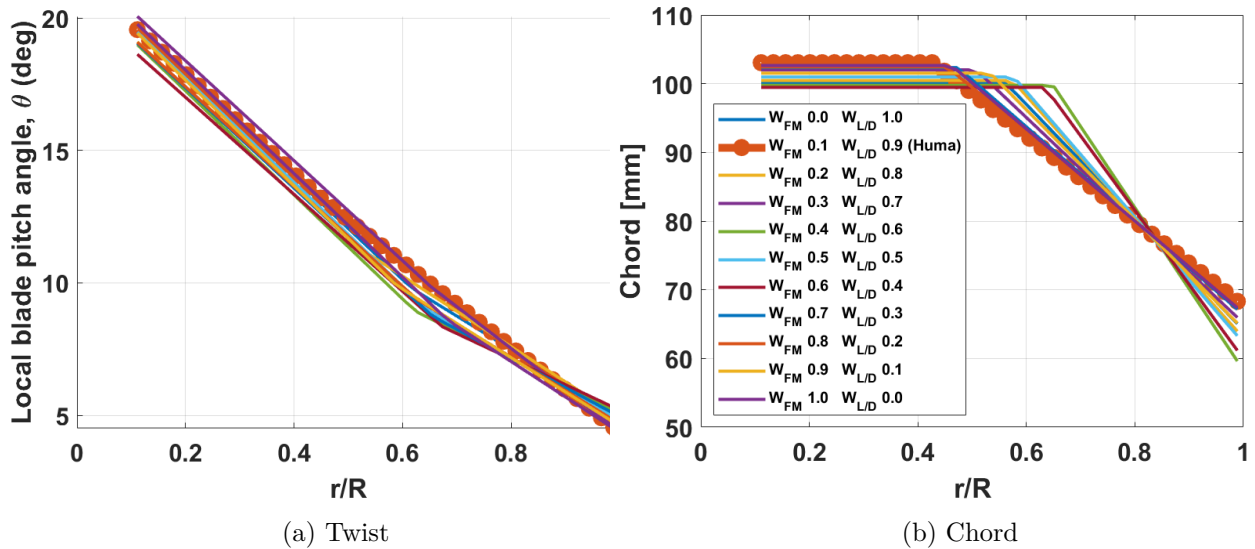


Figure 5.4: Top 11 designs and the selected best

and a thinner airfoil, the Sikorsky SSCA09, outboard with transition at 0.72R. The thicker airfoil provides better structural stiffness, whereas, the thinner airfoil extends stall margin at higher Mach numbers.

5.4.4 Optimized rotor performance

The optimized hover FM, PL, and cruise L/D were 6.01, 15.13 lb/hp, and 7.5 respectively for supplies delivery and 0.8, 14.8 lb/hp, and 7.5 for the long endurance mission. Details are provided in Table 5.3.

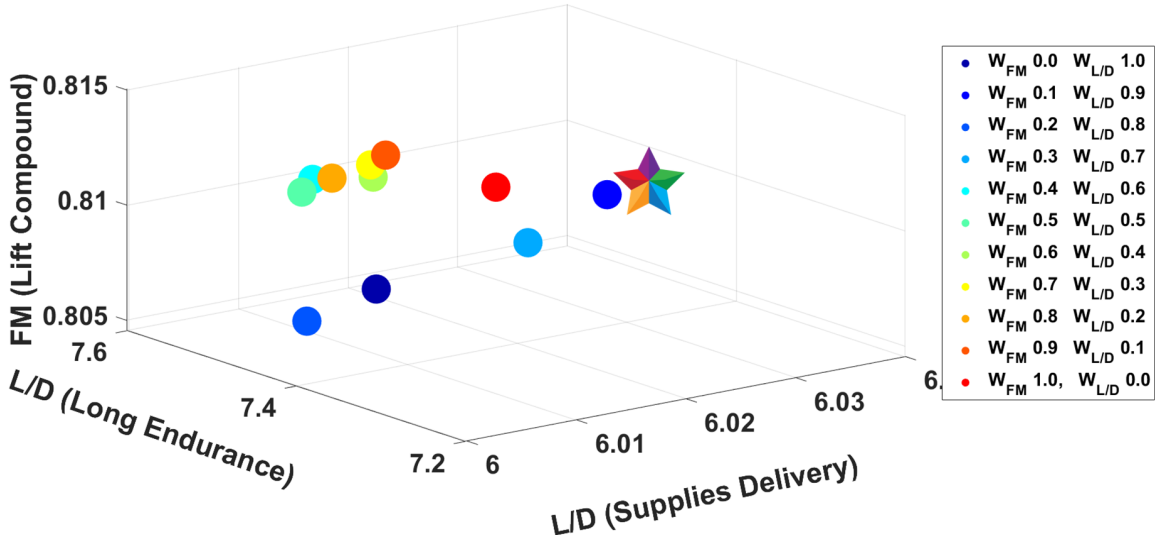


Figure 5.5: Pareto Frontier: Best weight fraction selection

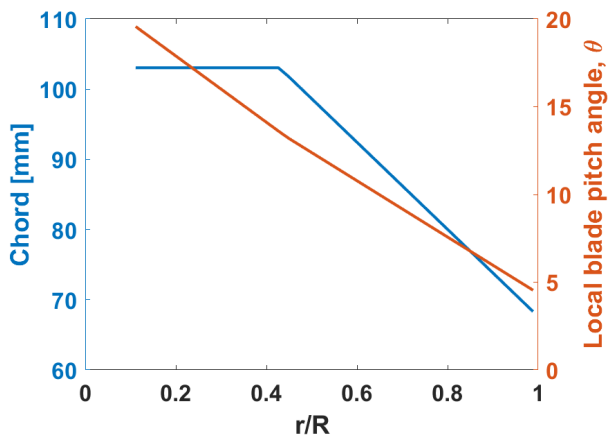


Table 5.2: Optimized main rotor blade	
Geometric Variables	Optimized values
Inboard twist rate (deg/span)	-18.90
Outboard twist rate (deg/span)	-16.06
Twist junction (r/R)	0.44
Taper ratio	1.52
Taper location (r/R)	0.43
Inboard Airfoil	OA212
Outboard Airfoil	SSCA09
Airfoil transition (r/R)	0.72

Figure 5.6: Optimized main rotor geometry

Table 5.3: Main rotor performance

Configuration	Segment	Performance	
Single Main Rotor	Hover	FM	0.81
	Cruise	PL	15.13 lb/hp
Lift Compound	Hover	L/D	6.03
	Cruise / Loiter	FM	0.80
	Cruise / Loiter	PL	14.80 lb/hp
	Cruise / Loiter	L/D	7.50

6 Blade Structural Design

Huma has a three-bladed stiff in-plane hingeless rotor. The blade structure was designed to obtain sufficient strength to carry centrifugal loads in addition to steady and oscillatory loads in flap, lag, and torsion and



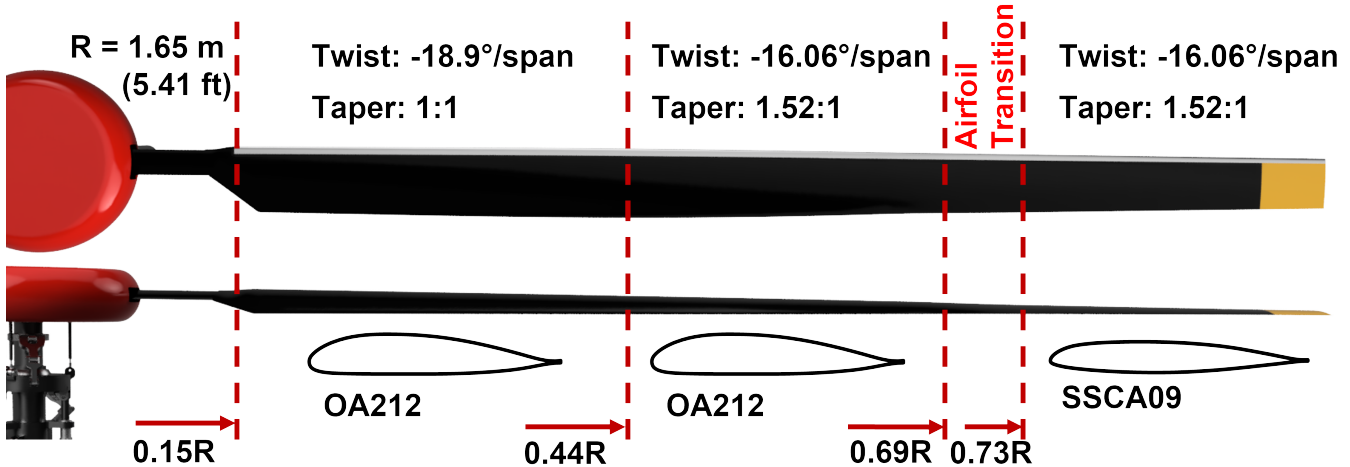


Figure 5.7: Profile of the optimized main rotor

minimize vibratory loads (2-4/rev).

The design targeted a first flap frequency of 1.08/rev and a first lag frequency of 1.4/rev to achieve good gust stability, high control bandwidth for precision ship deck operations, and immunity from ground and air resonance without an expensive elastomeric lag damper. A precone of 2° is included to reduce mean stresses in loiter.

6.1 Structure

An in-house cross-sectional analysis tool was used first to design and calculate blade stiffness and inertia along the span. This accounted for varying airfoils, skin and spar, taper and twist, tuning masses, ply orientations, and ply drop-off. Design parameters included spar shape and location, spar thickness, fillers (foam or honeycomb), leading-edge weights, and materials for all components. Leading edge weights maintained the sectional center of gravity at the quarter-chord, ensuring pitch-flap stability. Precise cross-sectional material distribution also positioned the elastic tension axis close to the quarter-chord.

The spanwise stiffness and inertial properties were inputs to UMARC-II, an in-house comprehensive analysis code that modeled flap, lag, and torsion to calculate natural frequencies and loads for both rotor operational speeds. Another in-house 3-D code, X3D, modeled the detailed internal structure with 3-D brick elements to calculate stresses and strains including local concentrations.

The final blade structure is shown in Figure 6.1. The blade grip attaches to the E-glass/epoxy flexbeam spanning from 6% to 15% of the blade radius with a small titanium insert included at the root to transfer centrifugal loads. The flexbeam transitions smoothly to the blade by wrapping around a foam core to become the blade's D-spar between the 15% to 17% blade radial stations. The primary lifting surface spans from the end of the short transition region to the blade tip to maximize the lifting area.

6.2 Root Flexbeam

A 1.08/rev flap frequency is desired to achieve precision control. A higher flap frequency was not desired due to large blade stresses, high vibration, and too rapid response to gusts. A 1.4/rev lag frequency is required to eliminate heavy and expensive elastomeric dampers and avoid the 1/rev and 2/rev resonance regions. To achieve a low part count and avoid lubrication and maintenance while obtaining the desired

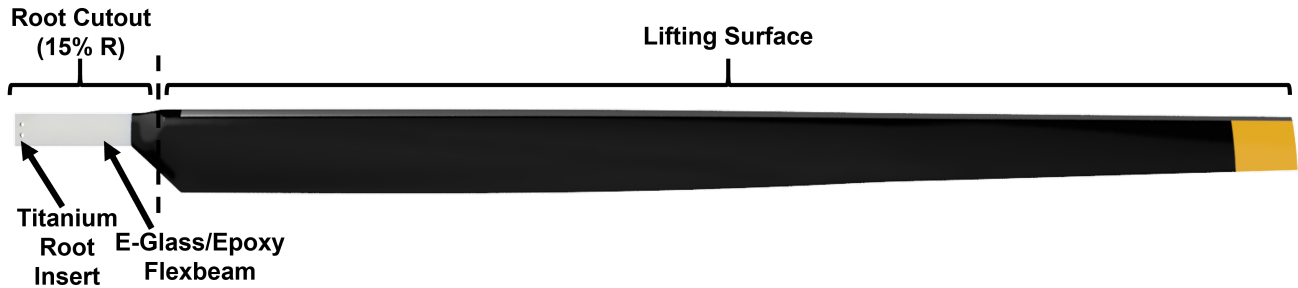


Figure 6.1: Main rotor blade top view

rotor frequencies, a root flexbeam was included. The virtual flap and lag hinges were within the carefully designed flexbeam portion of the blades. The effective flap hinge is at 12% R.

The root flexbeam is made of unidirectional E-glass/epoxy prepreg composite chosen specifically for flexibility, long fatigue life, low cost, low maintenance, and ease of manufacturing. Graphite/epoxy was not selected as it is stiff and light. The desired rotor frequencies could only be achieved with an unreasonably slender rectangular cross-section. A larger elliptical E-glass/epoxy flexbeam cross-section is desired for a smooth merge to the outboard D-spar to maintain a greater factor of safety for centrifugal force and flap and in-plane bending. The elliptical flexbeam cross-section also minimizes profile drag. This geometry also eases the transition to the outboard D-spar since the leading edge is already similar to the airfoil shape.

The root portion of the flexbeam is built up over a titanium insert with additional $\pm 45^\circ$ glass fiber plies to improve load transfer to the hub and distribute the load to the blade retaining bolts. The edge distance to the blade retaining bolt holes is greater than twice the hole diameter to alleviate stress concentration.

6.3 Internal Structure, Outboard of the Flexbeam

A cross-section view of the internal structure is shown in Figure 6.2. The D-spar is the primary load-carrying member and is made of unidirectional E-glass/epoxy prepreg. Eight plies are utilized near the root, gradually dropping off to four towards the tip, which is thinner. The same material is used for the flexbeam and D-spar to maintain fiber continuity. The D-spar provides the required torsion stiffness with a simple geometry.

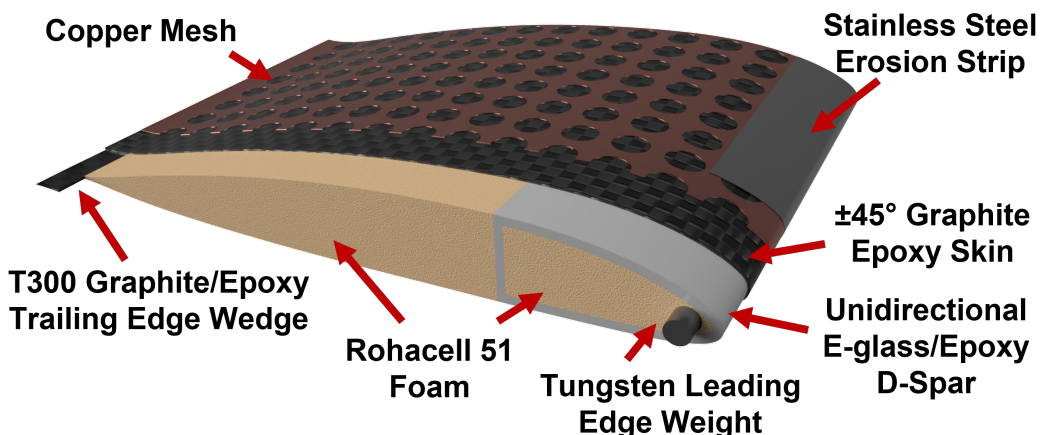


Figure 6.2: Cross-section of the main rotor blade

The outboard section of the flexbeam transitions seamlessly into the D-spar. This smooth transition is accomplished by separating the flexbeam fibers into bundles that contour around the Rohacell 51 foam tapering from within the D-spar. The transition region is depicted in Figure 6.3.

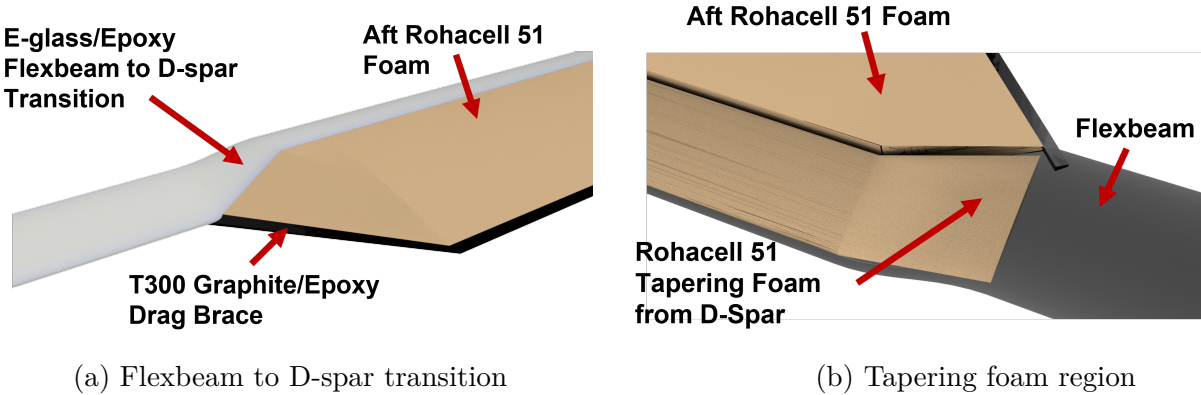


Figure 6.3: Flexbeam to blade transition

The center of gravity is maintained at the quarter-chord throughout the blade by tungsten leading edge weights placed within the D-spar. The center of gravity is pushed further ahead at 0.4R by a 65 g (0.143 lb) tuning mass which cleared the second flap mode from resonance.

The blade skin consists of two layers of $\pm 45^\circ$ T300 graphite/epoxy weaves. This provides a majority of the torsional stiffness. A trailing edge wedge of 5% chord of the same material resists skin delamination, provides lag stiffness, and acts as a drag brace at the flexbeam transition region where the lag bending moment is transferred from the blade to the flexbeam. The hollow portions within and aft of the D-spar are filled with Rohacell 51 foam to maintain the airfoil profile. This foam is lighter weight, cheaper, and easy of manufacture compared to a honeycomb material. A stainless steel erosion guard is placed at the leading edge to protect the blades from sea spray and particulates which are prevalent during ship deck operations. Stainless steel provides corrosion resistance, necessary in a marine environment. A thin copper mesh is wrapped over the blade skin to protect from lightning strikes during rough weather flight. The copper mesh allows for current to flow to the root end blade attachments to eliminate electrostatic discharge per 14 CFR 25.581 [17].

6.4 Blade Manufacturing

The blades would be manufactured following an in-house fabrication procedure.

The D-spar, flexbeam, and titanium insert are manufactured together to maintain fiber continuity. First, the leading edge Rohacell 51 foam is machined to the internal geometry of the D-spar. Slots for the tungsten leading edge weights are cut into the foam and individual weights are placed throughout the blade span. E-glass/Epoxy fiber tows are laid over the foam from the blade tip to the root, over the titanium root insert, and again from the root to tip on the blade underside to make the D-spar and flexbeam. This process is performed using automated fiber placement to capture the complex airfoil, taper, and twist profiles of the blade. Gradual ply dropoffs are included in the construction to conform to the thinner airfoil geometry near the blade tip. The entire D-spar and flexbeam assembly are cured in a mold.

The outer profile is created by the aft Rohacell 51 foam core which is molded to match the required airfoil profile and pressed to the rear of the D-spar. Automated fiber placement then lays the trailing edge graphite wedge plies. The two $\pm 45^\circ$ plies of graphite/epoxy are wrapped around the flexbeam-blade

transition region and blade lifting region. Next, a preformed stainless steel erosion guard and copper mesh are placed over the leading edge and blade skin surface respectively. Finally, the blade is placed in a mold which includes a pocket for the erosion guard.

6.5 Blade Properties

The blade weight is 0.55 kg (1.21 lb). Figure 6.4 shows the nondimensional mass and stiffness distributions of the rotor blades. The flexbeam starts at 6% span. The flexbeam decreases stiffness properties between 6% to 15% span to facilitate the required rotor frequencies. Outboard of the root cutout (0.15R), the skin, spar, and leading-edge weights determine the sectional properties. Spanwise variations in this section are due to airfoil transition, taper, and ply drop-offs.. A discontinuity in nondimensional mass (Figure 6.4(d)) is present near the 40% spanwise station due to the 65 g (0.143 lb) tuning mass.

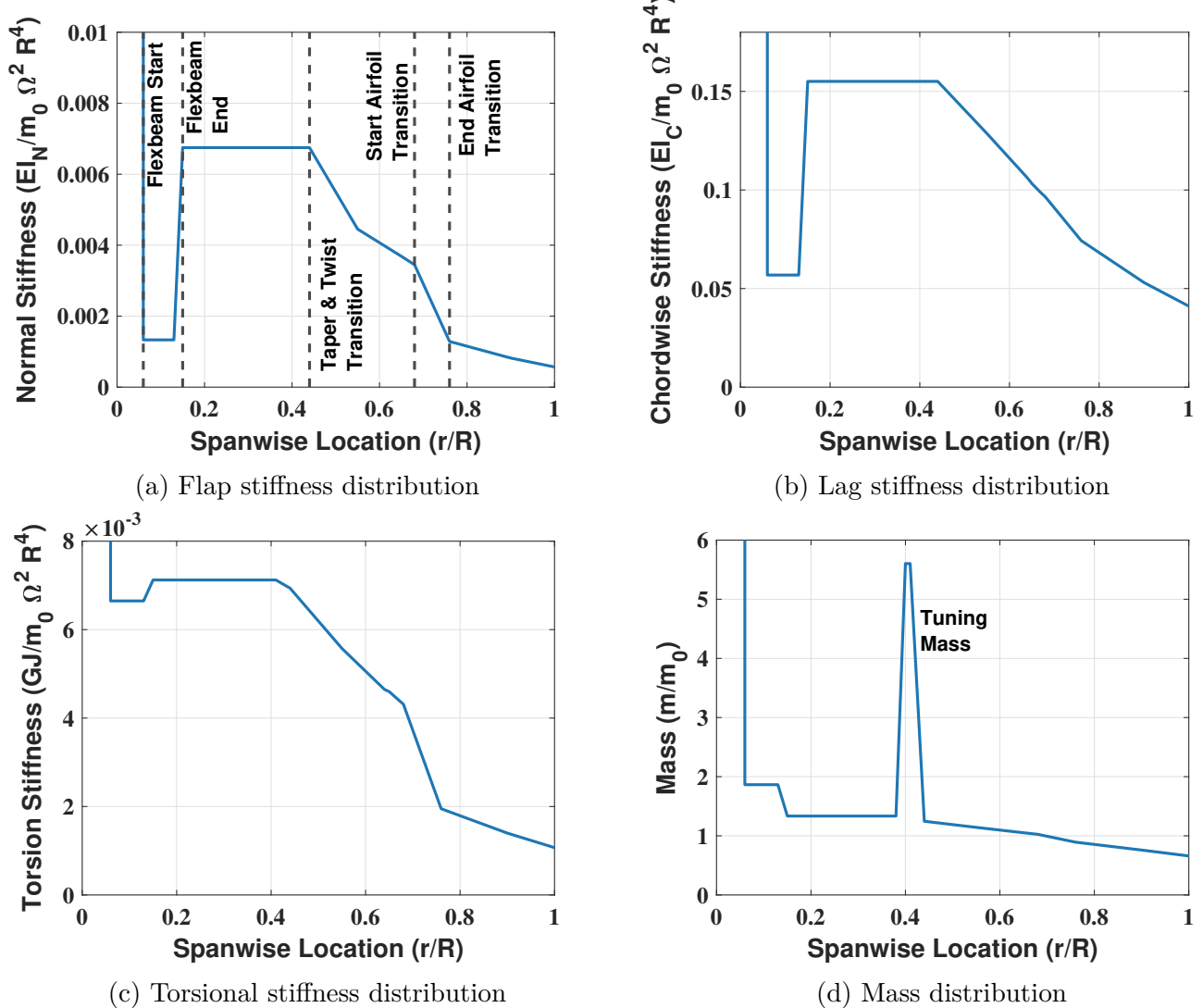


Figure 6.4: Main rotor sectional properties; Ω is rotor speed in hover

The blade sectional properties, especially the flexbeam properties, determine the blade frequencies. Figure 6.5 shows the fan plot for *Huma*'s main rotor. The rotor's first flap frequency is 1.08/rev to achieve high control bandwidth from moments for shipboard operations in gusty environments. A higher flap frequency

produced too high vibratory hub moments. The rotor is stiff in-plane with a first lag frequency of 1.4/rev to eliminate the need for any lag damper for ground and air resonance. The simple mission without any diving turns or pull-up maneuvers ensured chord loads remained acceptable. The second flap frequency was placed at 2.62/rev by the 65 g (0.143 lb) tuning mass, away from 3/rev, significantly reducing vibrations in forward cruise flight. The first torsional frequency is quite high at 9.8/rev. It helps in aeroelastic stability and the low advancing tip Mach number helps keep the pitch link loads manageable due to the lack of transonic pitching moment. The first seven natural frequencies are provided for the nominal (hover and SMR cruise) and lift compound cruise rotor speeds in Table 6.1. The modes are sufficiently far apart from all /rev crossings (rotor harmonics).

A stiff in-plane rotor system typically exhibits large hub vibratory loads. Active vibration suppression, such as the Sikorsky Active Vibration Control (AVC) system implemented on the S-97 Raider [18], uses numerous fuselage-mounted actuators to reduce vibratory loads. A weight penalty is realized due to the actuators and moving masses. *Huma* mitigates hub vibratory loads by limiting the maximum advance ratio to $\mu = 0.26$ in the fast outbound cruise mission segment when slowing the rotor. Wing lift sharing in cruise also significantly decreases hub vibratory loads. In-house Mach-scaled wind tunnel test of the Maryland compound rotor rig observed a 30% reduction of in-plane hub vibratory loads with wing lift sharing for the very stiff in-plane rotor [19].

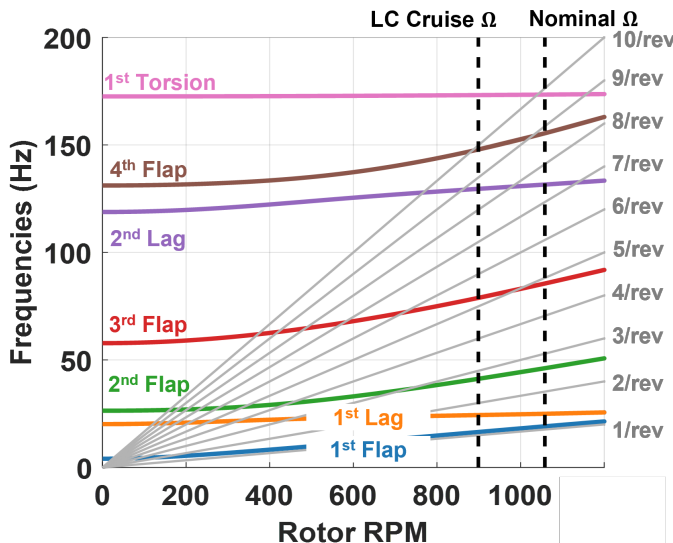


Figure 6.5: Fan plot of the main rotor

Table 6.1: Blade frequencies at nominal and lift compound cruise rotor speeds

Mode (/rev)	Nominal Ω 1058 RPM	LC Cruise Ω 899 RPM
1st Flap	1.08	1.10
1st Lag	1.42	1.63
2nd Flap	2.62	2.75
3rd Flap	4.85	5.26
2nd Lag	7.46	8.65
4th Flap	8.82	9.87
1st Torsion	9.83	11.56

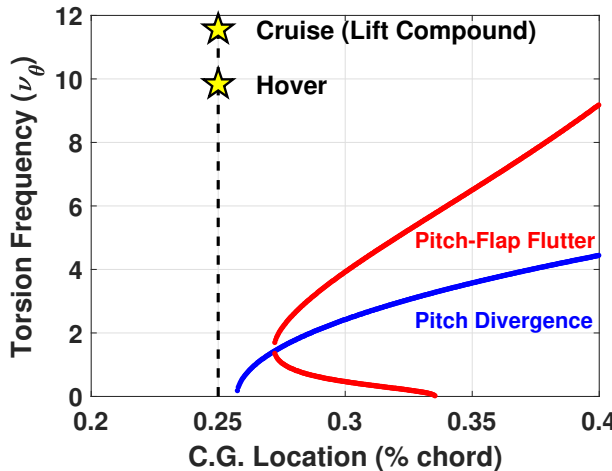
6.6 Aeroelastic Stability Analysis

Aeroelastic stability analysis included flap-lag, pitch-flap, ground resonance, and air resonance to ensure that the rotor is stable in all phases of flight with adequate margins.

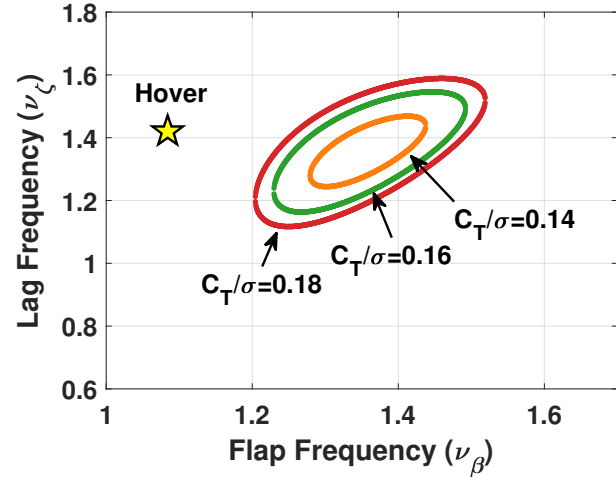
Pitch-flap flutter is a dynamic instability caused by lift and centrifugal coupling from C.G. offset from the pitch axis. Both of these instabilities are effectively eliminated by placing the pitch axis at the quarter-chord and C.G. at or ahead of it. Figure 6.6(a) shows the stability boundaries for pitch divergence and pitch-flap flutter as a function of chordwise C.G. location and torsion frequency. *Huma* is free from both instabilities.

Rotors that are stiff in flap and lag are susceptible to flap-lag flutter at high blade loadings. Figure 6.6(b) shows that *Huma* is well clear of the instability boundaries even for high blade loadings. Therefore the

blades will stall before any of these instabilities are encountered. Any chance of stall flutter is also mitigated by the high torsion frequency. The rotor is stable from this instability in the operating flight envelope.



(a) Pitch-flap stability boundaries



(b) Flap-lag stability boundaries

Figure 6.6: Pitch-flap and flap-lag aeroelastic stability margins

Ground resonance is an explosive instability caused by the coupling of the fuselage/landing gear modes with the rotor in-plane modes. Avoidance of this mode is critical for vehicle and ground crew safety on a small ship deck. This instability is typically solved by adding lag damping for soft in-plane rotors. Ground resonance avoidance is particularly challenging for the missions outlined in the RFP due to the significant weight differences between takeoff and landing, necessitating significantly different levels of lag damping. Wet ship deck environments offer nearly zero Coulomb damping, and *Huma*'s three-point landing gear, functioning as leaf springs, further reduces structural damping. To counter all of these challenges, the rotor is designed to be stiff in-plane ($\nu_\zeta > 1/\text{rev}$) and eliminates the need for a lag damper. In turn, higher fidelity 3D stress analysis tools were crucial for assessment of in-plane stresses. The lag frequency of 1.4/rev kept the lead-lag bending stresses well below material limits [20].

6.7 3-D Stress Analysis

The rotor blade was stress-tested using the in-house solver X3D [21]. This solver uses three-dimensional (3D) finite elements to model the structure from first principles and capture the dynamic stresses. The rotor frequencies were also calculated using X3D which were similar to the beam-based calculations shown in Figure 6.5. The analysis was conducted at various flight conditions, but the results are only shown for the SMR at the maximum speed of 41 m/s (80 knots) where the highest stress concentrations were encountered.

Figure 6.7 shows the axial (bending) stress distribution along the blade. Three cross-sections are highlighted at 18% R, 53% R, and 75% R. The first and the last cross-sections correspond to two different airfoils with 12% thickness-to-chord ratio at the root and 9% near the tip. High compressive stresses are observed on the top surface near the root, with the bottom surface having high tensile stress due to blade lift. There is some tensile stress concentration at the top surface of the blade near the mid-span due to the blade pre-cone (2°). The maximum tensile stress in the spar is approximately 280 MPa, which gives a factor of safety over 5.

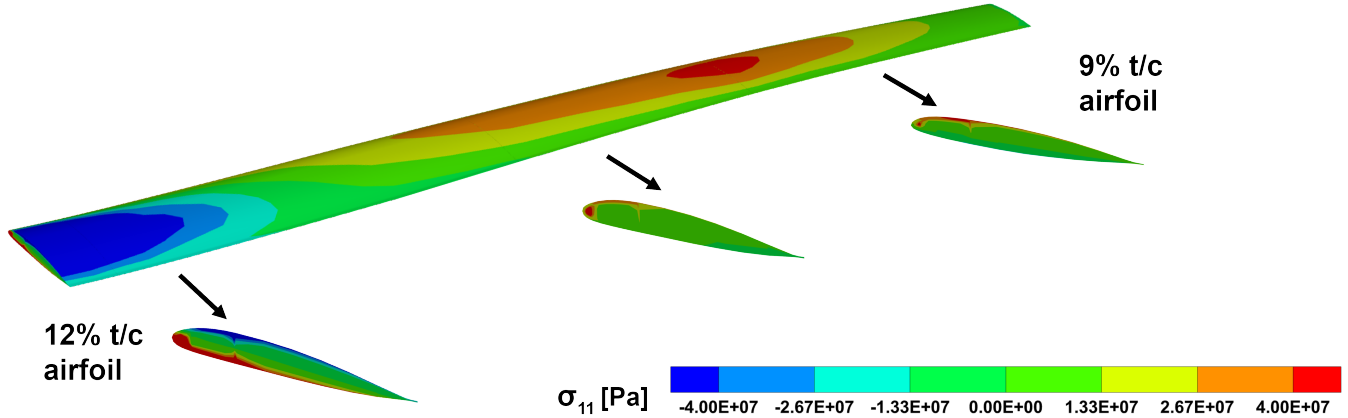


Figure 6.7: 3-D Stresses analysis in forward flight (80 knots) using X3D

7 Hub Design

The main rotor hub primarily retains the blades, allows motions, absorbs loads, and transmits the loads from the blades to the shaft. The hingeless hub achieves the following goals: 1) simple geometry and lower part count for lower manufacturing costs and easier maintenance; and 2) compact design and cleaner shank for low hub drag in loiter. The hub was designed to withstand steady and oscillatory loads with a fatigue life of over 5,000 hours.

7.1 Hub Selection

Four widely used rotor hub types were considered using seven selection criteria: gust sensitivity, control authority, part count, weight, vibratory loads, hub drag, and maintenance requirements. Shipboard operations require precise high-bandwidth control in high wind and gusts. Low weight and drag are critical to maximize vehicle performance for both mission profiles. A low part count decreases part manufacturing and maintenance costs and time. Low hub vibrations ensure minimal noise in avionics sensor data. Table 7.1 shows the hub selection matrix. The hubs were rated on a scale of -1 (poor) to +1 (good).

Table 7.1: Hub type selection matrix

Hub Type	Gust Sensitivity	Control Authority	Parts Count	Weight	Vibration Level	Hub Drag	Maintenance	Total
Articulated	1	-1	-1	-1	1	-1	-1	-3
Semi-Articulated	0	0	0	0	0	0	0	0
Hingeless	-1	1	1	1	-1	1	1	3
Bearingless	0	0	0	1	0	0	1	2

Articulated: Articulated hubs require mechanical hinges in the flap, lag, and pitch axes. The hinges increase part count, weight, complexity, and forward flight drag. Additionally, typical hinge offsets produce flap frequencies of 1.03-1.06/rev which limits control bandwidth needed in gusty shipboard environments.

Semi-Articulated: Semi-articulated hubs are rigid in lag and use elastomeric bearings for pitch and flap. This hub has increased flap stiffness compared to the articulated hub. However, elastomeric bearings are undesirable for use in marine environments due to degradation from seawater [22].

Hingeless: Hingeless hubs use flexures for flap and lag while retaining a bearing for pitch control. Higher

control bandwidth is achieved from flap frequencies near 1.1/rev at the expense of higher vibratory loads. Hingeless hubs have a low part count and hub drag. They are compact and can be hidden within a hubcap or fairing due to a cleaner shank. Modern CAD-based digital design allowed careful property and frequency placement to relieve aeroelastic couplings that would prevent high stresses and the need for elastomeric dampers. The hingeless hub design was selected due to its simplicity, low hub drag, and high control bandwidth.

Bearingless: Bearingless hubs are essentially hingeless hubs with a lag damper. They typically require a torque tube to house the snubber damper. For a large helicopter, a 1.4/rev lag frequency would be too high for loads and call for a bearingless design when reduced below 1/rev. A 1.4/rev lag frequency is acceptable for a small UAS like *Huma*. Moreover, a snubber damper is very expensive and gets severely degraded by seawater.

7.2 Hub Assembly

The hingeless hub assembly is shown in Figure 7.1. Major components include the aerodynamic fairing (hubcap), the hub yoke, pitch cases, tension-torsion straps, scissors, swashplate, pitch links, and the splined rotor shaft. The mast retention bolt secures the hub assembly to the main rotor shaft and is secured by threading in the direction of rotor rotation. It includes a corrosion-resistant wedge-lock mast retention washer that acts as a positive locking device, preventing the bolt from loosening due to vibrations [23]. This bolt also retains the hubcap fairing mount. An eye bolt can be used in place of the mast retention bolt to facilitate crane operations on a ship deck. The rotor shaft securely attaches to the hub yoke using a splined interface, as shown in Figure 7.2(a). The simple hub yoke attaches to a standard cylindrical pitch case by a polyether urethane tension-torsion strap with a steel wire core to resist centrifugal loading while allowing pitch motion with the radial and thrust bearing stack. Titanium Ti-6Al-4V alloy was selected for the hub yoke and pitch cases due to its high fatigue life, high strength-to-weight ratio, and high corrosion resistance. The pitch horn is built into the pitch case and is laterally offset to enable +23°/-10° of collective range and ±20° of cyclic range. There are no pitch-flap or pitch-lag couplings. These components enable the hub structure to be clean, compact, light, and low-maintenance. A 2° pre-cone is included to reduce steady stresses in hover in hover and loiter.

7.3 Swashplate Design

Huma's small UAV scale prompted a dedicated design study for the selection of a control actuation technique. Torsionally flexible blades can be used for swashplate-less control, reducing some hub weight and forward flight hub drag. Techniques include trailing edge flaps [24] or blade twisting controlled by hub pitch and shaft rotational speed [25]. These methods rely on a very low torsion frequency, reducing aeroelastic stability, and are not yet mature. Low technology readiness levels and high bandwidth control requirements in gusty environments make these methods unsuitable. Individual blade control (IBC) mechanisms using either hydraulic actuators or piezoceramic pitch link actuators were also considered. These methods require high-frequency actuation within the rotating frame, resulting in large and heavy power conditioning that undermined the goal of a low empty weight fraction. The traditional swashplate mechanism was selected for *Huma* as it is proven and time-tested for robustness and reliability.

Huma's swashplate provides collective and cyclic control. The system is shown in Figure 7.2. The swashplate is attached to a collar built into the shaft. An aluminum spherical bearing is placed around the collar with a low-friction sleeve between both components for the collective and cyclic degrees of freedom. The non-rotating swashplate is secured to the exterior of the spherical bearing and houses a tapered roller bearing. The rotating swashplate is divided into two halves to affix securely to the tapered roller bearing. Rotating scissors attached to the upper swashplate and rotating fastener alleviates bending and shear loads





Figure 7.1: Hingeless hub assembly

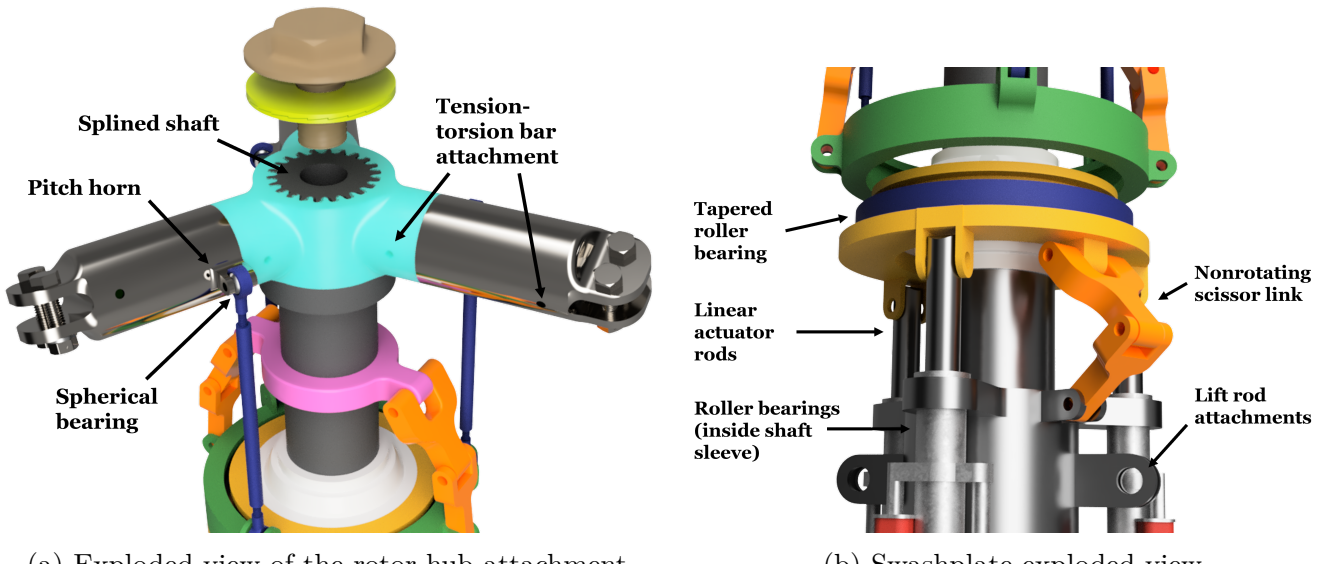


Figure 7.2: Rotor hub and swashplate exploded views

on the pitch links. A nonrotating scissor linkage attaches the entire swashplate system to a lower shaft collar to constrain the nonrotating parts of the system from rotating with the rotor. To ensure a low-drag profile and minimize bending loads on the assembly, the swashplate, scissor linkages, and pitch links were located as radially close to the shaft as possible to fit the entire assembly within the aerodynamically efficient pylon and hubcap fairing.

7.3.1 Swashplate Actuators

Huma is an unmanned aircraft and cannot rely on the traditional mechanical actuation from a pilot for swashplate control. Therefore, small electro-mechanical cylinders (EMC) and electro-hydrostatic actuators (EHA) were considered to actuate the swashplate. EMCs rely on a ball-screw assembly and are generally smaller in size than EHAs but have a much lower power-to-weight ratio, actuation speed, and maximum stroke length. EMCs, such as the UltraMotion AM series actuators used on the Maryland Tiltrotor Rig, typically require liquid cooling which adds weight. Ample space is available around the rotor shaft below the swashplate, allowing for the installation of three miniature electro-hydrostatic actuators which are fully self-contained [26]. The high actuation rate allows traversal of the full 33° collective range within one second. The high-bandwidth actuators ensure flight stability in gusty environments. The actuators are attached 120° apart to the shaft support collar as shown in Figure 7.3. The collar assembly is also the component that transfers hub loads to the fuselage bulkheads using lift rods.

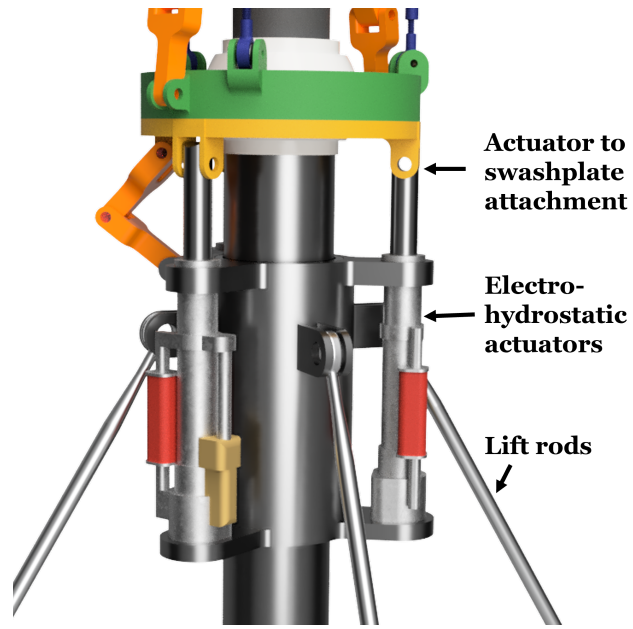


Figure 7.3: Swashplate actuators attached to the shaft support collar

The actuators are attached 120° apart to the shaft support collar as shown in Figure 7.3. The collar assembly is also the component that transfers hub loads to the fuselage bulkheads using lift rods.

8 Wing Design

A fixed wing is aerodynamically more efficient than a rotor but limitations arise in terms of structural weight, design modularity, and high shaft tilt angles. To harness the overall advantages of a wing, detailed design was imperative. This includes lift sharing between wing and rotor, structural design, structural attachments, and wing flutter.

8.1 Lift Sharing and Shaft Tilt Angle

In the absence of a pusher propeller, the lift share of a wing is dictated by the rotor shaft tilt angle. Allocating a high proportion of lift to the wing leads to a high rotor shaft tilt angle to generate thrust. The required thrust also increases due to wing drag. A high shaft tilt angle introduces several significant disadvantages. It increases aerodynamic drag, requires more power to maintain altitude and speed and imposes greater vibratory loads on the airframe.

For a low to moderate shaft tilt angle (less than 8°), the lift share set at 48% for the wing. This allocation guided wing loading and airfoil selection. A careful selection not only alleviated wing structural weight but also ensured compliance with storage and dimensional constraints.

8.2 Airfoil Selection

The initial pivotal step involved the meticulous selection of the airfoil. After scrutinizing well-known airfoils, a pool of 7 low-speed airfoils (Figure 8.1) was shortlisted, prioritizing high C_l/C_d , and low pitching

moment at the required wing loading. Subsequently, CFD simulations were conducted using an in-house solver for each airfoil to analyze their performance plots, as shown in Figure 8.2. Analyzing the data revealed FX-63137 airfoil as the optimal choice by virtue of its aerodynamic efficiency and minimal drag.

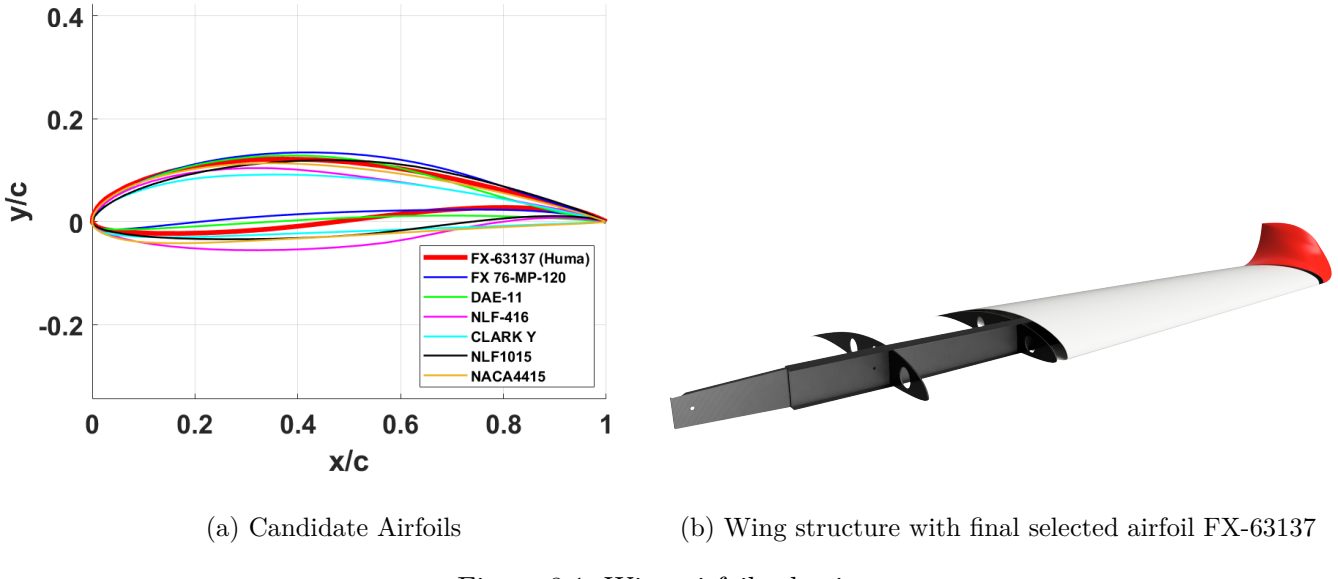


Figure 8.1: Wing airfoil selection

8.3 Geometric Considerations

Several factors were considered for the wing planform design such as aerodynamic performance, ease of manufacturing, and structural advantages. The wing planform with a 2:1 taper was selected to supplement the airfoil efficiency with an approximate elliptical lift distribution across the span and reduce the root bending moment, hence lower structural weight. For the same purpose, a straight leading edge with a tapered trailing edge was chosen. The wing was given a 2° dihedral angle to enhance stability. The wing incidence was set to 4° to meet the necessary lift for loiter. The airfoil was selected to provide the highest lift-to-drag ratio at this incidence. To mitigate undesirable edgewise flow, winglets were added. The winglets were designed as blended tips to reduce the strength of the recirculating vortices with minimal skin friction penalty [27].

8.4 Wing Structural Design

The structural design of *Huma*'s wing focused on modularity and prevention of flutter. The internal structure must be designed to withstand loads up to 3.5g according to the U.S. Navy AR-56 structural design requirements for helicopters [28]. The wing spar is the primary load-bearing structure. A comparative study of the spar cross-section determined an I-beam to have an advantage over other cross-sections, such as C-channel spars and box beams, due to its high stiffness-to-weight ratio. The spar is located at the quarter chord throughout the wing span and is cantilevered to the fuselage at the wing adapter within the center body bay.

The material selection process for the wing internal structure was driven by the following goals: low weight, high stiffness, and exceptional corrosion resistance in marine environments. Composites were selected over metal due to their high specific stiffness.

Classical laminate theory and static load analysis were used to determine the ply orientation and spanwise thickness of the I-beam spar. The flanges were designed with a symmetric composite layup of [+45/-45/0/-45/+45] T300 graphite/epoxy. The web was designed with a composite layup of unidirectional plies of

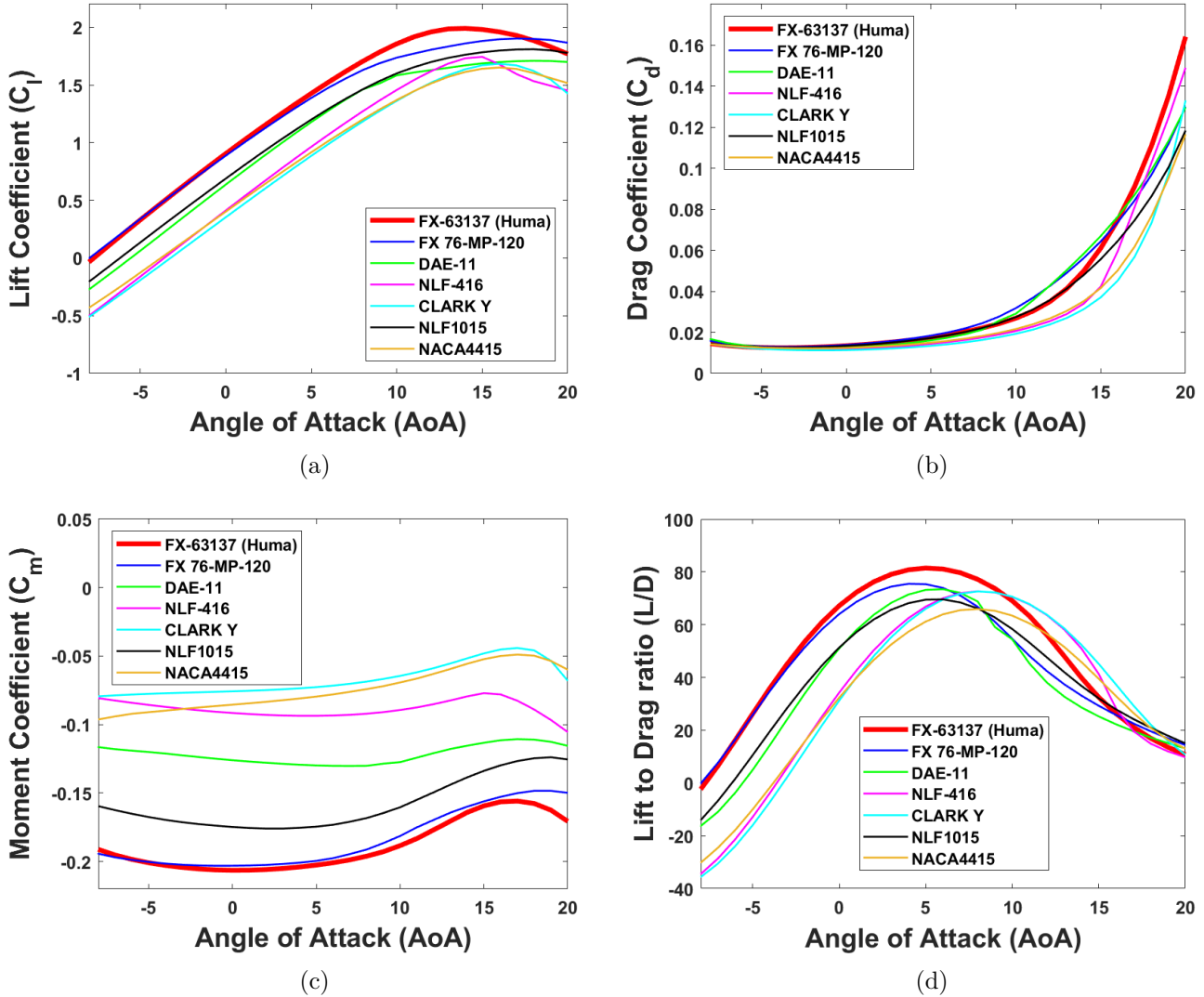


Figure 8.2: Performance curves of selected airfoils

the same material. This ply orientation provides high bending stiffness to resist flutter. The skin provides sufficient torsional stiffness with two plies of $\pm 45^\circ$ woven T300 graphite/epoxy. The ribs are placed at five equidistant locations and maintain the wing's airfoil cross-section.

8.5 Finite Element Analysis

A finite element analysis was performed to determine the static loading characteristics of the composite wing structure. The root of the spar has a clamped boundary condition and the aerodynamic loads were distributed across the wing span. The analysis was carried out using a load factor of +3.5g at the 41 m/s (80 knots) cruise speed. The internal structure has a factor of safety of 2.1 in bending according to the Tsai-Wu failure criterion [29]. Figure 8.3 shows the stresses on the composite wing spar.

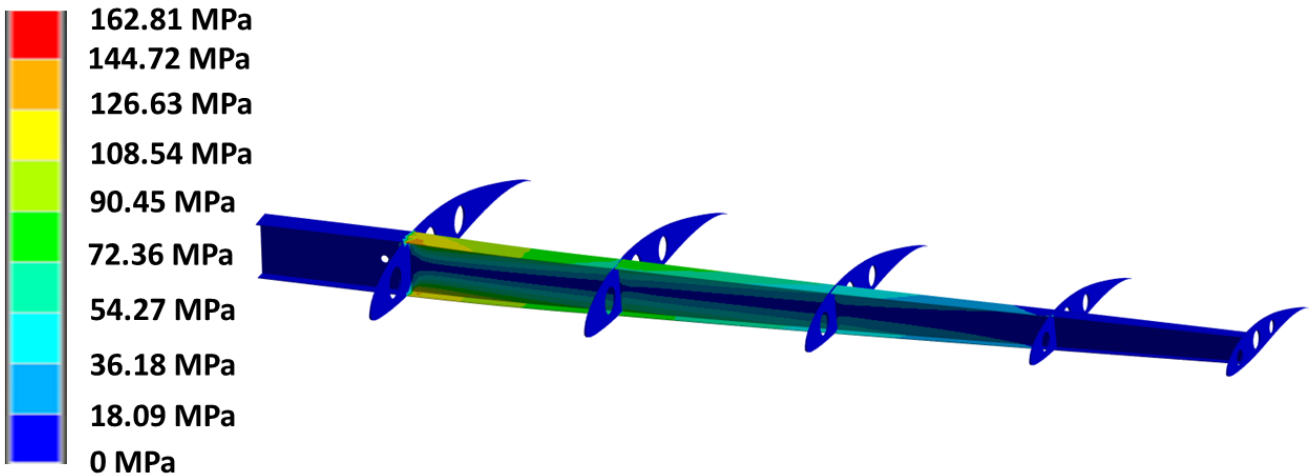
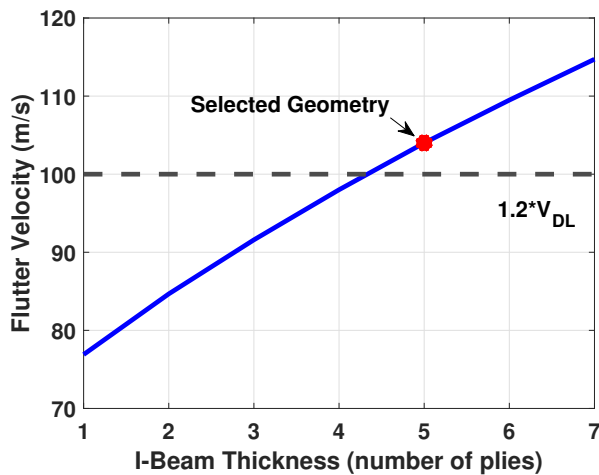


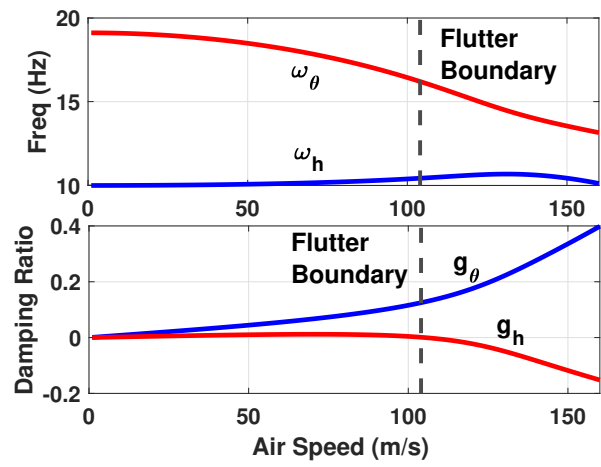
Figure 8.3: Finite element analysis of Composite wing spar

8.6 Aeroelastic Analysis

An aeroelastic analysis was performed to determine the flutter and divergence characteristics of the wing design. The wing was analyzed as a cantilevered beam in bending and torsion under unsteady aerodynamic loads, inertial loads, and elastic loads [30]. To achieve a minimal wing weight, the thickness of the wing spar was studied as a function of number of plies. Figure 8.4(a) depicts the flutter velocity with wing spar thickness varying from 0.2 mm to 1.4 mm. The velocity calculated at each thickness is compared with V_{DL} , as the flutter speed should be greater than 1.2 times this velocity to ensure adequate aeroelastic stability margins [31]. A spar with a five-ply thickness was selected to meet the stability criteria while minimizing weight and thickness. The wing flutter speed is 104 m/s (202.2 knots) and the divergence speed is 139 m/s (270.4 knots). The frequency damping plots are seen in Figure 8.4(b). As such, the wing is free from any aeroelastic instability in the flight envelope.



(a) Flutter Velocity vs Wing Spar Thickness



(b) Aeroelastic study results

Figure 8.4: Aeroelastic analysis of the wings

9 Tail Rotor Design

The high winds and gusts associated with shipboard operations were a challenge for tail rotor design. The important design considerations were yaw authority under cross and tail wind, low power, resistance to vortex ring state (VRS), and simplicity for low cost and ease of manufacturing. The design process resulted in a 2-bladed teetering tail rotor with twisted and tapered blades.

9.1 Tail Rotor Sizing

The tail rotor geometry was selected with momentum theory and the AFDD tail rotor weight estimation model to ensure effective anti-torque and yaw control in all flight segments. Torque and yaw control requirements were set by vertical climb and descent mission segments since the vertical stabilizer fully offloads the tail rotor at 41 m/s (80 knots) for the lift compound configuration.

9.1.1 Diameter

A crosswind from the right (90° azimuth) puts the tail rotor in a climb state requiring increased collective which may lead to blade stall [32]. A crosswind from the 270° azimuth can potentially lead to the loss of tail rotor effectiveness from vortex ring state [33]. With a set tail rotor tip speed and moment arm from the main rotor, the tail rotor inflow velocity directly depends on the diameter. Table 9.1 presents the maximum crosswind from the 270° azimuth that the tail rotor can withstand before entering a vortex ring state. Losses due to flow blockage from the tail boom and vertical stabilizer are included as a 10% greater thrust requirement. A smaller tail rotor is beneficial for delaying the onset of vortex ring state but requires more power than a larger rotor. A small diameter tail rotor increases blade loading and decreases the stall margin for a crosswind. *Huma's* tail rotor, with a 0.63 m (2.07 ft) diameter, was designed to provide a 10% margin over the RFP's 8 m/s (16 knots) maximum crosswind requirement.

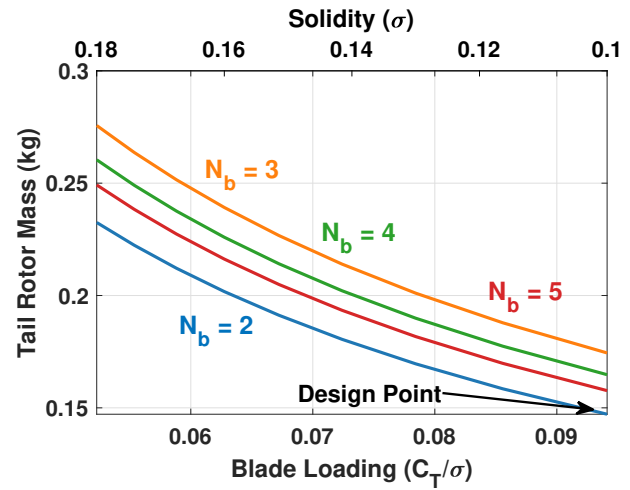


Figure 9.1: Tail rotor mass versus blade loading

Table 9.1: Tail rotor diameter trade study

Radius	Max. Steady Wind	Rotor RPM	TR to MR Power
$0.25R_{MR}$	6.7 m/s (13.0 knots)	4213	7%
$0.19R_{MR}$	8.8 m/s (17.1 knots)	5530	8%
$0.17R_{MR}$	10.1 m/s (19.6 knots)	6320	9%
$0.14R_{MR}$	11.8 m/s (22.9 knots)	7373	10%

9.1.2 Solidity

Figure 9.1 shows the effect of tail rotor solidity on blade loading and tail rotor weight. At this small scale, the number of blades generally decreases weight except for the 2-bladed teetering hub. Even though blade loading decreases with higher solidity, the weight increase is quite significant. Hence, a 2-bladed teetering rotor with a solidity of 0.01 was selected for a sufficient blade stall margin and high yaw control authority.



9.1.3 Tip Speed

The tail rotor tip speed was selected to be the same as the main rotor. A lower tip speed would decrease rotor noise but this would come at the undesired cost of higher drive shaft torque and weight [34]. The 600 ft/s tail rotor tip speed corresponds to a rotation speed of 5530 RPM, which is comparable to the engine's RPM of 6000. Consequently, only minimal gearbox reduction is required, thereby reducing the overall weight needed to achieve the proper tail rotor speed.

9.2 Aerodynamic Design

The tail rotor blade aerodynamics design process mirrors that of the main rotor blade, though with fewer design variables. In this streamlined approach, the number of design variables was reduced to three: one twist, one taper, and one airfoil. The airfoil selection was thicker to accommodate a spar. The optimized parameters from the genetic algorithm (Figure 9.3(a)) are the OA212 airfoil with a 12% thickness, a twist of $-15^\circ/\text{span}$, and a taper of 1.32 as shown in Figures 9.2 and 9.3. The optimized geometry has a FM of 0.792 and a power loading of 10.95 lb/hp.

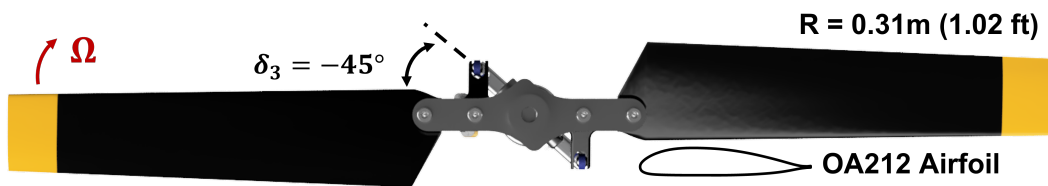
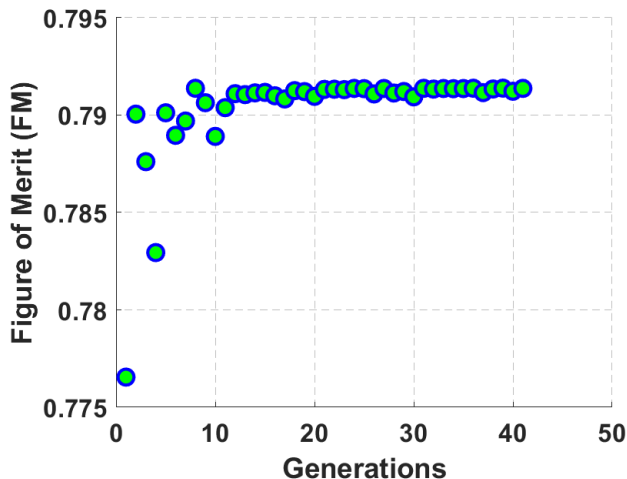
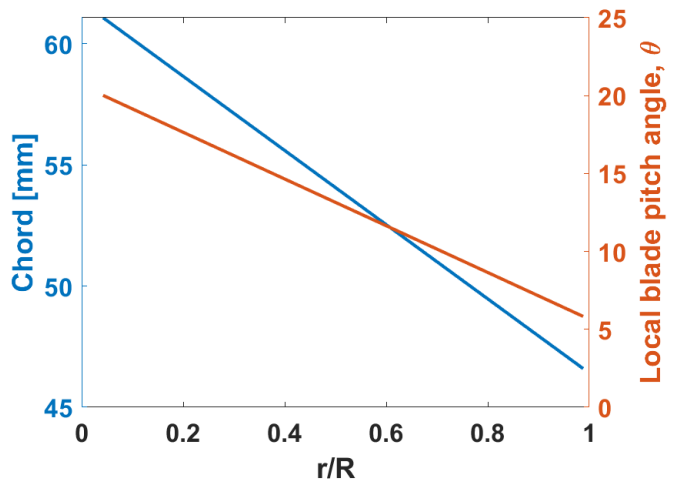


Figure 9.2: Tail rotor planform



(a) Tail rotor optimization



(b) Optimized tail rotor geometry

Figure 9.3: Tail rotor optimization

9.3 Tail Rotor Mounting

The main rotor shaft pre-tilt and engine placement required special attention to tail rotor mounting. A 0.12 m (0.39 ft) tip clearance is present between the main rotor and tail rotor at the lowest allowable main



Table 9.2: Tail Rotor Parameters

Parameter	Value
Diameter	0.63 m (2.07 ft)
Number of Blades	2
Solidity	0.1
Aspect Ratio	6.37
Moment Arm, l_t	2.02 m (6.6 ft)
Tip Velocity	182.9 m/s (600 ft/s)



Figure 9.4: Tail rotor vertical placement

rotor flapping angle (-12°) to ensure safety from blade strike. This clearance is higher in hover due to coning and the 6.5° fixed rotor shaft tilt. The main rotor to tail rotor moment arm is 2.02 m (6.63 ft). Two possible tail rotor mounting locations were considered for *Huma*, shown in Figure 9.4. Position 1 was chosen for *Huma* for three reasons: (1) The tail rotor has a significant 0.14 m (0.48 ft) ground clearance for safety when landing in the disaster environment, (2) The trim roll angle is decreased since the tail center of rotation is closer to the main rotor plane, which is beneficial for precise hover over the ship deck, (3) the tail rotor is placed at the center of the tail boom which offers greater structural stiffness and space for a gearbox. However, the tail rotor drive shaft is placed along the bottom of the tail boom for bearing support, as documented in Section 12.4. A belt drive system is required to increase the tail rotor height, however, this small added weight does not outweigh the safety and flight dynamics benefits of a raised tail rotor.

Huma's tail rotor is mounted to the left of the tail boom in a pusher configuration. The tail boom and vertical stabilizer blockage occur upstream of the tail rotor, where the rotor wake contraction is widest rather than downstream where the wake is contracted to a smaller diameter than the tail rotor. This decreases losses from flow blockage.

The tail rotor operates with a top-aft direction of rotation. This delays the onset of vortex ring state from leftward wind due to the influence of the main rotor wake [35]. Additionally, a side wind from the right causes the main rotor to generate vortices that reach the tail rotor in a forward-top orientation. The tail rotor benefits from an aft-top rotation to counter the main rotor vortex.

9.4 Hub Design

Huma has a two-bladed teetering rotor constructed using composite materials for the blade and aluminum 7075 for the yoke to minimize structural weight. The teetering design was selected due to its mechanical simplicity, high technology readiness level due to many helicopters currently operating with teetering tail rotors, and low weight. The tail rotor design is shown in Figure 9.5. It is inspired by the time-tested Robinson R22 teetering tail rotor hub [36]. The tail rotor blades include two radially-spaced spherical bearings at the root to attach in between the top and bottom hub yoke plates. Pitch horns are directly built into the composite blades to drive pitch articulation about the spherical bearings within a 22° pitch range. The pitch links attach to a collective-only rotating fixture actuated by the same type of electro-hydrostatic actuator that actuates the main rotor swashplate. A low-profile hub fairing is included to minimize tail rotor drag in forward flight. A mast retention bolt and a wedge-lock washer fasten the hub yoke to the tail rotor hub shaft, which has drive flats to ensure that the tail rotor is constrained to the shaft in rotation. A corrosion-resistant EPDM rubber mast bump stop fits within the hub yoke to prevent potential damage from mast bumping.



A $-45^\circ \delta_3$ angle is built into the teetering hub to introduce stabilizing pitch-flap coupling. As the blades flap up, pitch is decreased to return to a lower flap angle. This reduces maximum blade flapping angles to prevent mast bumping and blade-fuselage strikes [37]. Furthermore, pitch-flap coupling results in decreased blade and pitch link loads. The δ_3 reduces unaugmented directional static stability but this is mitigated with a directional stability augmentation system for *Huma*.

10 Airframe Design

10.1 Overview

Huma's internal structure and components were designed to withstand flight loads of $+3.5g/-1.0g$ [28]. The material selection of the vehicle was heavily influenced by the marine environment. Vehicle modularity between missions was also a major design consideration. The landing gear was designed for hard ship deck landings, while maintaining a low drag profile and weight. The vertical empennage was designed to function both as a stabilizer and landing gear.

10.2 Internal Layout

The internal layout of *Huma* is the result of interconnected decisions intended to develop an efficiently packed and carefully balanced aircraft with minimal empty space. The transmission and powertrain are arranged to allow for swashplate actuation, tail transmission structural support, and a low weight transmission design that forgoes traditionally heavy transmissions. The center body bay serves as a readily accessible mounting point for modular components, and its placement between the forward fuel tank and collector sump to allow for a continuous connected fuel line from the forward tank through the add-on tank to the collector tank. The placement of the avionics minimizes their impact on the aerodynamic fuselage while maximizing their field of view, enables air cooling from incoming airflow, and counterbalances the vehicle CG. Even the mounting and assembly of the components was carefully considered, with the placement of structural members driven by the positions of mission critical components and the need to maintain a low-drag fuselage shape.

The internal layout is detailed on the next page. The configuration displayed is the long endurance mission lift compound with wings and an auxiliary fuel tank. The supplies mission SMR configuration utilizes the same airframe and internal layout. The configuration differences occur entirely within the center body bay, as discussed in Section 4. The center of gravity of both configurations, fully loaded, varies slightly. The SMR configuration CG is 23 mm (0.91 in) longitudinally forward of the lift compounded configuration's CG, 8 mm (0.31 in) higher along the vertical axis, and 1 mm (0.04 in) further left in the lateral direction.

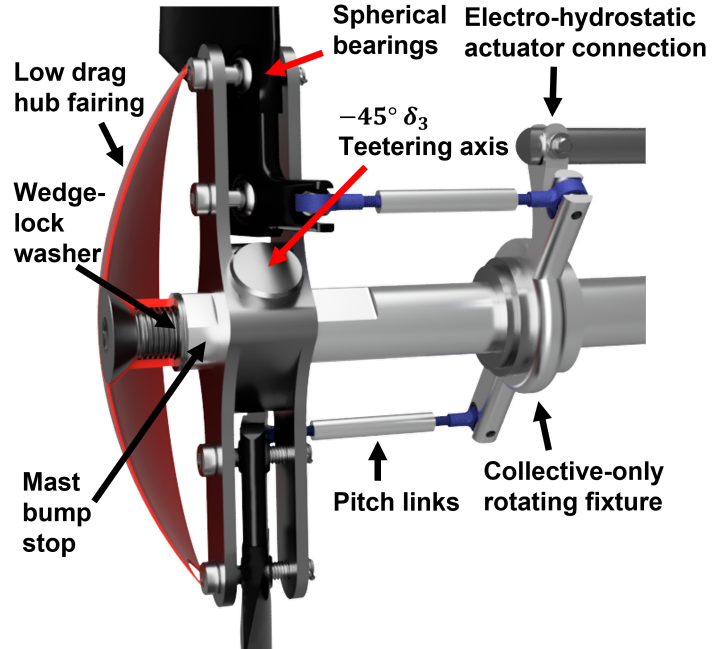
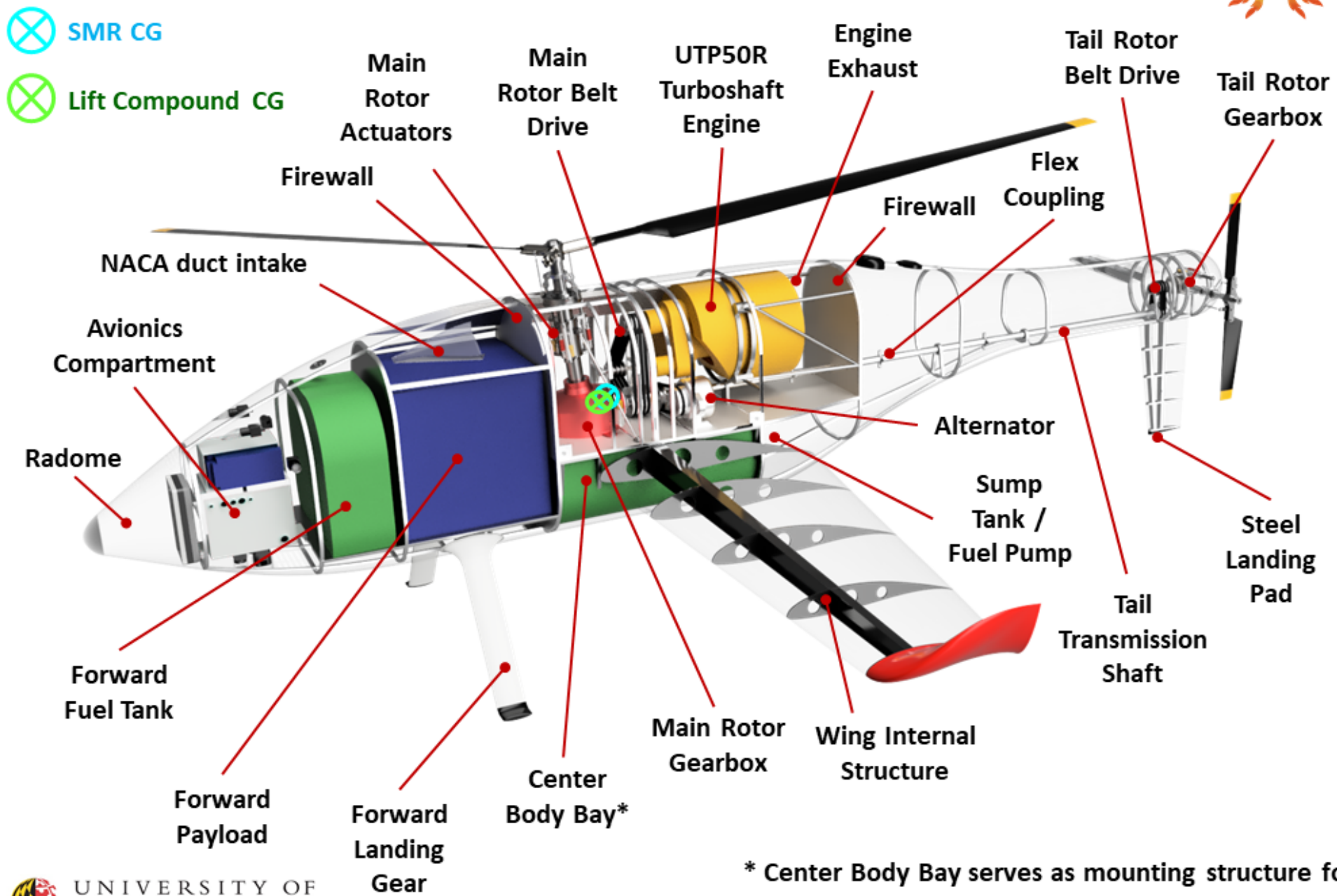


Figure 9.5: Tail rotor hub components



Thorough Internal Layout



10.3 Marinization

The aerosol of salt particulates in marine environments, or sea spray corrodes metallic materials by acting as a catalyst in the presence of atmospheric oxygen and moisture. This causes surface pitting, and requires consistent service or replacement of parts. Metals selected for *Huma* were resistant to corrosion from sea salt particulates such as Na^+ , Cl^- , K^+ , Mg^{+2} , Ca^{+2} , and SO_4^{2-} . The material rate of deterioration can be quantified by its corrosion rate, which is evaluated by Salt spray tests [38]. Table 10.1 shows the materials selected for *Huma*'s internal structure and their corrosion rates from [39]. A metal's rate of corrosion is determined by its alloying materials. Composite material selection is dictated by delamination due to UV radiation and hydrolysis rather than corrosion rate. Delamination is an interlaminar failure mode due to high stresses in dissimilar laminate plies. Composites such as carbon fiber polymers can also cause galvanic corrosion of aluminum metals due to their large electropotential difference in the presence of sea spray. These failure modes can be mitigated by the use of coatings, sealants, non-conductive layers, and drainage taps for water and moisture. *Huma* uses thin film Cerakote H-series paint as a coating to prevent corrosion of metal materials due to sea salt for up to 2000 hours. The paint also prevents hydrolysis and provides UV stability to composites like Kevlar. The wing box region also has a layer of fiberglass to prevent physical contact between the carbon fiber I-beam and aluminum fuselage frame. Drainage points are located in the lower section of the fuselage skin to prevent the collection of water and moisture.

Table 10.1: Material selection for structural components

Structural Component	Material	Corrosion Rate mm year ⁻¹ (Mils year ⁻¹)
Fuselage Structure	Aluminum-lithium 2099-T83 Alloy	0.06 (2.36)
Transmission Casing	Aluminum A380	0.15 (5.91)
Gears	ACUBE®100 Steel	0.077 (3.03)
Shafts	AISI 4340 Steel	0.077 (3.03)
Landing Gear	Aluminum 7075 Alloy	0.14 (5.51)
Lift Rods	Aluminum 7075 Alloy	0.14 (5.51)

10.4 Fuselage Structure

The airframe is a semi-monocoque structure, consisting of 15 bulkheads, interconnected by stringers and webs for load distribution as seen in Figure 10.1. Two keel beams run the length from the nose to the tail, with the notable exception of the center body bay for modular access. The bulkheads ahead of the rotor supports the radar housing in the nose cone, the avionics bay, fuel tank and payload systems. At the base of those bulkheads, the landing gear box is situated to allow for transfer of loads from the ground reaction to the rest of the vehicle. Several bulkheads are situated in the center of *Huma*. This is to distribute the load from several subsystems such as the engine and transmission housing, as well as the structure to absorb the main rotor hub loads and wing root bending moments. Bulkheads aft of the engine begin to shape into the tail boom, which is also a semi monocoque structure. Subsystems like the empennage and transmission gearbox in the tail boom are attached to the rear bulkheads. The factor of safety of the airframe in the SMR configuration and Lift Compound airframe are 1.97 and 1.65 respectively.

A detailed dynamic analysis was carried out to examine whether vibration absorbers are needed to actively suppress vibration. Because expected cruise advance ratios are low, the calculated vibrations were low and suppression devices were deemed unnecessary.



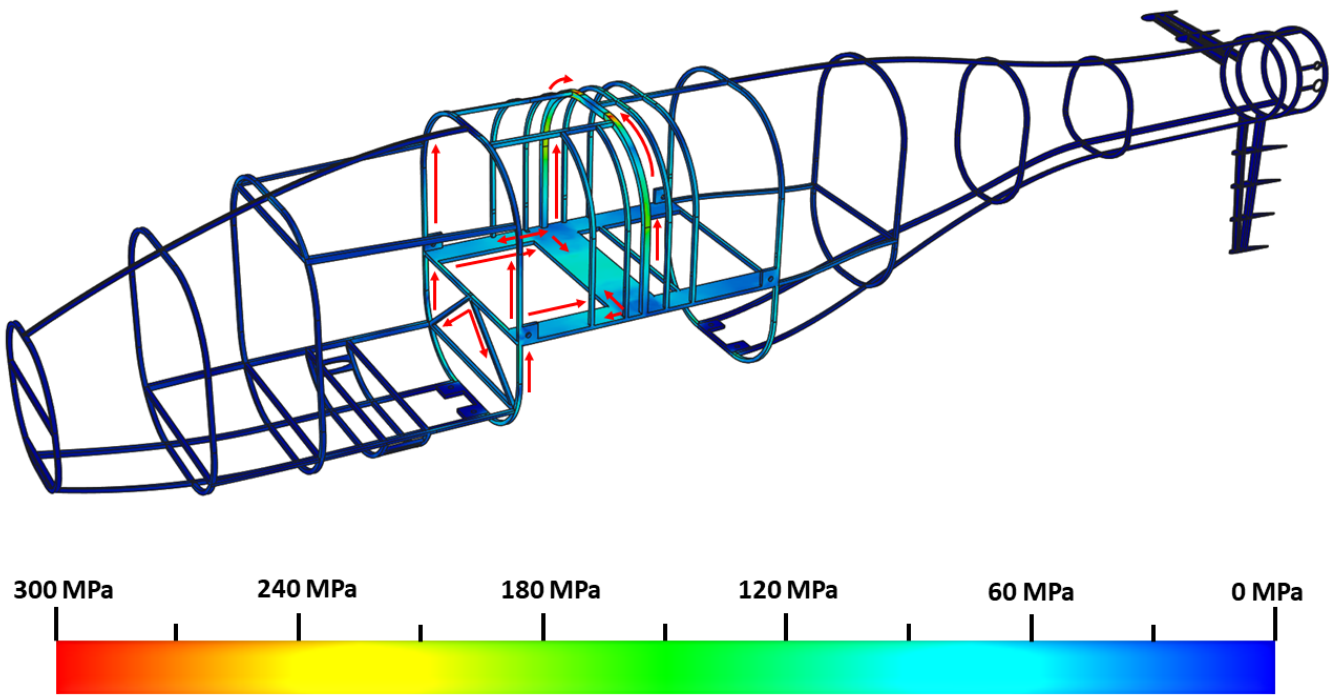


Figure 10.1: von-Mises stresses of airframe with load paths

10.4.1 Load Paths

Rotor loads are transmitted to the airframe through the lift rods connected to the main rotor shaft. The lift rods distribute the loads to the center of the airframe by means of the bulkheads ahead of the engine. The primary load paths are highlighted in Figure 10.1 with red arrows. These arrows represent the directions of diffusion of main rotor loads and wing loads into the cabin. Viscoelastic vibration dampers at the base of the lift rods minimize the oscillatory loads from the main rotor shaft. During landing and taking off, the ground reaction loads are transmitted through the landing gear box reinforced to the airframe at the front, and to the bulkheads in the tail boom at the rear. They have been sized to sustain 2.2g ground reaction loads. The addition of the wing in the long endurance mission will also provide additional loads passing through the center body bay to the center airframe.

10.4.2 Airframe Material Selection

Airframes are typically constructed with metals or composites. Composites were not selected due to their high cost of manufacturing. Aluminum alloys are often used due to their high specific stiffness and superior damage and buckling tolerance over other metals. Of these, aluminum-lithium alloys offer low density and high yield strength. A third generation Al-Li alloy, 2099-T83 has a much higher fracture toughness, low density, and improved corrosion resistances. [40].

10.5 Lift Rod Design

The lift rods serve the function of load transfer from the main rotor shaft to the bulkheads, bypassing the transmission housing. The lift rods are connected to the bulkheads by means of the shaft support collar on

the main rotor shaft. The rods which experience tension, were sized to handle rotor loads at the maximum loading condition of 3.5g with a factor of safety of 1.5. A hollow cross-section of inner and outer diameters 5.2 mm and 6.25 mm respectively, was selected over a solid rod to save weight without any effect in load bearing capabilities. Aluminum 7075 was chosen for its low weight, and high tensile yield strength.

10.6 Empennage Design

Huma's empennage system consists of a horizontal stabilizer bolted to the airframe on the starboard side of the vehicle and a vertical stabilizer on the bottom of the tail boom. Figure 10.2 shows the components of *Huma*'s empennage.

10.6.1 Horizontal Stabilizer

The main functions of the horizontal stabilizer are to counter the pitching moment produced by the fuselage during cruise and to provide longitudinal static stability. The NACA 4415 airfoil was selected for its high lift-to-drag ratio and low pitching moment. The initial planform area was sized using parametric analysis [9], resulting in an area of 0.14 m². This area was then refined through flight dynamics analysis to optimize the design for adequate static and dynamic stability, and finalized with a smaller tail area of 0.094 m² to avoid excessive weight and vertical gust susceptibility. Stabilizer structure consists of three components, namely the spar, ribs and skin. There are two C-spars located at 25% and 60% chord length are cantilevered to the airframe with bolts. C spars along with the skin form the torsion box for the stabilizer. This setup is designed to increase the torsional stiffness of the stabilizer, thereby preventing dynamic instabilities.

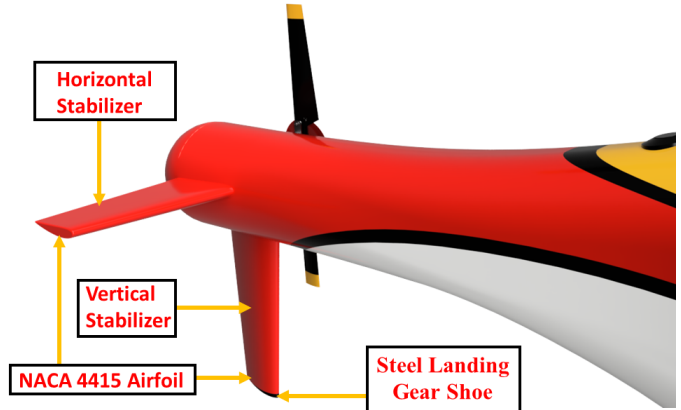


Figure 10.2: *Huma* empennage components

10.6.2 Vertical Stabilizer

The vertical stabilizer provides anti-torque in forward flight to offload the tail rotor and ensures directional stability. The vertical stabilizer is initially sized to fully offload the tail rotor during cruise. Similar to the horizontal stabilizer, the vertical tail area is iterated with flight dynamics analysis. This involves adjusting the size based on comprehensive aircraft trim analysis and the stability characteristics. The NACA 4415 airfoil was selected here as well due to its low pitching moment and high lift to drag ratio. The orientation and size of the vertical stabilizer depends on the loading conditions in flight and landing. A vertical stabilizer both above and below the tail boom would be slender, and fail in landing, so the current orientation of one stabilizer at the bottom of the tail boom was selected.

10.7 Landing Gear

The design process for *Huma*'s landing gear involved a trade study of the various configurations, material and cross section selection, followed by a static analysis under loading conditions with an emphasis on light weight structure selection.

10.7.1 Configuration Trade Study

Five landing gear configurations were considered. Each was studied using AFDD Weight model [9] and calculated flat plate area. The table 10.2 summarizes the results and the final selection:

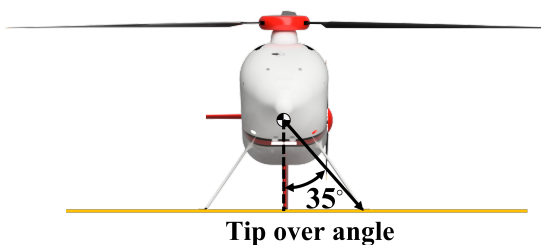
Table 10.2: Table summarizing the landing gear trade study

Landing Gear Configuration	Mass kg (lbs)	Flat Plate Area m ² (ft ²)
Retractable Skid	5.17 (11.4)	0
Retractable Wheel	12.17 (26.83)	0
Fixed Skid	4.32 (9.52)	0.05 (0.54)
Fixed Wheel	11.2 (24.69)	0.10 (1.08)
Three-point Landing Gear	2.4 (5.29)	0.004 (0.043)

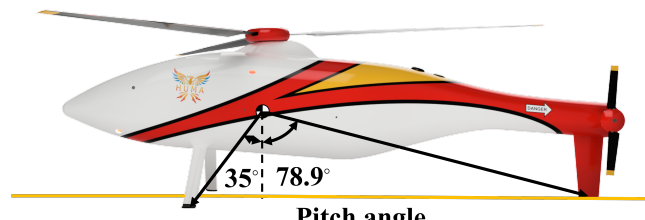
Both the retractable systems were too heavy. The fixed wheel system was both heavy as well as high drag. The three point landing gear system was the best of all. It was also expected to be more slip resistant on a wet deck.

10.7.2 Landing Gear Geometry

Landing gear design was driven by the stability of the vehicle during ground operations, and the loading conditions during landing. The pitch and roll stability angles were calculated for the *Huma*'s equilibrium position on the ground. The pitch stability and roll stability angles for *Huma*, are 78.9° and 35° respectively. Usually, the roll stability and pitch stability angle about the center of gravity should be less than 60 degrees and 30 degrees respectively due to static and dynamic rollover concerns. A larger margin was maintained to account for ship deck pitching and rolling motions. The selected three-point landing gear bypasses the 60° pitch stability limit since the tail is designed for landing loads. The height of the landing gear was sized such that sufficient ground clearance for the crew to remove the center body bay and swap the fuel tank and payload.



(a) Landing Gear Pitch Stability



(b) Landing Gear Roll Stability

Figure 10.3: Landing Gear Stability Angles

Ideally, the landing gear is designed such that the rotor hub plane is parallel to the ground plane at touchdown. However, for *Huma*, this led to long and slender front gear that would fail in compression. Therefore, the landing gear geometry was shortened. This requires a pivot motion about the tail landing gear during takeoff and landing. A steel pad is built into the bottom of the tail landing gear to prevent slipping and damage during takeoff and landing. For the final stability angles, the shaft is 4.5° ahead of the vertical plane in its equilibrium position.

Landing gear with rectangular cross sections carry stress concentration at its edges and require aero shells; making the landing gear heavy. Circular cross section landing gears also induce drag. Hence, both were rejected. The elliptical cross-section was selected as it is both light weight and produces less drag. The base of the front landing gear is made of rubber to prevent slippage on wet ship decks. This increase in friction, added with the friction from the steel shoe. The front landing gear foot is made of rubber to prevent slippage on wet ship decks. Calculations gave an outer elliptical semi major axis of 75mm and 7.6 mm with a 3 mm wall thickness.

From the Navy AR-56 structural design requirements [28], the limit sink speed of rotorcraft in marine environment is 8 ft/sec. Taking the vertical loading condition of 2.2g, the cross section dimensions were calculated for buckling and compressive stress.

Composites were rejected due to their brittle nature and low damage resistance. Aluminum 7075 alloy was selected due to its low density and high specific strength coupled with good corrosion resistance. Cerakote paint coating is used to provide additional protection from sea spray aerosol.

10.7.3 Landing Gear Static Structural Analysis

Analysis of the landing gear in loading conditions prescribed from Navy AR-56 using ANSYS as seen in Figure 10.4. The figure shows the effective stresses experienced by the landing gear during maximum loading conditions. The front landing gear is rigidly connected to the fuselage by a root insert. The factor of safety of was found to be 1.71.

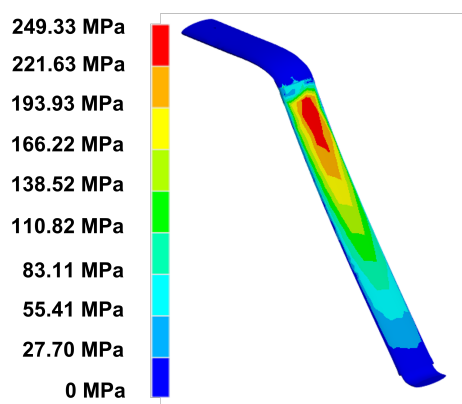


Figure 10.4: von-Mises stress analysis of landing gear

11 Powerplant

When selecting a powerplant for *Huma*, the RFP-specified 160 kg (353 lbs) MGTOW limited much of the design space of conventional powerplants. Options were further limited by the additional requirement that the aircraft must use Jet-A fuel, or run on purely electric power. Because the goal of this design is to extend loiter duration time to 10 hours or more and maximize the payload capacity, a lightweight powerplant with high specific power and low specific fuel consumption (SFC) is paramount.

Sizing indicated a maximum power requirement of 27 kW (36 hp), which may be achieved by a single engine, or a collection of engines. Powerplants were investigated that are currently on the market or achievable today, as it is our goal to deliver a vehicle with a high degree of technological readiness.

11.1 Powerplant Selection

Four types of powerplants were investigated: 1) turboshaft, 2) piston, 3) engine-generator and turbogenerator with electric motors, and 4) hydrogen fuel cells with electric motors.

11.1.1 Turboshaft

Figure 11.1 shows the candidate turboshaft engines for *Huma*. Given the low weight class of the aircraft, the JetCat helicopter turbine engines, mostly intended for small-scale hobby use, were investigated. *Huma* would require several of these smaller-scale engines, such as the JetCat SPT10-RX-H. However, despite



their high specific power, the high specific fuel consumption of these smaller engines made them undesirable. The Stuttgart Engineering STV 100 and STV 130 have good specific powers but possess a high SFC, and require presently untested modifications to operate using Jet A fuel. Turboshaft engines that operate at powers substantially lower than their rated power suffer performance losses that decrease SFC. The Turbotech TP-R90 is another option; a recuperating engine that utilizes the hot engine exhaust to preheat its fuel prior to combustion, considerably improving engine SFC. The total weight of the engine, however, outweighs the advantage of its low fuel consumption. UAV Turbines UTP50R [41] has an acceptable specific power, and also utilizes recuperation to reduce its fuel consumption. With an installed power close to *Huma*'s power requirement, losses in efficiency do not significantly diminish the utility of the engine. These properties make the UTP50R an ideal candidate as the powerplant for *Huma*. The properties of these turboshaft engines are summarized in Table 11.2.

Table 11.1: Summary of candidate engine characteristics

Engine	Power Output kW (hp)	Weight kg (lbs)	Power/Weight Ratio kW/kg (hp/lb)	SFC kg/kW-hr (lb/hp-hr)
SPT10-RX-H	9.0 (12.1)	2.89 (6.37)	3.11 (1.9)	1.87 (3.07)
STV 100	74.6 (100)	28.0 (61.7)	2.66 (1.62)	0.36 (0.59)
TP-R90	96.9 (130)	80.0 (176.4)	1.21 (0.74)	0.17 (0.28)
UTP50R	37.3 (50)	31.8 (70.0)	1.17 (0.71)	0.27 (0.45)



Figure 11.1: Candidate turboshaft engines

11.1.2 Piston Engine

Piston engines are much heavier but consume less fuel. For loiter missions, it is important to study this trade-off. The candidate heavy-fuel piston engines are shown in Figure 11.2. The Hirth Engines 3503 HF 2-stroke [42] appeared to be a reasonable choice for *Huma* with a specific power that exceeds the UTP50R, but this benefit is offset by the weight of a liquid cooling infrastructure and a higher SFC. The Hirth 4201 HF [43] is an air-cooled engine with an 11 kW (15 hp) power output, but ultimately was not selected due to its low power-to-weight ratio, and poor SFC. The ZOCHE aero-diesel ZO 03A [44] may offer an exceptional SFC, but weight savings due to its low fuel consumption are offset by its high weight. The LiquidPiston XTS-210 [45] rotary engine uses a unique combustion system, however, it fails to outperform any of the turboshaft engines in specific power or specific fuel consumption. Piston engines capable of fitting within *Huma*'s weight class prove to display low specific power compared to competing turboshaft engines and often require additional heavyweight infrastructure for cooling, making them poorly suited for this lightweight UAV.

Table 11.2: Summary of candidate engine characteristics

Engine	Power Output kW (hp)	Weight kg (lbs)	Power/Weight Ratio kW/kg (hp/lb)	SFC kg/kW-hr (lb/hp-hr)
3503 HF	44.0 (59.0)	36 (79.3)	1.22 (0.74)	0.44 (0.73)
4201 HF	11.0 (14.75)	11.5 (25.4)	0.95 (0.58)	0.49 (0.80)
ZO 03A	51.0 (68.4)	5 (121.3)	0.93 (0.56)	0.22 (0.36)
XTS-210	19.3 (25.9)	21.2 (46.7)	0.91 (0.55)	0.35 (0.58)

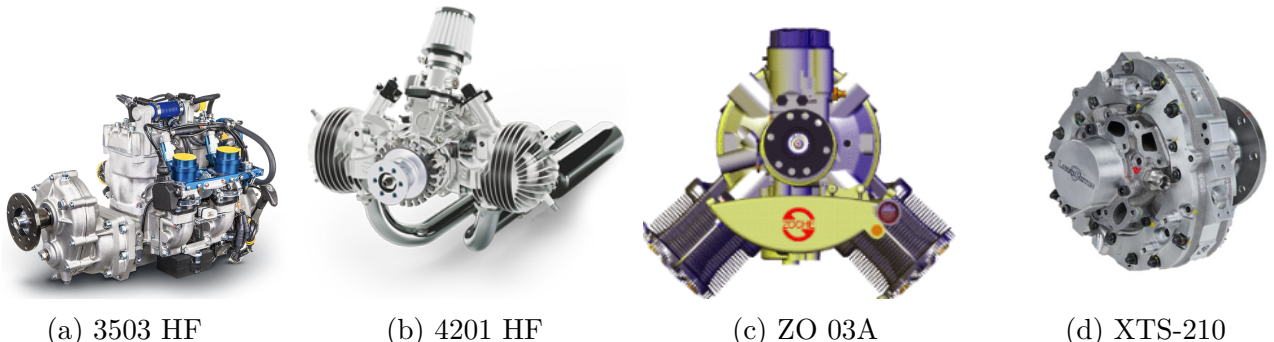


Figure 11.2: Candidate piston engines

11.1.3 Engine-Generator and Turbogenerator

An engine-generator with distributed propulsion using electric motors is an attractive system to reduce transmission weight. This methodology would require an engine-generator hybrid powerplant attached to electric motors. One such turbogenerator, the TG-R55, offers an attractive SFC but is too heavy for feasible use. The LaunchPoint HPS400 [46] suffers from the same drawback. Though this powerplant is self-starting and includes a cooling system for hover and low-speed applications, its low specific power makes it unusable. The FusionFlight ARC Micro Turbo Generator [47] is a much smaller scale powerplant intended as a personal portable power source. When compared to larger powerplants in the 50-100 hp class, its low power-to-weight ratio makes it suboptimal for aerospace applications. In addition to these generators, one must also consider the weight of the electric motors. A weight equation (Equation 3) based on statistical data of 51 commercially available electric motors [48] was used to estimate weights of motors needed for *Huma*'s main and tail rotors.

$$\begin{aligned} W \text{ in kg} &= 0.2519Q^{0.5857}, Q \leq 13 \text{ Nm} \\ W \text{ in kg} &= 0.1062Q^{1.0422}, Q > 13 \text{ Nm} \end{aligned} \quad (3)$$

The necessary electric motors would weigh 29 kg (63 lbs), nearly the weight of the UTP50R turboshaft. Additionally, the electric motor driving the main rotor would likely need liquid cooling components, adding more weight. Utilizing a generator and distributed electric motors would eclipse the weight savings of a simplified transmission, so this method of power generation was not pursued.

Table 11.3: Summary of candidate generator characteristics

Engine	Power Output kW (hp)	Weight kg (lbs)	Power/Weight Ratio kW/kg (hp/lb)	SFC kg/kW-hr (lb/hp-hr)
TG-R55	55 (73.8)	55 (121.3)	1.0 (0.61)	0.29 (0.48)
HPS400	40 (53.6)	59 (130)	0.68 (0.41)	0.55 (0.91)
ARC Micro	8.0 (10.7)	10 (22)	0.8 (0.49)	2.25 (3.7)
NOVA-2400	2.4 (3.22)	4.2 (9.26)	0.57 (0.35)	0.83 (1.36)

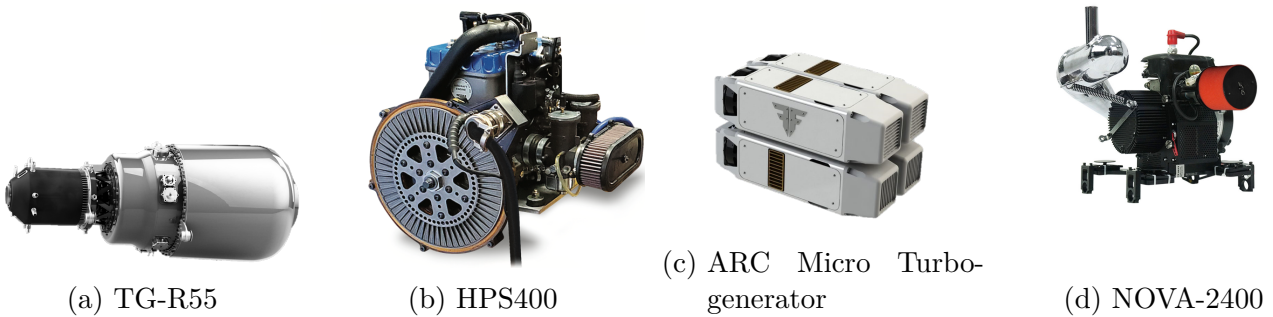


Figure 11.3: Candidate engine generators and turbogenerators

11.1.4 Hydrogen Fuel Cell

It is worthwhile to examine the possibility of utilizing a clean and renewable power source such as hydrogen fuel cells instead of fossil fuel. Hydrogen fuel does not produce hazardous exhaust and generates energy at lower and safer temperatures. Proton exchange membrane (PEM) fuel cells [49] have high specific energy, 39.4 kW-hr/kg (26.4 hp-hr/lb), far exceeding Li-ion batteries. However, the power-to-weight ratio of hydrogen fuel cells, including balance of plant, is approximately 0.5 kW/kg (0.61 hp/lb), which is far lower than the specific power of any of the turboshaft engines. A hydrogen-powered vehicle would require the PEM cells and an additional 29 kg (63 lbs) of electric motors. Another concern of hydrogen power is fuel storage. Liquid hydrogen must be maintained at -260° C (-425° F), requiring heavy tanks with thick insulation. Active heat rejection infrastructure would be highly integrated into the vehicle, making aircraft modularity far more challenging to achieve. If the hydrogen is stored in a gaseous form, the tanks are highly pressurized, and even composite tanks can at the most reach a hydrogen storage weight fraction of only 6 percent [50]. This means 6 kg (13 lb) of stored hydrogen would require a 100 kg (220 lb) tank. For the loiter segment of the long endurance mission alone, the tanks would need to weigh more than 30 kg (61.2 lbs), exceeding the maximum modular component weight defined by the RFP.

11.2 Powerplant Performance

Comparing all of the options discussed thus far, the UTP50R was selected for its low weight, installational simplicity, power output relative to the aircraft's needs, and low SFC during operation. Statistical data from a selection of turboshaft engines is used to develop an expression for the variation in engine SFC based on the power requirements of the vehicle at various stages of the mission [51]. This data was used to generate Figure 11.4, and used to calculate the UTP50R's performance over the entire mission, as discussed in Section 16.

During cruise sections of the mission, the Engine RPM is reduced by 15%. Though a significant reduction of engine RPM is known to have a detrimental effect on engine performance, NASA experimental testing predicts a 15% reduction in rotor speed is possible without a loss of turboshaft engine efficiency [52].

11.3 Powerplant Installation and Operation

The UTP50R engine is mounted on a supporting frame which is installed directly into the bulkheads of the fuselage structure. This ensures sufficient clearance between the engine and the tail rotor driveshaft which runs directly below the engine. Vibrations produced by the engine during operation are damped by viscoelastic polymer anti-vibration pads [53] located between the engine mounting ring and support struts. The output shaft of the UTP50R spins at 106,000 RPM [41], which necessitates the use of the manufacturer-provided gearbox, reducing the shaft RPM to 6000. The engine is delivered with a built-in starter/generator, fuel pump, and oil pump, which facilitates a compact installation with few additional components required for operation. The starter/generator acts as a backup alternator in case of main alternator failure.

The engine draws fuel from the collector sump tank located beneath the 0.4 mm (0.016 in) thick corrosion-resistant titanium firewall. The firewall surrounds the engine and transmission section to prevent any hazardous gases or flames from traversing to other vehicle areas. The thickness was selected to comply with FAR 23.1191 [54] without the need for experimental testing. The engine intake is connected to inlets set in the fuselage skin, forward of the main rotor pylon. Air passes through NACA ducts into two aluminum intake channels that attach directly to the intake mounts on the UTP50R. Engine exhaust is channeled out of a vent with guide vanes located aft of the rotor on the right side of the vehicle. The exhaust vent is vertically offset from the horizontal stabilizer to minimize thermal impact on the stabilizer's composite skin. It is low-profile to reduce drag in flight and is separated from the fuselage skin by a silicate fiber layer to prevent composite delamination. Warning labels are displayed near the vent to ensure the safety of ground personnel.

11.4 Fuel System

As a modular aircraft, *Huma* carries two internal fuel tanks; one permanently installed forward tank located ahead of a wall separating it from the front payload bay, and a modular auxiliary fuel tank, mounted in the center body bay. The forward fuel tank has a maximum capacity 18.7 L (4.94 gal) of Jet A fuel, carrying 12.6 kg (27.8 lbs) of fuel for the supplies-delivery mission, and 15 kg (33 lbs) for the long-endurance mission. The removable fuel tank, with a maximum capacity of 35.4 L (9.35 gal) carries 28.5 kg of Jet A for the long-endurance mission only. Both fuel tanks are constructed with an aluminum and fiberglass composite shell with a crashworthy rubber bladder interior. Based on data concerning the empty mass-to-volume ratio of the auxiliary fuel tanks of the R66 [55], the forward and add-on tanks are assumed to have an empty mass of 1.7 kg (3.75 lbs) and 3.22 kg (7.10 lbs), respectively (with additional support structure to mount the tank to the center body bay). Both tanks are gravity fueled; the forward tank by a port on the top of the fuselage and the add-on tank by a port on the side of the tank body.

Both tanks are pumped into a collector sump tank by a Currawong Engineering single-piston pump that

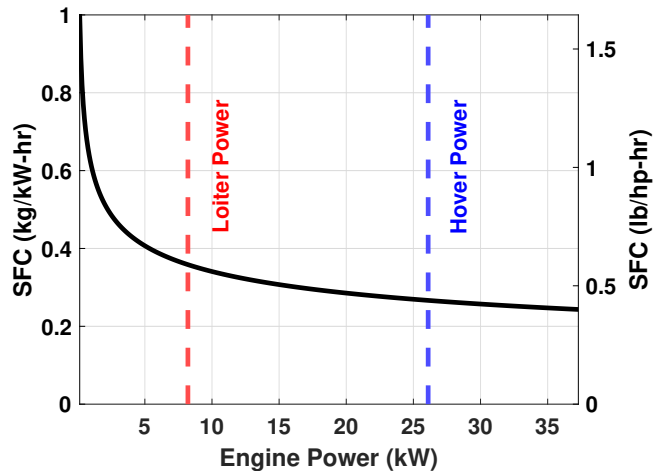


Figure 11.4: Engine SFC vs. Engine Operating Power



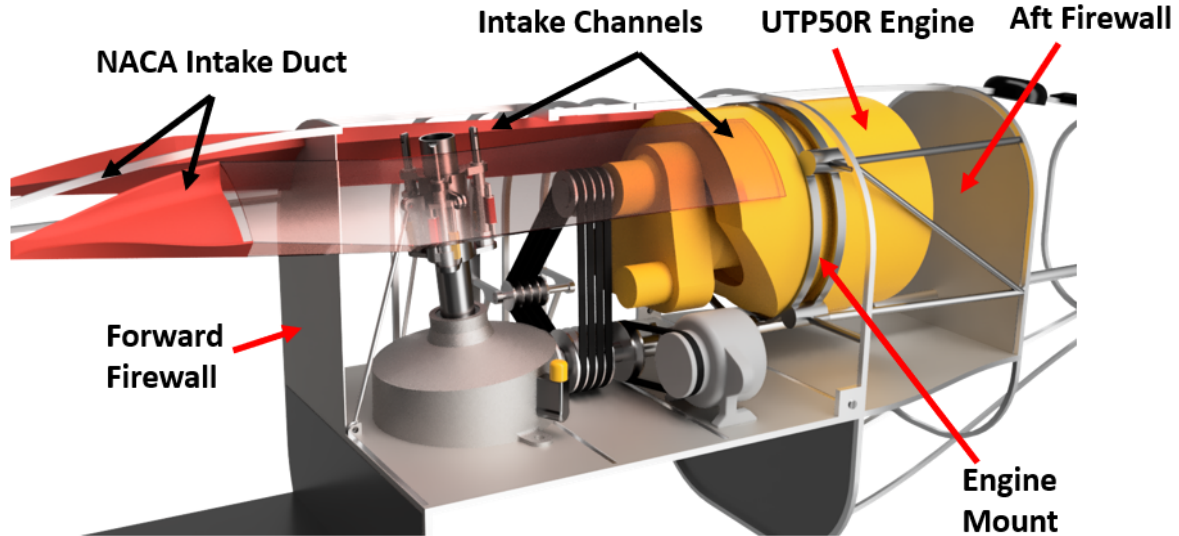


Figure 11.5: UTP50R installation with mount and intake manifold

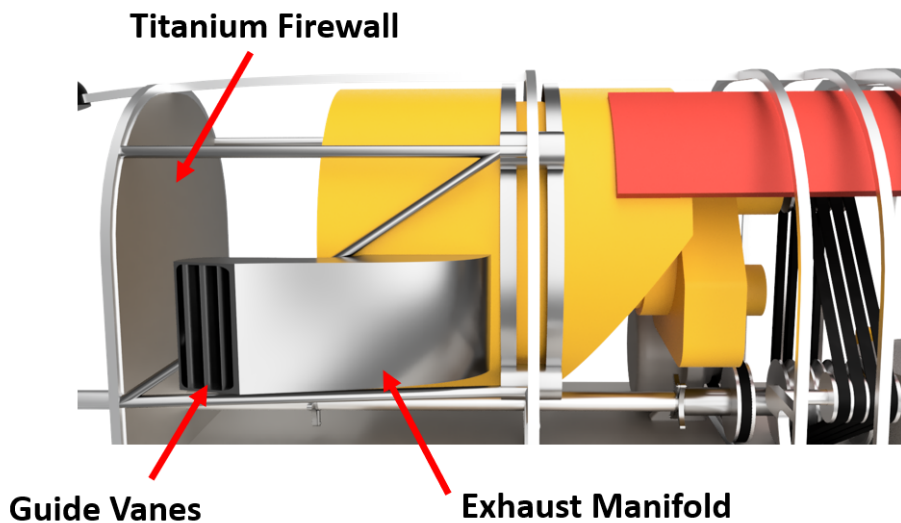


Figure 11.6: Huma exhaust manifold

keeps the sump tank full during operation with a flow rate of 260 g/min (0.002 lb/min) [56]. The add-on tank utilizes quick-disconnect fuel ports to ensure that personnel can quickly and effortlessly attach the tank and corresponding fuel lines to the overarching fuel architecture. The sump tank is located aft of the center body bay and directly below the main engine, and is sized to be compliant with FAA regulations [57], with a capacity of 0.38 L (0.10 gal). During the long-endurance mission, to ensure proper balancing of the aircraft center of gravity, the auxiliary fuel tank shall be depleted first. Float sensors will be used in each tank to monitor the fuel levels. When sensors indicate that the add-on fuel has been expended, the flight computer will close off the line to the add-on tank and the pump will begin to draw fuel from the forward tank.

12 Transmission Design

Power must be transferred from the UTP50R to the main rotor, tail rotor, and alternator by utilizing a drivetrain system that runs throughout the aircraft interior. The transmission was designed to utilize lightweight components as to minimize the *Huma*'s empty weight fraction.

12.1 System Overview

Huma's transmission uses a combination of cogged V-belts to turn a primary drive shaft, reducing the rotational speed from approximately 628 rad/s (6000 RPM) at maximum engine speed to 439 rad/s (4196 RPM). This drive shaft connects to both the tail transmission, main gearbox, and alternator pulley. The main gearbox reduces this speed further down to 111 rad/s (1058 RPM), while a series of pulleys and a tail gearbox step up this rotational speed to 579 rad/s (5530 RPM). A pulley on the central drive shaft reduces the rotational speed to 419 rad/s (4000 RPM) to deliver power to the alternator. Figure 12.1 details how these components are arranged within the airframe.

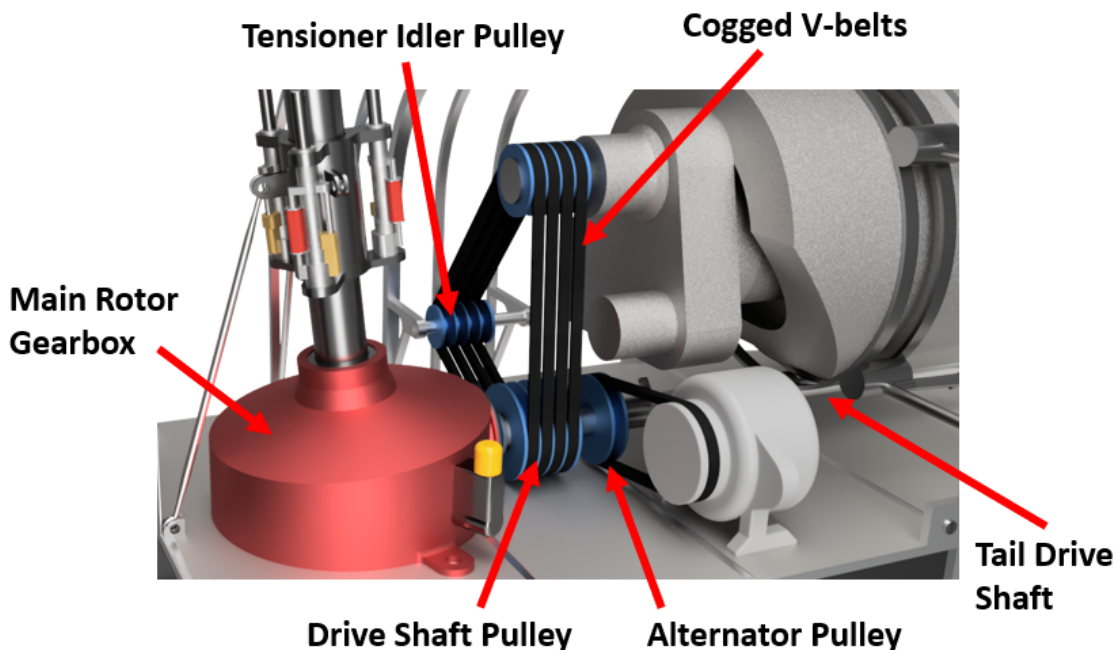


Figure 12.1: Layout of the main transmission

The transmission system transmits power between shafts at differing heights by utilizing cogged V-belts and pulleys. This allows the transmission to make better use of vertical space within the fuselage to position components. Belt and pulley assemblies require less weight than more traditional gearboxes which require housing or additional stages, and can be easily replaced and maintained. Bevel gears are used to achieve a change in shaft angle needed to position the main and tail rotors.

The main rotor and tail rotor transmissions are connected by way of a drive shaft with two stages: an AISI 4340 steel section that carries the torque and bending loads created by the main pulley assembly and transmits torque to the main rotor, and an aluminum 7075 section that transmits power to the tail rotor. This shaft is positioned underneath the UTP50R engine, includes flex couplings, and is supported by bearings and A-frame structures placed at the bulkheads aft of the steel section.

12.2 Drivebelt Design

Maintaining *Huma*'s compact and streamlined fuselage requires a novel and compact powertrain design that efficiently occupies space within the airframe while providing sufficient support for its components. Transmission for the tail rotor would need to route above or below the UTP50R engine, running on top of the empennage or along its bottom. Positioning the shaft at the top of the empennage would leave little room for swashplate actuation, so the shaft was routed beneath the engine, along the lower engine firewall and the base of the tail to achieve sufficient clearance to the engine and to provide A-frame support for the shaft bearings. The offset between the output shaft of the UTP50R and the tail drive shaft is 0.21 m (0.69 ft) vertically. Connecting these with a gearbox would require a significant weight penalty due to the gears themselves and the exterior housing. Similarly, the vertical position of the tail driveshaft needed to be raised to ensure adequate clearance between the ground and the tail rotor blades. A large multi-stage gearbox located in the tail would have a highly detrimental impact on the CG of the aircraft, which further necessitated the need for a lightweight solution to alter the location of transmitted power vertically.

Seeking a simpler, lightweight alternative to a tall gearbox, the team investigated V-belt and pulley transmissions based on data provided by Optibelt, a belt manufacturer headquartered in Germany that develops belt and pulley drives for automotive and industrial use [58]. Optibelt V-belts claim an efficiency of 97% when operating within the manufacturer-specified envelope of design power and RPM, and when operating on pulleys that exceed the designated minimum pulley diameter. Under these operating conditions, an Optibelt V-belt has a service life of 25,000 hours. Based on the manufacturer recommendation and the operating manual, the ZX/X10 belt was selected for the tail transmission, and the XPZ was selected for the main transmission.

These belts support a range of drive ratios up to 1:12, enabling the belt-driven stage of the transmission to accomplish a fraction of the total reduction needed for the main rotor. This ensures that only a small and efficient one-stage bevel gearbox will be necessary to step down the RPM of the main rotor shaft rather than a complex and heavy multi-stage reduction. These polychloroprene rubber and chloroprene compound belts are also corrosion resistant, making them suitable for storage and operation on a ship.

12.3 Main Rotor Transmission

The main rotor transmission includes the gearbox, drive belts, and a shaft.

12.3.1 Main Rotor Gearbox

The main rotor transmission consists of four XPZ wedge belts that turn the primary drive shaft, connected to a single-stage bevel gearbox that transmits torque to the main rotor shaft. The design of the bevel gears was informed by Dudley's Handbook of Practical Gear Design and Manufacture [59], Shigley's Mechanical Engineering Design [60], and American Gear Manufacturer's Association (AGMA) guidelines [61]. Sizing these gears was accomplished by studying the bending and contact stresses developed in the gears during operation. The bevel gears were designed to a minimum factor of safety of 1.5 against both stresses caused by radial loads and destructive pitting of the gears. Table 12.1 displays the calculation of the main gearbox gear and pinion factor of safety against wear and bending. Selecting a number of teeth for the gear and pinion that do not share a common denominator other than one ensures that the gears run with a hunting ratio. This ensures equal wear across all gear teeth and improves the operating life of the gears.

The main gearbox is a single-stage bevel gearbox with a reduction of 1:3.96, and a 96.5° change in angle from the input shaft to the output shaft. According to Dudley's Handbook, straight bevel gears operating within this reduction ratio have an efficiency of 98%. It consists of two bevel gears made of ACUBE 100, a cobalt-based alloy that displays high strength, corrosion resistance, and wear resistance, making it ideal



Table 12.1: Design parameters for main gearbox bevel gears

Quantity	Gear	Pinion
Number of teeth	63	16
Diametral pitch (P_d)	3.15 teeth/cm (8 teeth/inch)	3.15 teeth/cm (8 teeth/inch)
Face width (F)	1.8 cm (0.71 in)	1.8 cm (0.71 in)
Pressure Angle	20°	20°
Input Torque (T)	52.61 N m (38.8 ft lb)	52.61 N m (38.80 ft lb)
Quality Number	12	12
Contact Geometry Factor (I)	0.087	0.087
Geometry Factor (J)	0.17	0.26
Load-distribution factor (K_m)	1.0	1.0
Size factor for pitting resistance (C_s)	0.526	0.526
Size factor for bending (K_s)	0.593	0.593
Crowning factor for pitting (C_{xc})	1.5	1.5
Stress cycle factor for pitting resistance (C_L)	1.0	1.32
Stress cycle factor for bending strength (K_L)	0.862	1.0
Allowable contact stress number (S_c)	1.08 GPa (156 ksi)	1.08 GPa (156 ksi)
Allowable bending stress number (S_t)	0.132 GPa (19 ksi)	0.132 GPa (19 ksi)
Maximum contact stress (σ_c)	1.08 GPa (156 ksi)	1.42 GPa (206 ksi)
Maximum bending stress (σ_b)	0.11 GPa (17 ksi)	0.132 GPa (19 ksi)
Wear Factor of Safety (S_H)	1.65	2.17
Bending Factor of Safety (S_F)	1.5	1.59
Weight	1.46 kg (3.22 lb)	0.29 kg (0.34 lb)

for applications as a gear or bushing [62]. The housing of the gearbox will be manufactured with die cast Aluminum A380, selected for its strong corrosion resistance and ease of manufacturing. The selection of aluminum over magnesium alloys due to its corrosion resistance to seawater [63]. The interior of the gearbox is displayed in Figure 12.2. The hollow cavity in the base of the gearbox serves as a reservoir for oil that feeds into an oil pump mounted to the side of the housing. Oil jets spray into the intersection of the gear and pinion teeth to lubricate them, and oil collects in the sloped region below the pinion. A chip detector is placed in the reservoir to alert operators of any failure or wear in the gears.

The main gear is retained in the radial direction by a series of keys along the central collar of the gear, and axially by a pair of roller bearings placed along the main rotor shaft. The main drive shaft is inserted into the pinion gear, and a retaining bolt running from the pinion through a connection in the center of the main drive shaft secures the pinion radially. Axially, the pinion is retained by two roller bearings.

12.3.2 Drive Belts and Shafts

The main constraint when sizing the diameters of the primary driver pulleys is the space available in the fuselage interior. Since the main gearbox and drive shaft are mounted near the firewall, the maximum reduction possible was driven by the minimum pulley diameter of the XPZ belt, and the maximum driver pulley diameter given the geometric constraints of the fuselage. The primary drive belts that transmit power to the main drive shaft require tension to keep the assembly aligned and running efficiently. An idler pulley mounted on bulkheads to the right of the pulleys tensions the primary drive belts. The shaft of this idler pulley sits on an adjustable track that allows a mechanic to tighten or loosen the belts for operation or maintenance. Optibelt manufacturers provide data concerning the dynamic and static shaft tensions due to belt operation, and this belt data is summarized for the primary drive belts in Table 12.2.



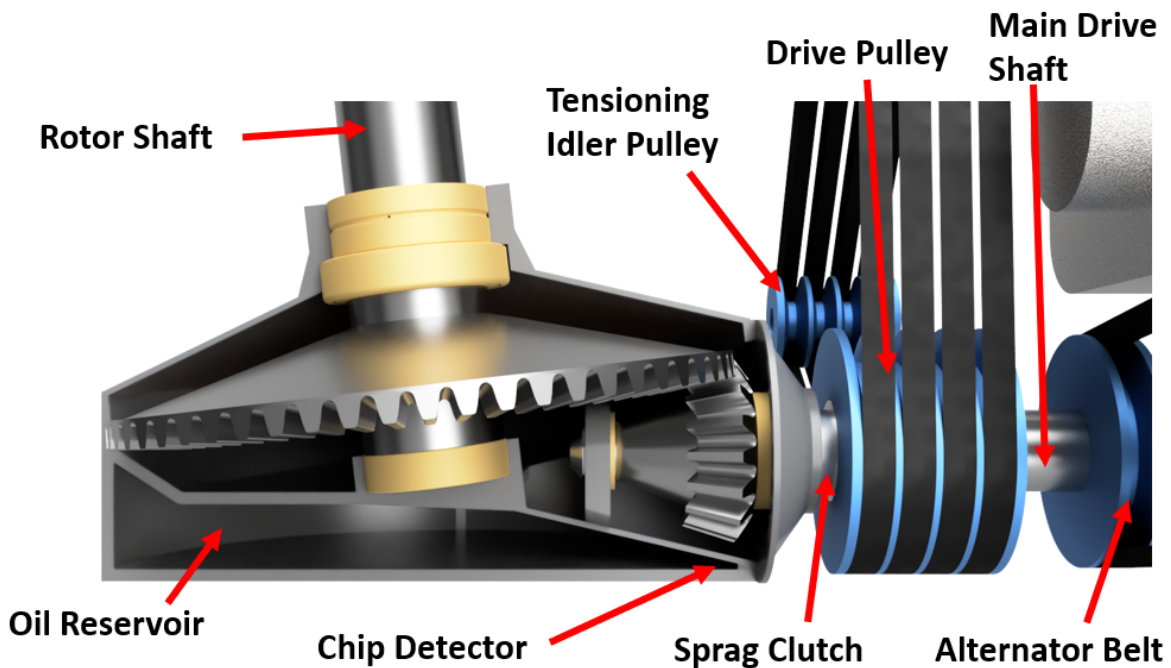


Figure 12.2: Interior of the main gearbox

Table 12.2: Summary of primary belt and pulley data

Parameter	Driven Pulley	Driver Pulley
Rotational speed, full rotor speed	4195 RPM	6000 RPM
Pulley diameter	80 mm (3.15 in)	56 mm (2.2 in)
Static shaft tension	411 N	411
Dynamic shaft tension	2957 N	2957 N

These tensions were used to size the main drive shaft, which connects to the aluminum tail transmission shaft with a flex coupling positioned behind the alternator driver pulley. The hollow main drive shaft is constructed out of AISI 4340 steel for its exceptional strength properties and is sized to a safety factor of 2 under the torque and tension loads of the driver pulleys. This drive shaft has an external diameter of 26.8 mm (1.06 in) and an internal diameter of 24.1mm (0.95 in). Interfacing between the driven pulley and the main drive shaft is a sprag clutch that allows for a rapid decoupling of the entire drive system from the powerplant in the event of an engine failure.

12.4 Tail Rotor Transmission

Figure 12.3 shows the complete tail rotor transmission assembly. The tail rotor transmission design was limited by geometric constraints imposed by the vertical position of the tail rotor and heavily influenced by the consideration of the aircraft center of gravity. Without a multi-stage gearbox or belt-driven transmission to raise the tail rotor axis, the clearance between the ground and the tail rotor would be only 0.06 m (0.20 ft). To achieve the safety and flight dynamics benefits of a raised tail rotor without inserting heavy components into the empennage that would significantly bring the vehicle CG aft. This vertical change in distance is accomplished with a pair of Optibelt ZX/X10 belts, while the 90°change in shaft direction from the drive shaft to the tail rotor is accomplished with a lightweight single-stage bevel gearbox.

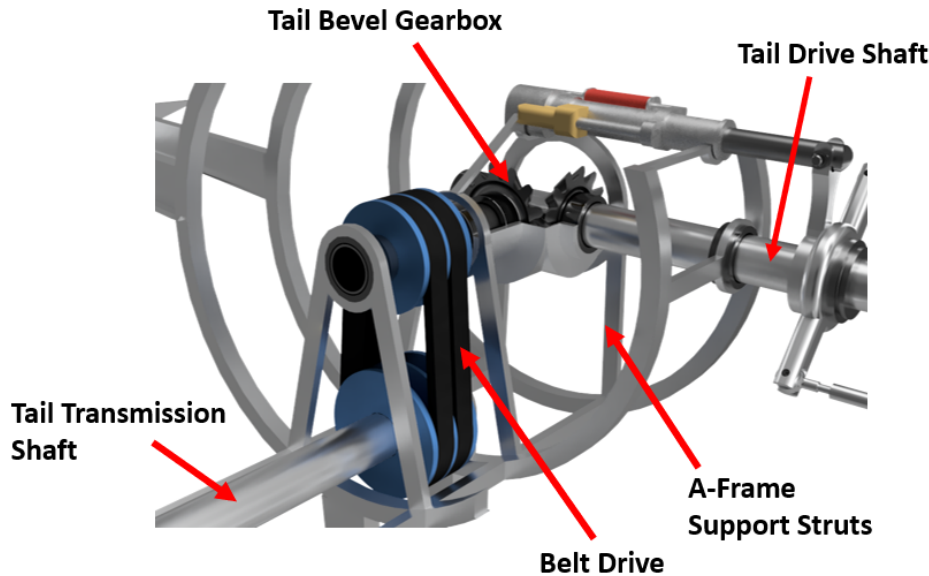


Figure 12.3: Tail transmission assembly

12.4.1 Tail Rotor Gearbox

The tail gearbox consists of two ACUBE 100 steel straight bevel gears positioned at a 90° angle. The gearbox has a reduction of 1.08:1, operating with an approximate transmission efficiency of 98% [64]. The tail bevel gear system uses the minimum number of teeth recommended by AGMA standards to limit weight while achieving a hunting ratio for low gear wear. The gearbox housing, input shaft, and tail drive shaft are suspended by A-frames built into the fuselage bulkheads. The housing is die cast from Aluminum A380, and the shape of the gearbox allows for oil to collect beneath the gear and pinion during operation, ensuring that both gears are splash lubricated during operation. The gear is retained axially using a roller bearing and the stepped end of the input shaft, while keys inserted between the shaft and gear retain the gear radially. The pinion is similarly retained radially by keyways between the shaft and pinion and retained axially by a pair of roller bearings mounted to the gearbox housing. The bending and wear factors of safety of the tail rotor gears is explored in Table 12.3.

12.4.2 Drive Belts and Shafts

The bevel gearbox reduction was designed as small as possible to minimize tail transmission weight. The drive belts are responsible for the majority of the reduction occurring between the tail drive shaft and tail transmission shaft. The pulley assembly achieves a reduction of 1.22:1, utilizing pulleys above the minimum pulley diameter for the ZX/X10 belt to maintain Optibelt's advertised efficiency and 25,000 hour operation life. Additional design data concerning the pulleys is discussed in Table 12.4. The input shaft of the gearbox and tail transmission shaft were both sized according to the torque loads transmitted to the tail and the bending moment caused by tail transmission drive belt tension. The tail transmission drive shaft carries a low fraction of the power carried by the main drive shaft and spans the entire length of the empennage, so Aluminum 6061 was selected for its low density, low cost, and capability of withstanding fatigue loads. Flex couplings are installed along the shaft at the midpoint between the empennage bulkheads to reduce bending loads in the shaft with fuselage deformation.

One of the major concerns of operating a tail rotor with a long transmission shaft is staying below the critical speed during operation. A long unsupported tail rotor shaft risks crossing the critical shaft RPM

Table 12.3: Design parameters for tail gearbox bevel gears

Quantity	Gear	Pinion
Number of teeth	14	13
Diametral pitch (P_d)	3.15 teeth/cm (8 teeth/inch)	3.15 teeth/cm (8 teeth/inch)
Face width (F)	1.0 cm (0.71 in)	1.0 cm (0.71 in)
Pressure Angle	20°	20°
Input Torque (T)	4.16 N m (3.07 ft lb)	4.16 N m (3.07 ft lb)
Quality Number	12	12
Contact Geometry Factor (I)	0.055	0.055
Geometry Factor (J)	0.169	0.169
Load-distribution factor (K_m)	1.0	1.0
Size factor for pitting resistance (C_s)	0.49	0.49
Size factor for bending (K_s)	0.62	0.62
Crowning factor for pitting (C_{xc})	1.5	1.5
Stress cycle factor for pitting resistance (C_L)	1.0	1.0
Stress cycle factor for bending strength (K_L)	0.86	0.86
Allowable contact stress number (S_c)	1.08 GPa (156 ksi)	1.08 GPa (156 ksi)
Allowable bending stress number (S_t)	0.13 GPa (19 ksi)	0.13 GPa (19 ksi)
Maximum contact stress (σ_c)	1.42 GPa (206 ksi)	1.42 GPa (206 ksi)
Maximum bending stress (σ_b)	0.13 GPa (19 ksi)	0.13 GPa (19 ksi)
Wear Factor of Safety (S_H)	4.63	4.63
Bending Factor of Safety (S_F)	4.9	4.9
Weight	0.051 kg (0.11 lb)	0.037 kg (0.082 lb)

during operation. *Huma*'s shaft operates at 4195 RPM, 53% of the critical speed, 7970 RPM.

Table 12.4: Summary of primary belt and pulley data

Parameter	Driven Pulley	Driver Pulley
Rotational speed, full rotor speed	5127 RPM	4195 RPM
Pulley diameter	45 mm (1.77 in)	55 mm (2.17 in)
Static shaft tension	71.0 N (15.96 lbf)	71.0 N (15.96 lbf)
Dynamic shaft tension	278.6 N (62.63 lbf)	(62.63 lbf)

13 Avionics System

The avionics architecture is designed to enable fully autonomous operation in both day and night conditions. This level of autonomy enables safe operation even when communication is delayed or disrupted, a significant risk in disaster sites and at long ranges. It can carry out all mission segments on its own without the need for constant pilot input, enabling it to operate with only a minimal ground crew.

13.1 Components

Avionics components were selected to support safe autonomous operation and to allow the vehicle to achieve the mission requirements. The selected sensors, processing and control components, and communication equipment are described in the following sections.



13.1.1 Sensors

The onboard sensors, shown in Figure 13.1, were chosen to provide essential data for all mission segments. Sensors were selected to provide adequate redundancies in the event of an individual sensor failure in challenging conditions. Compactness and low power requirements were also prioritized.



Figure 13.1: External sensors.

- Cameras:** *Huma* is equipped with a total of 8 cameras to provide visual data across all mission segments. The vehicle includes two forward-facing e-con Systems STURDeCAM31 cameras to detect obstacles in front of the vehicle. These cameras feature high dynamic range, allowing it to produce quality images in glare and with varying light conditions. It also incorporates two additional side-facing STURDeCAM31 cameras, equipped with wide-field-of-view lenses, which provide visual coverage and detect obstacles on either side of the aircraft. *Huma* uses another two downward-facing FLIR Blackfly S cameras for ground and ship landings. These cameras feature a high resolution (2448×2048 pixels) and high sensitivity. *Huma* is also equipped with two downward-facing FLIR ADK thermal cameras, which can provide usable images in low light and fog. The forward- and downward-facing cameras are arranged in a stereo (two-camera) configuration to provide 3D depth information; this also provides redundancy in the event a single camera fails.
- Radar:** An Echoflight airborne radar, produced by Echodyne, is mounted inside the aircraft's nose. This ultra-low size, weight, and power radar is used to detect other aircraft and obstacles in front of the vehicle during cruise. The radar provides a long detection range, up to 2 km, allowing *Huma* to sense and avoid obstacles well in advance. Additionally, it is capable of detecting obstacles even in rain and heavy fog, conditions which are common in marine environments.
- Airspeed sensor:** An mRobotics Digital Airspeed Sensor provides forward airspeed information. The sensor features a 1 psi measurement range, allowing it to measure an airspeed of up to 100 m/s. To reduce the effect of rotor downwash on airspeed measurements, the static pressure port is located

inside the fuselage.

- **GNSS:** A CubePilot Here3 GNSS receiver provides global positioning data with a position accuracy of 2.5 m. The receiver also incorporates a magnetometer (compass) to provide heading information.
- **IMU (Inertial Measurement Unit), Altitude Sensor, and ADS-B In:** The IMUs, altitude sensors, and ADS-B In receivers are integrated directly into the onboard flight controllers. Each flight controller includes three IMUs, each consisting of an accelerometer and gyroscope, as well as one magnetometer to estimate yaw or heading and two barometers to measure altitude. Two of these three IMUs are vibration-isolated to reduce the impact of vibration on sensor measurements. The flight controller carrier board also incorporates an ADS-B In receiver, allowing it to detect and avoid other aircraft equipped with ADS-B Out. For improved data quality, the included ADS-B antenna is replaced with a longer, externally-mounted antenna.

13.1.2 Processing and Control

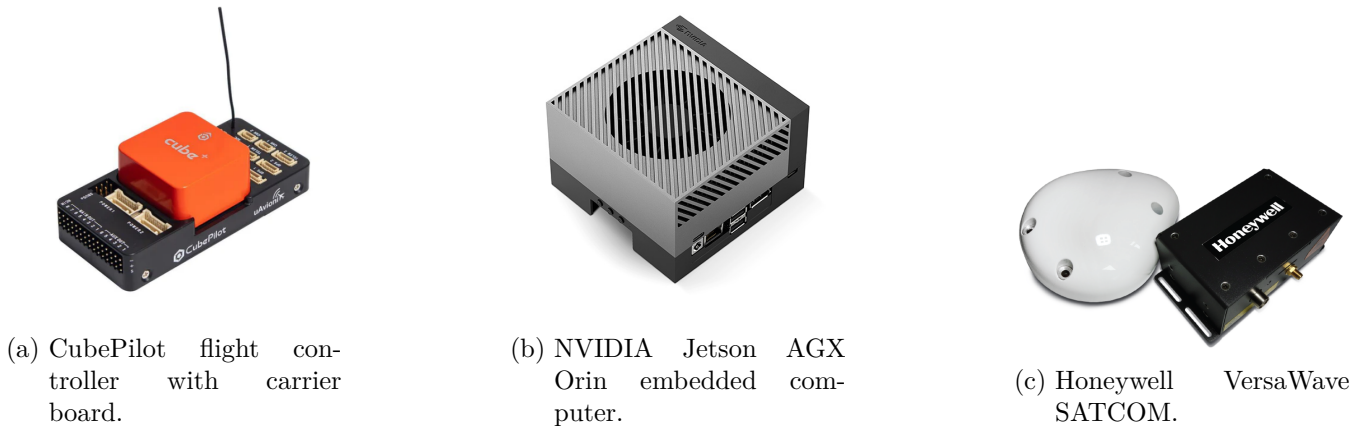


Figure 13.2: Processing and communications components.

- **Flight controller (Autopilot):** *Huma* includes three CubePilot The Cube Orange flight controllers, one main controller and two backup controllers. These run the aircraft control loop and state estimation filters and send commands to the actuators. The three flight controllers are arranged in a triple-redundant configuration; this allows any failure or fault with one flight controller to be detected by comparing controller outputs and state estimates with the other two. If a failure is detected on the main controller, one of the two backup controllers can take over.
- **Flight computer:** The NVIDIA Jetson AGX Orin 64GB computer was selected as the flight computer for this aircraft. It handles higher-level and computationally-intensive tasks, including image processing, sense-and-avoid, and path planning. The flight computer must be capable of processing images from multiple cameras simultaneously in real-time, a very computationally demanding task. This embedded computer is specialized for image processing and AI applications, making it well-suited to these tasks.

13.1.3 Communications

Huma is equipped with an external satellite communication system (SATCOM), the Honeywell VersaWave, allowing it to communicate with ground operators anywhere in the world. This SATCOM unit, which is

designed specifically for aircraft applications, was selected due to its low weight, size, and power requirements. The UAV must operate at distances of up to 185 km from its takeoff location, well outside the range of standard radio transmitters, making the SATCOM essential for reliable communication. LTE/cellular communication was not considered viable as *Huma* operates in disaster zones or over open ocean, where cellular networks are not operational or unavailable. Additionally, the SATCOM supports the long endurance mission by providing the backhaul needed for the onboard cell relay.

13.2 Autonomy

The following sections describe how *Huma* operates autonomously and safely in all mission segments using its onboard software and hardware.

13.2.1 State Estimation

Each state estimate can utilize multiple redundant sensors. This improves the quality and reliability of these estimates, and ensures that the vehicle can estimate its state even in the event of a sensor failure. For position, the estimate can be obtained using a combination of GNSS, optical navigation, barometer altitude measurements (for Z-position), and double integration of IMU (inertial) measurements. Multiple redundant IMUs are used to estimate attitude and can be integrated to estimate linear velocity; an airspeed sensor is also used to estimate forward velocity. Extended Kalman Filters are used to estimate the vehicle position, velocity, and attitude, fusing any available sensor measurements to produce highly robust estimates.

13.2.2 Ground and Ship Landing

Huma is capable of autonomously landing on both ground- and ship-based landing locations. It can identify these locations either by stored or transmitted coordinates or through computer vision techniques such as feature detection.

During descent and landing, *Huma* must avoid collisions with people or objects that may be present in the landing area. It uses the YOLOv8 (You Only Look Once) object detection model, which is capable of detecting and classifying objects in images in real time [65]. This model uses a neural network to both classify objects and generate bounding boxes in images obtained from the downward-facing landing cameras. The model is retrained using the COCO (Common Object in Context) dataset, which contains many common objects, with added aerial images of objects in both land and ship environments. Additionally,

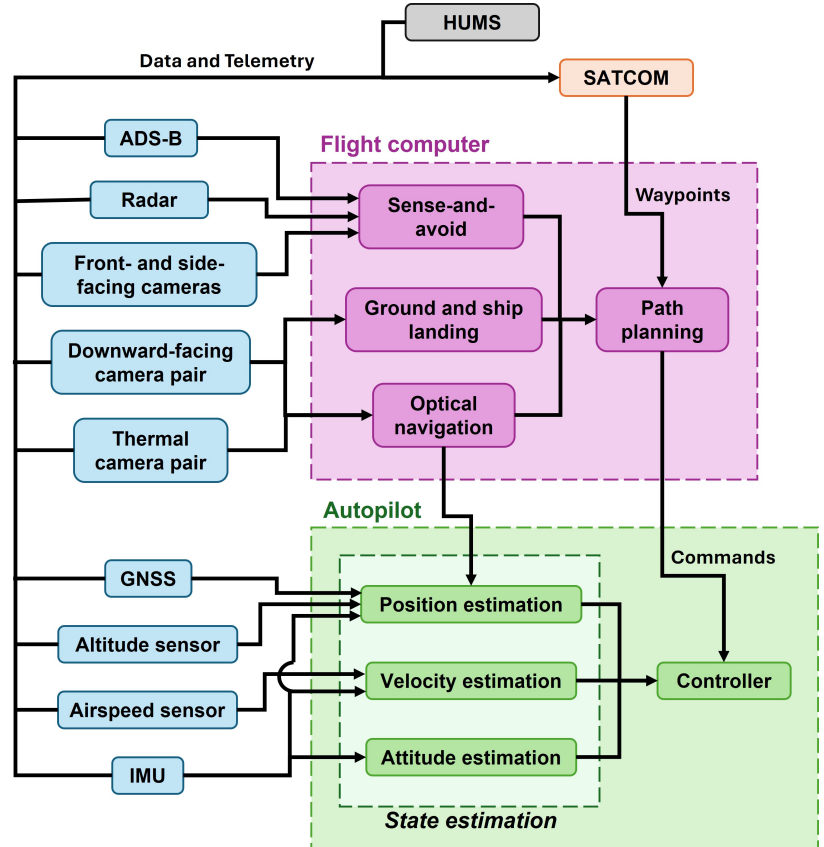


Figure 13.3: Avionics and autonomy architecture.

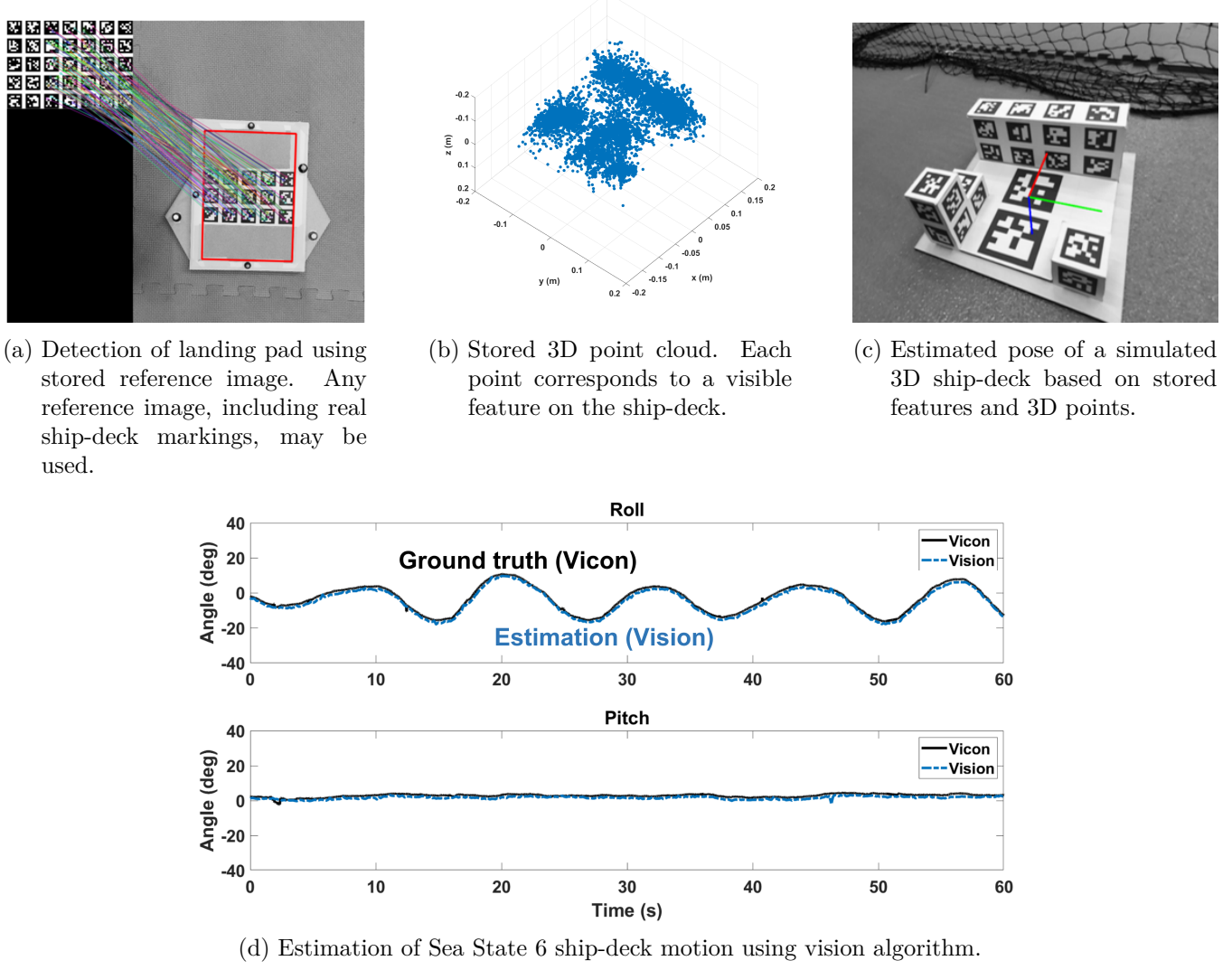


Figure 13.4: Feature-based ship-deck pose estimation algorithm.

the YOLOv8 model can be used with the thermal cameras during night landings with separate thermal vision datasets. For this, the model is trained using the Teledyne FLIR Thermal Images dataset, an example of which is shown in Figure 13.5(b), as well as additional thermal camera aerial images. The depth information provided by the stereo camera configuration is combined with the object detection output to localize the position of objects in 3D space. This allows the aircraft to alter its descent path to avoid these objects.

In the dynamic ship-deck environment, there is a major risk of pilot error when landing. *Huma* is able to carry out ship-deck landings fully autonomously, using only on-board sensors and hardware. The landing software algorithms offer a much faster response time than a human pilot with a lower chance of error. This offers improved safety to both the vehicle itself and the ship crew. *Huma* uses a procedure similar to human pilots to perform ship landings. While hovering above the ship-deck, it hovers above the center of the landing target, following its linear motion. The flight computer collects position and rotation data transmitted by the ship as well as position error from the flight controller, determining when it is safe to land. Ship-deck roll and pitch motion varies stochastically over time, so a landing is carried out during quiescent (calm) periods of motion. This requires that two conditions be met: 1) the ship deck

roll/pitch and roll/pitch rate must be within specified operating limits; and 2) the position error must be within specified limits. For helicopters, the operating limits for ship deck roll and pitch during launch and recovery are typically 8 and 3 degrees, respectively. These values are chosen such that the vehicle will not slide, tip over, or exceed structural limits [66]. Roll and pitch stability for *Huma* is discussed further in Section 10.7.2. When the two conditions are satisfied, the aircraft begins descending to the landing pad. If either position or rotation go out of bounds during this process, the landing is aborted, and the aircraft again hovers and waits for a safe landing window. This allows it to safely land on ships with varying levels of motion at both high and low sea states.

The RFP specifies that the ship transmits its position and orientation to the aircraft. However, in scenarios where relative pose data from the ship is not available to the aircraft, *Huma* is able to use vision algorithms to estimate the relative position and orientation using its existing cameras. A feature-based 2D algorithm can detect the pose of the ship-deck using the downward-facing cameras. Features can be described as small patches of interest in an image. They are robust to changes in illumination, rotation, and scale, and can be matched to identify objects across multiple images. Images of the existing 2D patterns on the ship-deck, such as helipad markings, can be matched to a stored 2D reference image. This is illustrated in Figure 13.4(a). The algorithm can then output the relative pose in real-time [67]. Using the front-facing cameras, a 3D feature-based algorithm can be used. This matches features on the 3D ship structures to stored features and 3D feature positions, generating position and rotation estimates [68]. Examples of stored feature positions and pose estimation are shown in Figures 13.4(b) and 13.4(c). The 2D and 3D algorithms are robust to visually degraded conditions potentially present in a ship-deck environment, such as occlusion or glare. Both algorithm outputs can be fused in a Kalman filter to produce robust pose estimates using only onboard hardware.

13.2.3 Sense-and-Avoid



Figure 13.5: Object detection and optical navigation algorithms.

Possible collision with obstacles, including birds or other aircraft, is a significant risk during the cruise and loiter segments. Therefore, *Huma* is equipped with avionics and software algorithms to perform real-time sense-and-avoid. The system can both identify the position and velocity of potential obstacles, and generate maneuvers to successfully avoid these obstacles.

To do this, the flight computer uses a combination of radar, ADS-B, and vision data to detect obstacles. The radar can track the position and velocity of obstacles in front of *Huma*, while the ADS-B In receiver can be used to detect any nearby aircraft equipped with ADS-B Out. Objects visible to the front- and side-facing cameras can be detected using the YOLOv8 object detection model, similarly to ground and ship landing. The cameras allow for detection of obstacles that may not be detected using radar or ADS-B,

such as small birds. This is illustrated in Figure 13.5(a).

The flight computer will estimate the trajectories of tracked obstacles, and determine if any will come within close range of the aircraft such that there is a risk of collision. If this is the case, the flight computer will generate avoidance maneuvers to maintain sufficient separation distance [69].

13.2.4 Optical Navigation

Huma uses optical navigation to supplement position estimates produced using GNSS and inertial measurements. Using images collected from its downward-facing cameras, the flight computer can match terrain features to stored maps, generating estimates of aircraft position. An example of terrain feature detection is shown in Figure 13.5(c). This will also allow the vehicle to navigate in the event of GNSS failure or denial, as inertial navigation alone is susceptible to drift. The camera images can also be analyzed for features of particular interest, such as landing sites.

13.2.5 Optional Remote Piloting

Though *Huma* is designed for autonomous operation, it can also be piloted remotely by a human operator if necessary. Using the equipped SATCOM, a pilot can command the vehicle from anywhere in the world. As the aircraft uses an SMR configuration, the pilot can utilize conventional rotorcraft controls. The onboard cameras transmit live video feed to the pilot, providing full visual awareness of the surroundings. Data from other sensors, including GPS, radar, and ADS-B In, is also transmitted. Autonomous operation can be resumed at the command of the operator or if communication is lost with the ground station.

13.3 Avionics Integration

13.3.1 Data Connections

The flight controller receives data from the IMUs, airspeed sensor, altitude sensors, GNSS, and ADS-B, while the flight computer receives information from the cameras and radar. The flight controllers continuously exchange data with the main flight computer through the USB connection. The flight controller sends commands to the actuators. Telemetry and flight data are sent to the ground station via the SATCOM connection, while the ground station can transmit new waypoints or commands to the flight computer.

13.3.2 Power Distribution

The alternator provides 14V power to the onboard avionics. This directly powers the radar and flight computer. As the SATCOM requires 28V power, a DC-DC converter is used to increase this voltage to 28V. The cameras and flight controllers are powered via the ports on the flight computer. In the event of alternator failure, critical avionics components can be powered using the onboard battery.

13.3.3 Mounting and Vibration Isolation

Figure 13.6 shows the placement of the avionics components.

The onboard cameras are mounted into cutouts in the fuselage. To reduce drag, the front- and side-facing cameras are mounted behind chemically-strengthened optical glass windows covering the fuselage cutouts. The downward-facing camera pairs are secured to the bottom of the internal avionics enclosure. As the two Blackfly S downward-facing cameras are not waterproof, they are fully enclosed inside the avionics section,



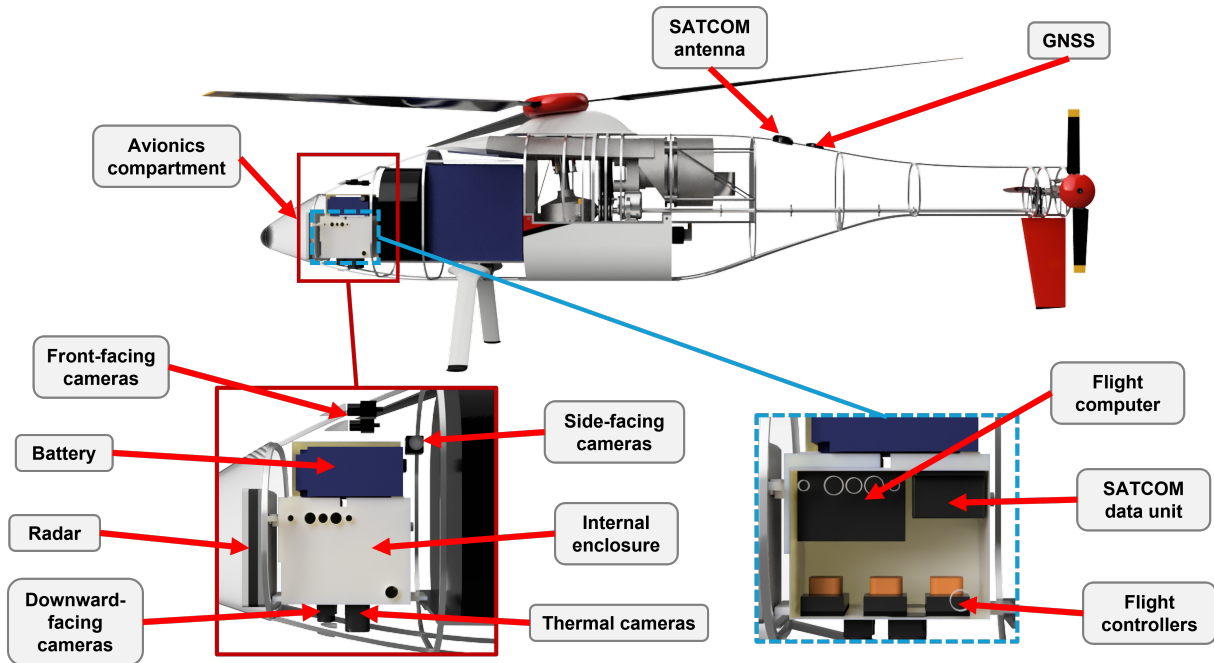


Figure 13.6: Diagram showing the placement of avionics and electrical components.

mounted behind additional optical glass windows. The thermal cameras are IP-rated water- and dust-proof; additionally, thermal cameras can only see through specialized IR-transparent materials. Therefore, the fuselage cutouts for the thermal cameras are left uncovered, exposing the camera lenses directly to the outside. Vibration can negatively affect camera image quality, introducing additional motion blur. To mitigate this, vibration-damping washers are used when mounting cameras.

The internal avionics components (the flight controllers, flight computer, and SATCOM data unit) are mounted inside a sealed avionics enclosure. The enclosure is water- and dust-proof and includes waterproof cable connectors. A bracket on the top of the enclosure holds the aircraft battery. The top and front sides of the enclosure are composed of aluminum straight-fin heat sinks to cool the flight computer and SATCOM data unit. The aluminum material also reduces the effects of EMI (electromagnetic interference) from the battery and radar on the internal components. For weight purposes, the remaining enclosure walls and battery mounting bracket are made of plastic. The flight controllers are mounted on vibration-reducing foam pads, further mitigating the effect of vibration on IMU readings.

The radar is mounted inside the vehicle nose, facing forward to detect obstacles in front. The nose is designed as a radome, which is constructed of fiberglass with stiffening ribs, allowing the radar signals to pass through unobstructed.

The SATCOM antenna and GNSS receiver require a clear line of sight to communication and GNSS satellites, respectively. Therefore, both of these components are mounted to the top of the fuselage.

13.4 Weight, Power, and Cost Summary

Table 13.1 provides a summary of the estimated weight, power, and cost of the avionics system. The selected components have a total weight of 4.67 kg (10.3 lb) and a maximum power usage of 176.8 W. The total cost is estimated to be 33,800 USD, of which the radar is the most expensive at 20,000 USD.

Table 13.1: Avionics weight, cost, and power summary.

Component	Quantity	Weight (kg)	Maximum power (W)	Cost (USD)
STURDeCAM31	4	0.04	1.3	300
FLIR Blackfly S	2	0.036	3	878
FLIR ADK	2	0.1	4	3,470
Echoflight	1	0.817	45	20,000
Honeywell SATCOM	1	0.51	44	500
CubePilot	3	0.073	2.5	350
Here3 GNSS	1	0.049	1	175
Airspeed Sensor	1	0.015	0.02	90
NVIDIA Jetson AGX Orin	1	2.13	60	2,000
Total		4.67	176.8	33,800

13.5 Health and Usage Monitoring System

The onboard Health and Usage Monitoring System (HUMS) monitors the status of critical onboard components and systems. Due to the low weight and size compared to larger helicopters typically equipped with HUMS, the design of the system is adapted to minimize weight and cost while still providing essential data for monitoring vehicle health. Accelerometers, temperature sensors, and strain sensors are placed in critical locations throughout *Huma*. Data from the sensors is monitored and logged by the main flight computer, which also runs monitoring algorithms which estimate the remaining useful life of onboard components. Information from the HUMS is available real-time to remote operators, or can be downloaded by ground crews after flight. The system will also warn operators if a fault is detected or if maintenance is required.

13.6 Electrical Power Components

Electrical power is provided to the avionics, actuators, and fuel pump with a Plane-Power AL12-EI60 14.2V, 60A alternator. The electrical system must be capable of supplying up to 800W of power as specified in the RFP, with 400W for the communications relay and up to 400W for avionics. At its rated voltage and current, it is capable of providing this required power. The engine has a small built-in alternator which is used as a secondary alternator, temporarily providing additional power if needed.

An earthX ETX680C 13.2V lithium iron phosphate (LFP) battery was chosen for the aircraft. LFP batteries have greater safety and stability from thermal runaway than other types of lithium-ion batteries, making them suitable for aircraft use. They are far lighter than lead-acid batteries.

The battery was selected based on the ability to power essential components for a minimum of 30 minutes in the event of alternator failure. This requirement is chosen based on FAA regulations, which require 30 minutes of safe operation with battery power [70], and to provide adequate time for the aircraft to land safely. Critical avionics components are the flight computer (in 15 W low-power mode), a single flight controller, the SATCOM, GPS, and forward- and downward-facing cameras. These items consume a total of 71 W of power. The four actuators for the main and tail rotor consume an additional 40 W each. With the selected battery, the vehicle can operate with critical components for 34 minutes.



Table 13.2: Electrical power components weight and cost summary.

Component	Quantity	Weight (kg)	Cost (USD)
ETX680C Battery	1	1.8	380
AL12-EI60 Alternator	1	3.1	1,600
Total		4.9	1,980

14 Weight and Balance

Component group weights were initially sized using the Tischenko and AFDD [9] models to inform initial analysis. These estimates were refined with digital CAD-based methodologies. This also provided robust estimates of the *Huma*'s center of gravity for both the lift compound and SMR configurations. A component-level weight breakdown is discussed in Table 14.1, with mission-specific add-ons, payload, and fuel requirements.

Table 14.1: Vehicle weight breakdown

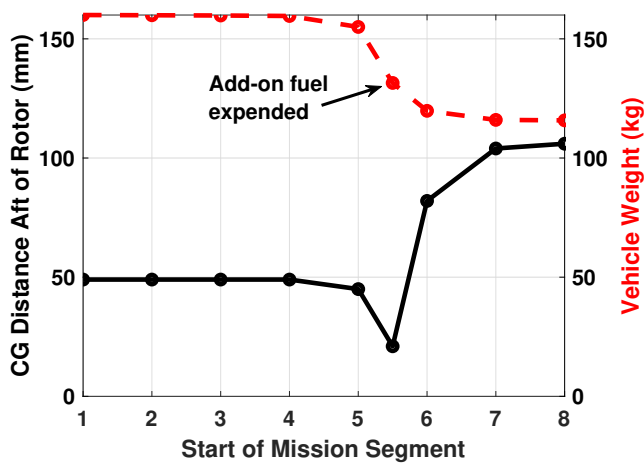
Component	Weight, kg (lb)	Component	Weight, kg (lb)
Structures	26.43 (58.27)	...	
Fuselage structure	9.52 (20.99)	Avionics/Electronics	10.87 (23.97)
Flooring and firewalls	1.00 (2.20)	Support Structure	1.3 (2.87)
Vertical stabilizer	0.21 (0.47)	Battery	1.80 (3.97)
Horizontal stabilizer	0.052 (0.11)	Alternator	3.10 (6.83)
Skin	12.78 (28.18)	Avionics suite	4.67 (10.30)
Pylon	0.11 (0.24)	Fuel System	2.10 (4.40)
Radome	0.65 (1.43)	Forward tank	1.70 (3.52)
Landing Gear	1.61 (3.55)	Collector Sump and Pump	0.40 (0.88)
Paint	0.5 (1.1)	Accessories	1.11 (2.45)
Powertrain	40.27 (88.76)	Total Empty Weight	87.05 (191.91)
UTP50R	31.75 (70.00)	Supplies Delivery	72.95 (160.83)
Shafts	1.12 (2.47)	Payload Case	4.40 (9.70)
Main Belt Drive	0.93 (2.05)	Enclosure Skin Panels	0.05 (0.11)
Main Gearbox	3.87 (8.51)	Payload	58 (127.87)
Intake and Exhaust	1.35 (2.98)	Jet-A Fuel	10.50 (23.15)
Engine Mount	0.79 (1.74)	Long Endurance	72.95 (160.83)
Tail Transmission	0.46 (1.01)	Add-on Fuel Tank	4.11 (9.06)
Main Rotor	5.24 (11.56)	Wing Adapter	0.76 (1.68)
Hingeless Hub	1.89 (4.17)	Wings	3.88 (8.55)
Main Rotor Blades	1.65 (3.64)	Payload	20 (44.09)
Fairing	0.32 (0.71)	Jet-A Fuel	44.20 (97.44)
Actuators	1.38 (3.04)	GTOW	160.00 (352.7)
Tail Rotor	1.03 (2.27)		
Tail Hub	0.91 (2.01)		
Tail Rotor Blades	0.12 (0.26)		
...			

During the long endurance mission, *Huma*'s center of gravity is forward of the aerodynamic center of its wings to ensure stability during forward flight. The CG experiences a longitudinal shift of 85mm (3.35 in) or

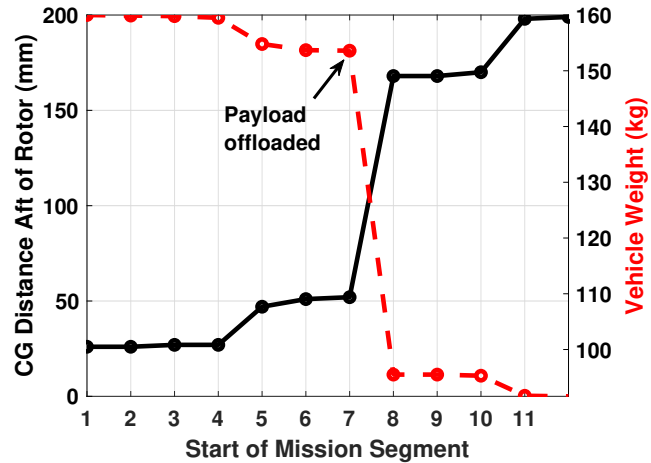


5.15% R. Longitudinal variation over each mission segment is discussed in Figure 14.1(a). Its forward-most position is reached during Mission Segment 5 as the add-on fuel tank is fully depleted during loiter, and its aft-most position is reached when both fuel tanks are fully depleted during landing. Lateral variation of the CG is less than a millimeter, and the vertical position of the CG raises upward 41mm (1.61 in) over the duration of the mission, as displayed in Figure 14.2(a).

During the supplies delivery mission, the vehicle is more susceptible to variation in its longitudinal CG. As the single fuel tank depletes, the CG shifts aft, but a significant change in CG occurs when payload is removed from the carrying case and forward payload bay. The extent of the longitudinal CG shift is tracked in Figure 14.1(b). The vehicle is shown to be stable in all flight segments in Section 15. Lateral variation of the CG is 1.15mm (0.05 in), while the vertical change of the CG is observed to be 47mm (1.85 in), with the extreme points of this sweep occurring when the vehicle is fully loaded, and empty of payload and fuel. Figure 14.2(b) captures the lateral and vertical movement of the CG for the supplies delivery mission.



(a) Longitudinal CG travel over the long endurance mission



(b) Longitudinal CG travel over the supplies delivery mission

Figure 14.1: Study of Longitudinal CG Travel

15 Flight Dynamics and Controls

Huma is a modular rotorcraft capable of operating with or without a wing. Consequently, flight dynamics and trim analyses are conducted for both configurations, taking into account the weight and center of gravity (CG) envelope. In the Single Main Rotor (SMR) configuration, the rotor system primarily generates the lift and control forces. In the lift-compound configuration, the wing unloads some of the lift required by the rotor during forward flight, creating a lift-sharing mechanism between the rotor and wing for extended endurance. However, the addition of another major lifting surface alters the rotorcraft dynamic characteristics. Therefore, the flight mechanics design must ensure that *Huma* maintains stable and controllable flight in both configurations without exceeding the control limits of the effectors. The control effectors for both configurations are the primary rotorcraft controls: main rotor collective, main rotor longitudinal and lateral cyclic, and tail rotor collective. To avoid the weight and cost penalties associated with additional control surfaces and actuators, the design limits the number of control surfaces to essential, non-redundant controls, provided that the basic controls are sufficient. A Dynamic Inversion controller is designed in-house for the *Huma* SMR configuration to stabilize the aircraft across the entire flight envelope. This controller

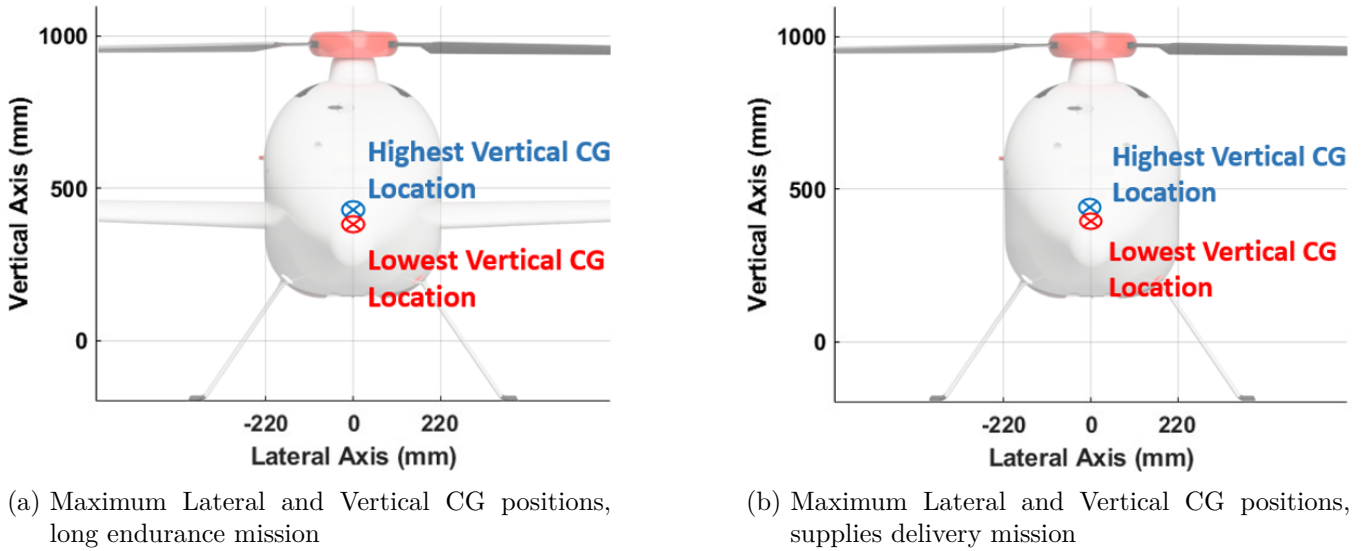


Figure 14.2: Study of Vertical and Lateral CG Travel

ensures the aircraft can operate under adverse gust and high wind conditions, which is especially crucial for shipboard operations.

15.1 Flight Dynamics Simulation Model

Flight dynamics modeling and simulation is performed using an in-house code developed at the University of Maryland (UMD) by the design team members.

The model contains a 6-degree-of-freedom rigid-body dynamic model of the fuselage, nonlinear aerodynamic lookup tables for the fuselage, rotor blades, wing, and empennage, rigid flap and lead-lag rotor blade dynamics, and a three-state Pitt-Peters inflow model [71]. The state vector contains the usual 9 rigid body states, 3 position states, 4 flapping and 4 lagging multiblade coordinates, and 3 dynamic inflow variables for both main and tail rotor.

The control inputs are:

$$\mathbf{u}^T = [\delta_{\text{lat}} \ \delta_{\text{lon}} \ \delta_{\text{col}} \ \delta_{\text{ped}}]$$

where δ_{lat} and δ_{lon} are the lateral and longitudinal cyclic inputs, δ_{col} is the collective input, and δ_{ped} is the pedal input.

The nonlinear model is trimmed at different flight conditions and then linearized at these equilibrium points. The resulting linear system is represented by:

$$\dot{\mathbf{X}} = \mathbf{AX} + \mathbf{BU} \quad (4)$$

The order of the linear model is then reduced by partitioning the state vector into fast and slow states to



enable a more tractable control design. This is achieved through residualization, a component of singular perturbation theory that pertains to linear time-invariant (LTI) systems [72]. As a result, the state vector is reduced to 8 states, excluding the yaw.

$$\mathbf{X}_s = [u \ v \ w \ p \ q \ r \ \phi \ \theta] \quad (5)$$

15.2 Trim Analysis

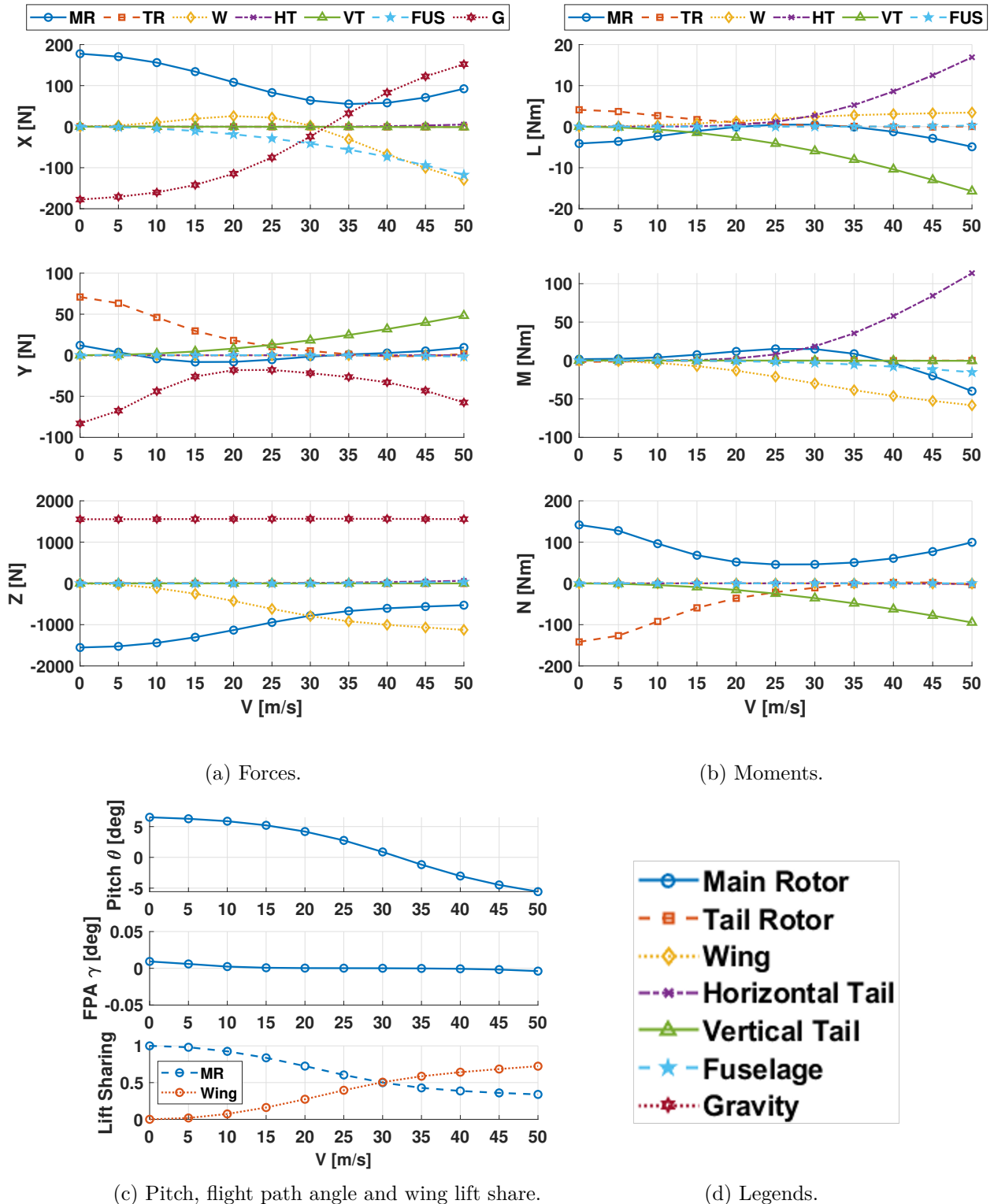
The trim problem aims to find the set of primary controls required to maintain the helicopter in equilibrium by balancing all acting forces and moments. The aircraft derivatives are taken about the trim condition, which are then used for stability analysis and flight control design. To achieve a trim solution, we adopted a strategy with a zero sideslip angle, which is standard for rotorcraft. Trim analyses are performed for both configurations of *Huma*: *Huma* SMR for a supply-delivery mission and *Huma* lift-compound (LC) for a long-endurance mission. The key difference is that the LC configuration uses a lifting wing to share the load with the main rotor, enhancing endurance.

Several key design features were determined by flight dynamics:

1. The horizontal tail plays a crucial role in enhancing the static and dynamic longitudinal stability. Without a horizontal tail, the rotorcraft exhibits highly unstable roots along the longitudinal axis. An inverted and one-sided horizontal tail is used to generate negative lift in forward flight, thereby maintaining pitch stability. An incidence angle of 2° was found to be optimal considering the flight envelopes of both configurations, eliminating the need for scheduling and additional actuators while maintaining effectiveness in high-speed cruise. Initially, the horizontal stabilizer was sized with a wetted area of 0.14 m^2 . This area was varied, and the stability roots were tracked to evaluate its effectiveness. It was determined that a horizontal tail area of 0.094 m^2 moved the poles favorably towards the left hand plane. To avoid both weight penalties and susceptibility to vertical gusts, the tail area was reduced by 50% with further stabilization managed through optimized control gains for each flight condition.
2. Vertical tail offers several advantages, such as streamlining the empennage section and in *Huma*'s case, the landing gear strut, supplementing directional stability, and unloading the tail rotor during forward flight [73]. Additionally, it can stabilize the rotorcraft in case of a tail rotor malfunction in high-speed forward flight. *Huma* features a one-sided downward vertical tail that covers the rear landing gear strut. This vertical tail is sized and set with a fixed pitch incidence of 2° to fully offload the tail rotor in cruise mode. However, due to its position below the CG, it creates a significant roll moment in cruise. This roll moment is largely neutralized by the one-sided horizontal tail, as evidenced by Figure 15.2(b) showing zero net forces and moments in trim conditions of cruise segments. Thus, excessive lateral cyclic input is successfully avoided for roll balance in cruise.
3. The wing in *Huma* lift-compound (LC) configuration designed to share about half of the rotor lift the during the loiter segment. It has a 4° fixed incidence angle to achieve its optimal angle of attack during the this segment, which lasts at least 10 hours. The wing is positioned slightly behind the aft CG of *Huma*, acting as a stabilizer rather than a destabilizer. This positioning also reduces the need for excessive longitudinal cyclic input to tilt the thrust vector during low-speed transition by supplementing the pitch-down moment.

Trim analyses are first conducted for the off-mission analysis of the long endurance *Huma* LC configuration. The aircraft is trimmed at discrete airspeeds, assuming the weight is always equal to the aircraft gross weight and the CG is nominal. As requested by RFP, the corresponding graphs of pitch angle, flight path angle, and wing lift fraction, along with zero net forces and moments, are presented in Figure 15.2. Forces and moments are presented in the body axis as shown in Figure 15.1. *Huma* hovers with a pitch angle of



Figure 15.2: Trim variables for off-mission analysis with *Huma* lift-compound configuration.

about 6° due to the shaft tilt implemented to improve forward flight efficiency. As it gains forward velocity, it begins to pitch down, flying with the best angle of attack of the wing at the designated loiter speed, which was aimed for during the initial sizing phase to enhance aerodynamic efficiency. At loiter speed, the



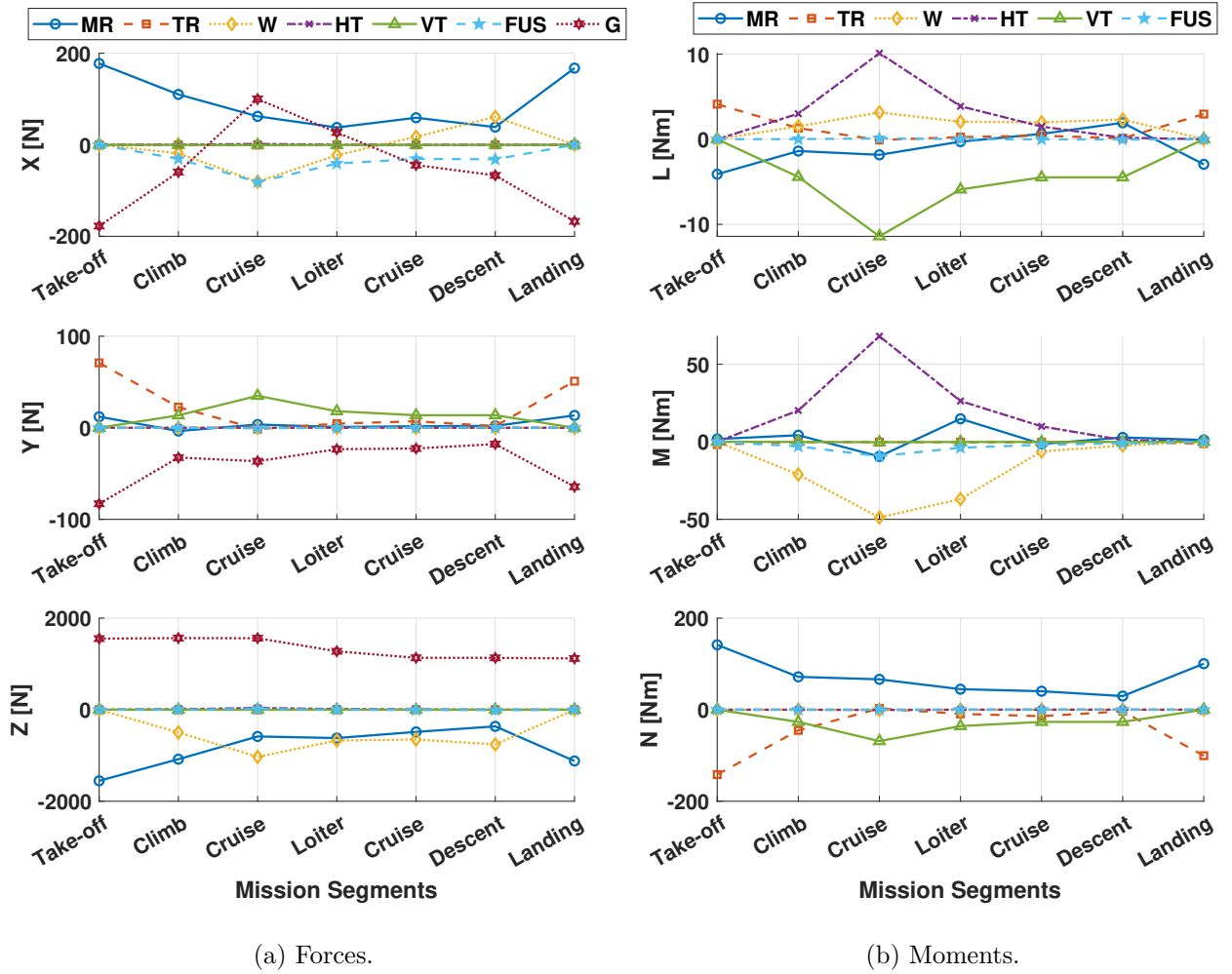


Figure 15.3: Trim forces and moments for long endurance mission analysis with *Huma* lift-compound configuration.

wing supports approximately 48% of the total lift required to sustain flight, as it was initially designed and optimized for.

Huma is also trimmed at each mission segment of both supply delivery and long endurance missions as required by RFP. These analyses account for weight and CG shifts during the mission. For each segment, the trim weight and CG are approximated as the average of that segment. Start-up and idle segments are ignored, and take-off and landing segments are represented as take-off hover and landing hover. Zero net forces and moments generated by all components for the trim condition of each mission segment are available for the *Huma* LC configuration in the long endurance mission in Figure 15.3 and for *Huma* SMR in the supply delivery mission in Figure 15.4. The required swashplate inputs are presented in Figure 15.5 for each mission separately. Collectives, θ_0 , for main and tail rotor values are presented as collectives at the root as applied to the swashplate.

15.3 Stability Analysis

The stability derivatives of each configuration in hover and cruise are shown in Table 15.1. Poles of SMR and lift-compound are illustrated in Figures 15.6 and 15.7 respectively. Coupled longitudinal/lateral



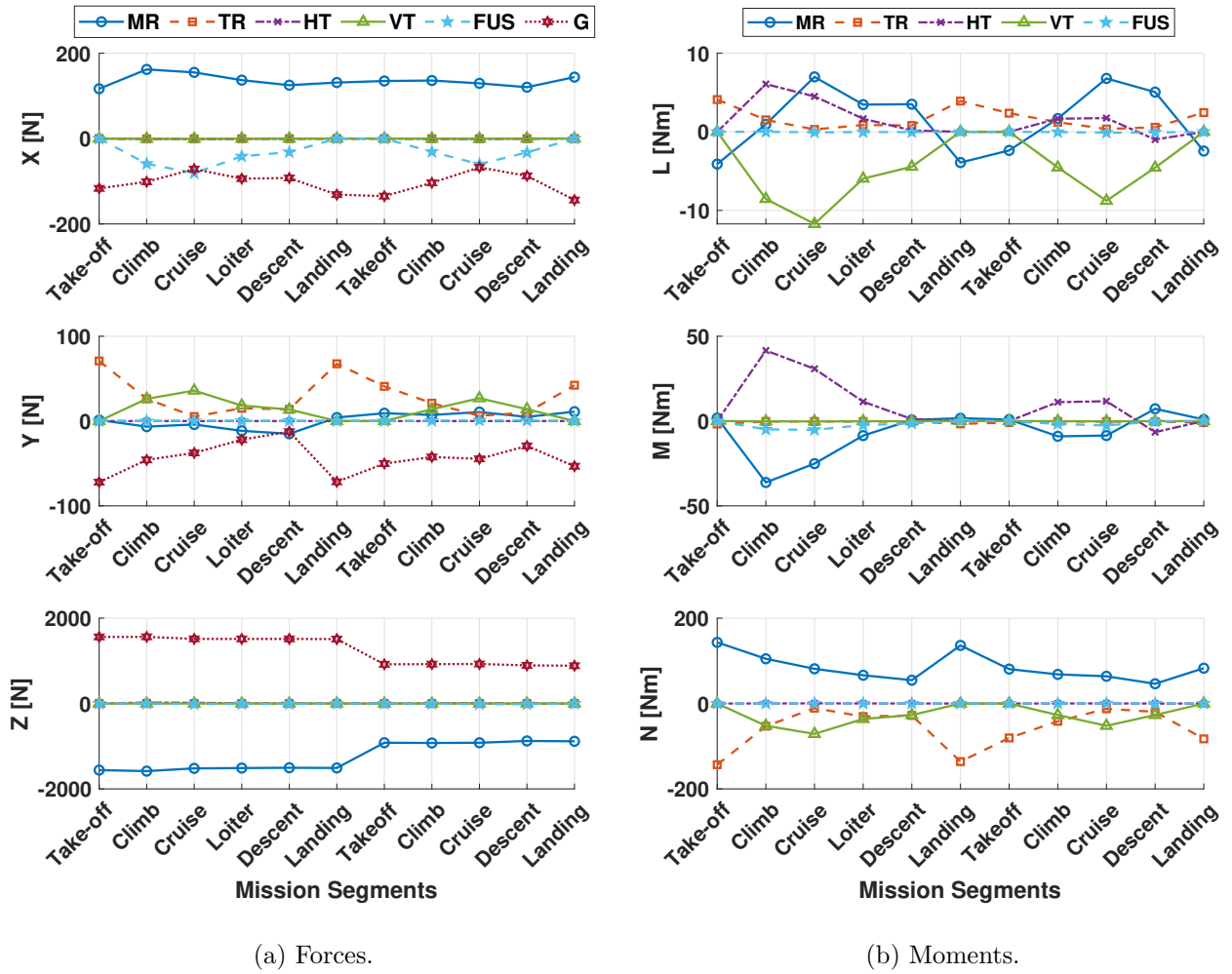
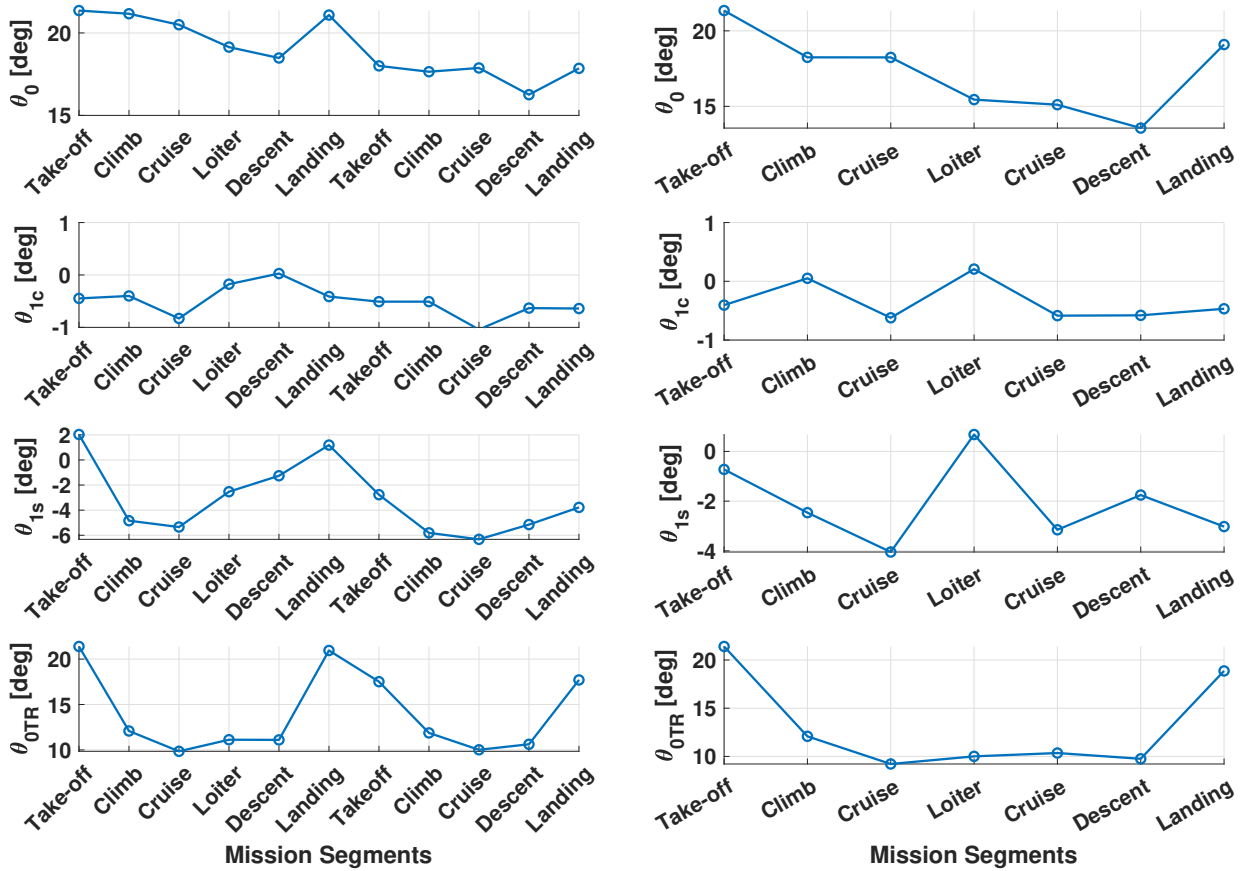


Figure 15.4: Trim forces and moments for supply delivery mission analysis with *Huma* SMR configuration.

derivatives likely have a significant influence on the response characteristics, generally showing a higher level of instability at low speeds [74]. However, for the purposes of stability analysis, we will make the approximation that the eigenvalues fall into two sets—longitudinal and lateral—to gain maximum physical insight by isolating the natural modes of motion.

In SMR configuration, *Huma* exhibits a phugoid pair that is unstable both in hover and forward flight, a characteristic inherent to helicopters. However, *Huma* SMR demonstrates a slightly more unstable phugoid mode at high speeds due to its hingeless rotor. The lateral phugoid mode of *Huma* at hover is marginally stable (positioned more to the left in the coupled analysis), evolving into a separate stable Dutch roll oscillation with frequency increasing strongly with speed. In other modes, significant roll subsidence occurs in the lateral axis, driven by large roll damping derivative L_p , while pitch subsidence occurs in the longitudinal axis, characterized by a significant pitch damping derivative M_q as presented in Table 15.1. Additionally, less-damped heave and spiral subsidences are observed in the longitudinal and lateral axes, respectively.

The addition of the wing compound did not significantly alter the hover dynamics. However, in forward flight, we observe a marginally stable phugoid mode in the longitudinal axis. This improvement is attributed to the correct positioning of the wing, as discussed in the trim analysis section which was iteratively refined through collaboration among the flight dynamics, mass properties, and structural design teams. Placing


 (a) Long endurance with *Huma* LC.

 (b) Supply delivery with *Huma* SMR.

Figure 15.5: Trim control inputs for both missions.

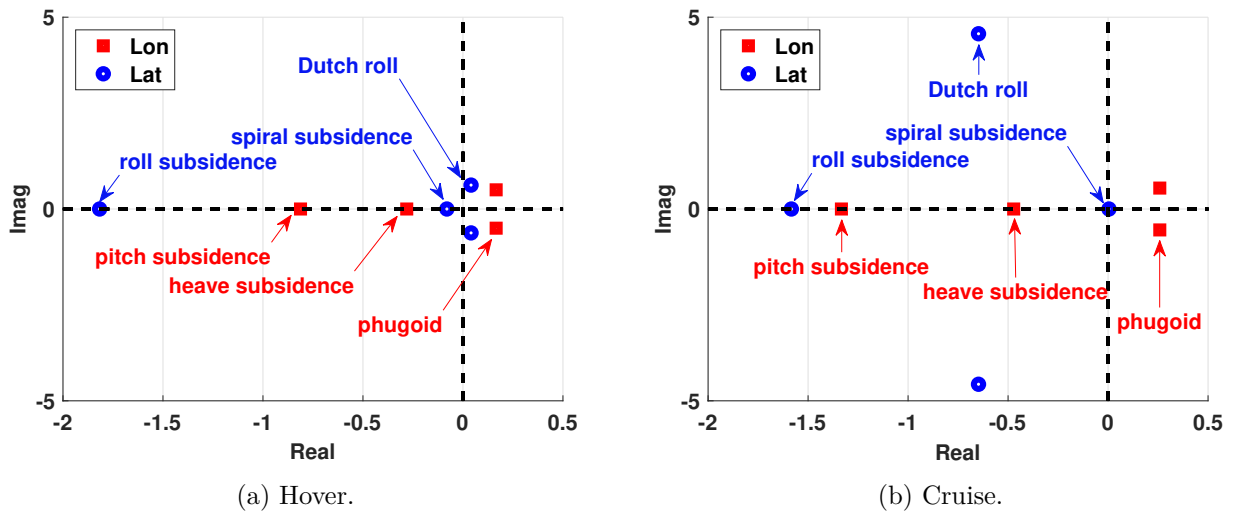
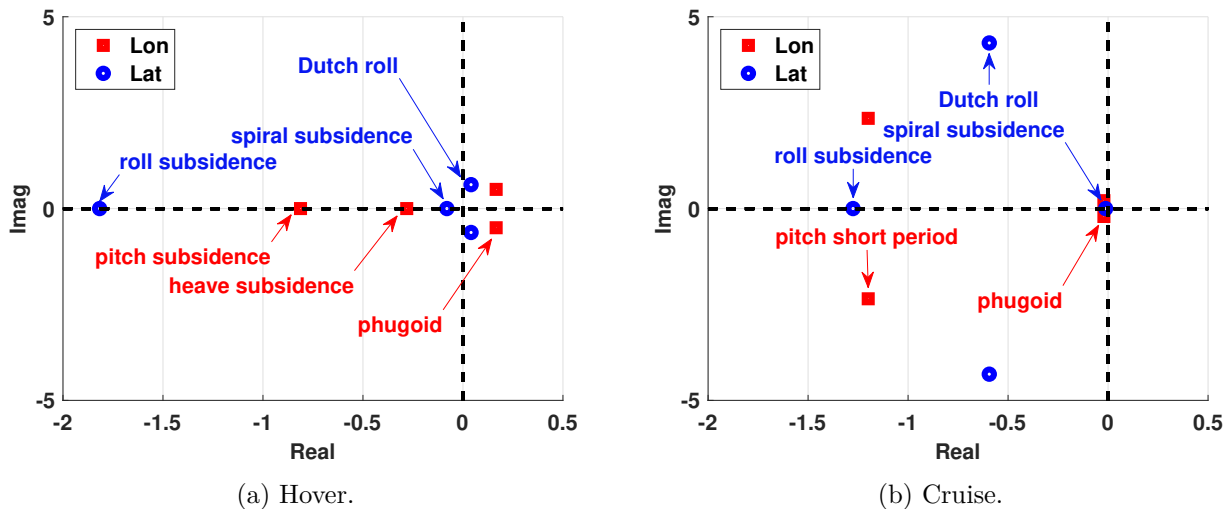

 Figure 15.6: Stability roots for *Huma* SMR configuration.

Table 15.1: Key stability derivatives of *Huma* in Hover and Cruise

Derivatives	SMR		Lift Compound		Units
	Hover	Cruise	Hover	Cruise	
X_u	-0.03	-0.04	-0.03	-0.06	1/sec
M_u	0.02	0.04	0.02	-0.01	rad/sec-m
X_w	0.02	0.04	0.02	0.15	1/sec
M_w	0.01	0.01	0.01	-0.14	rad/sec-m
X_q	0.12	-1.94	0.12	2.98	m/rad-sec
M_q	-0.46	-0.60	-0.46	-0.58	1/sec
Z_u	0.03	0.03	0.03	0.00	1/sec
L_v	-0.08	0.08	-0.08	0.07	rad/sec-m
Z_w	-0.28	-0.65	-0.28	-1.81	1/sec
L_p	-1.57	-1.60	-1.57	-1.31	1/sec
Z_q	0.01	41.30	0.01	41.20	m/rad-sec
L_r	-0.02	-0.22	-0.02	-0.12	1/sec
Y_v	-0.03	-0.15	-0.03	-0.14	1/sec
N_v	0.08	0.52	0.08	0.46	rad/sec-m
Y_p	-0.11	1.93	-0.11	-3.02	m/rad-sec
N_p	0.06	0.08	0.06	0.07	1/sec
Y_r	0.01	-40.92	0.01	-40.88	m/rad-sec
N_r	-0.21	-1.12	-0.21	-1.03	1/sec

Figure 15.7: Stability roots for *Huma* lift-compound configuration.

the wing behind the aft CG causes it to act in a stabilizing manner. This tendency is evident, particularly in the positive destabilizing derivative M_u turning slightly negative. Additionally, we observe a better-damped heave subsidence mode, attributable to the 3-fold increase in the negative heave damping term Z_w . Add to that, heave and pitch modes are coupled, creating a pitch short period. Therefore, *Huma* LC in cruise resembles a classical fixed-wing set: pitch short period, phugoid, Dutch roll, spiral, and roll subsidence.

15.4 Flight Control Design

Huma SMR open loop dynamics are unstable as discussed in stability analysis section and naturally diverges over time when a control input or disturbance is applied, as illustrated in figure 15.8 for a harmonic gust. Therefore, at first a stability augmentation system must be implemented to stabilize the helicopter, then position controllers are implemented to hold a specific altitude or compensate for drifts at any axis coming from the windy environment and gust disturbances. The control loop consists of inner and outer loops, first to stabilize the aircraft and then to hold altitude and position.

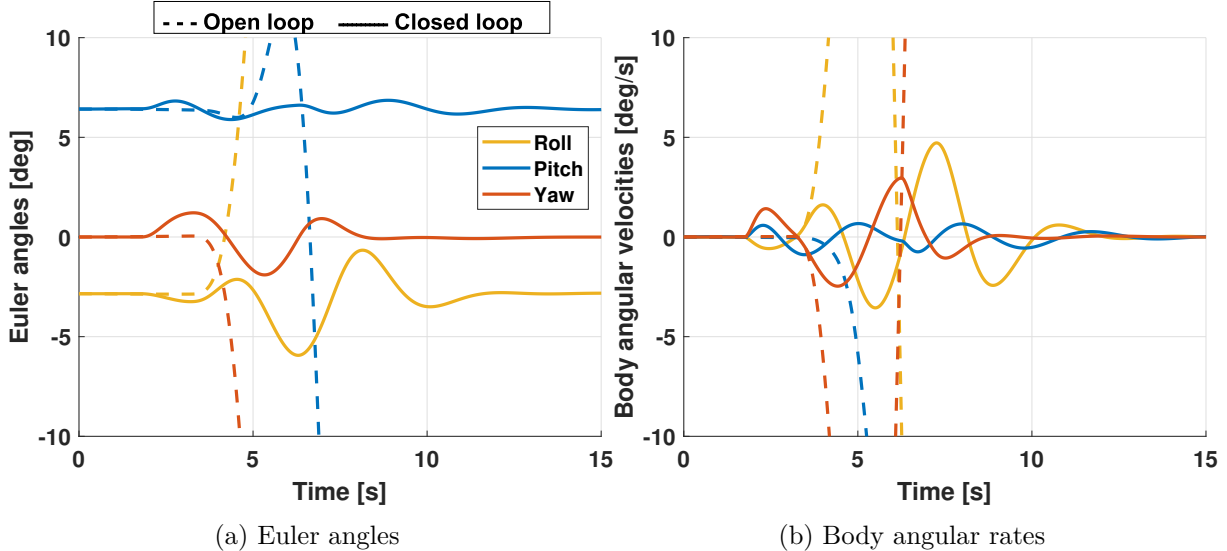


Figure 15.8: Open loop vs Closed loop response for *Huma* SMR with 8 m/s side gust at hover

Huma SMR is the chosen configuration to develop the control laws for and to perform the gust rejection. However, the control laws could also be applied for *Huma* LC configuration because the vehicle controls and DI architectures are the same in both configurations.

15.4.1 Controller Architecture

The control strategy is based on the Dynamic Inversion (DI) control architecture [75], [76]. Dynamic inversion uses feedback linearization technique by inverting the plant model that results in having the output follow the input of a command model that has comparable dynamics as the vehicle dynamics. DI control law provides feedforward and feedback paths which makes it well-suited for the high wind and gust rejection mission requirements. Instead of having full-state feedback, the reduced linear model with the rigid body states coupled is sufficient and could be used in the plant inversion. This means model scheduling for each flight condition will be only needed in feedback linearization loop which is an advantage of DI over other model following controllers such as Explicit Model Following controller (EMF) which additionally needs to schedule the inverse model command model and hence the feedforward path. Another advantage of DI over EMF is that a multi-input multi-output (MIMO) state space representation is easily employed, which facilitates both design and implementation processes.

To stabilize *Huma* SMR dynamics, an Attitude Command Attitude Hold (ACAH) controller ensures that the plant's actual attitude follows the input attitude command. The lateral axis control is shown in Figure 15.9. The ACAH controller is divided into three parts: command filter, feedback compensation, and feedback linearization. Due to the highly windy and gusty environment of shipboard operations, *Huma* SMR needs to have the yaw axis controlled and to compensate for heading changes using ACAH during

hover after takeoff and before landing. However, in forward flight as velocity increases, a Rate Command Attitude Hold (RCAH) controller is used with turn coordination.

The control strategy adapts to different phases of the flight envelope, requiring distinct controls for hover and forward flight. A mix of position and velocity controllers will be used in the outer loop in addition to the ACAH controllers in the inner loop. Position control holds the altitude and rejects sideways disturbances, while the velocity controller maintains cruise speed. Inner loop controllers ensure that the helicopter is stable and follows the commands from the outer loop controllers so that roll, pitch, and yaw attitudes track the commanded signals. Turn coordination is active in high-speed cruise (i.e., above 60 knots) while at hover and low forward speeds (i.e., below 40 knots), the tail rotor has full authority. In between these speeds, a blend of yaw commands and turn coordination is used.

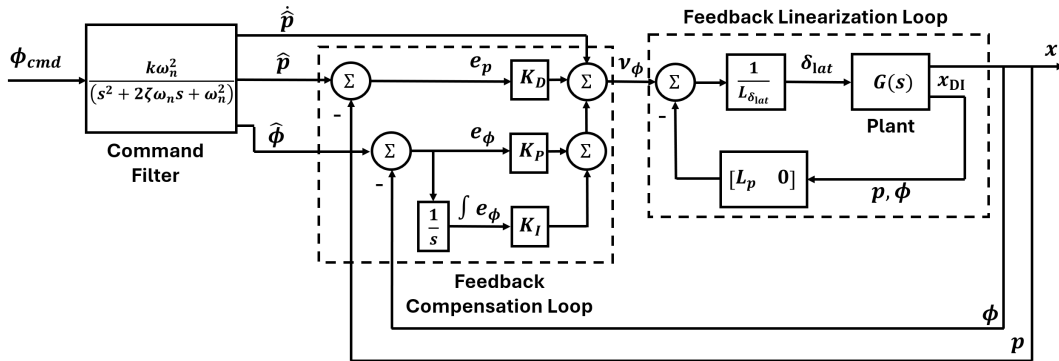


Figure 15.9: Example of an ACAH DI controller for lateral axis

The state space representation of the inner loop (IL) ACAH DI controller for the coupled system of vehicle attitudes is shown below:

$$\dot{\mathbf{x}}_{\text{DI}} = \underbrace{\mathbf{A}_{\text{DI}}}_{\mathbf{A}_{\text{res}}} \mathbf{x}_{\text{DI}} + \underbrace{\mathbf{B}_{\text{DI}}}_{\mathbf{B}_{\text{res}}} \underbrace{\begin{bmatrix} \delta_{\text{lat}} \\ \delta_{\text{lon}} \\ \delta_{\text{ped}} \end{bmatrix}}_{\mathbf{u}_{\text{DI}}} \quad (6a)$$

$$\underbrace{\begin{bmatrix} \phi \\ \theta \\ \psi \end{bmatrix}}_{\mathbf{y}_{\text{DI}}} = \underbrace{\begin{bmatrix} 0 & 0 & 0 & 0 & 0 & 0 & 1 & 0 & 0 \\ 0 & 0 & 0 & 0 & 0 & 0 & 0 & 1 & 0 \\ 0 & 0 & 0 & 0 & 0 & 0 & 0 & 0 & 1 \end{bmatrix}}_{\mathbf{C}_{\text{DI}}} \mathbf{x}_{\text{DI}} \quad (6b)$$

Where, $\mathbf{x}_{\text{DI}} = [u, v, w, p, q, r, \phi, \theta, \psi]^T$, and $\mathbf{A}_{\text{res}}, \mathbf{B}_{\text{res}}$ are extracted from the residualized slow states linear model. Hence, the actual control inputs to the open loop system are

$$\begin{bmatrix} \delta_{\text{lat}} \\ \delta_{\text{lon}} \\ \delta_{\text{ped}} \end{bmatrix} = (\mathbf{C}_{\text{DI}} \mathbf{A}_{\text{DI}} \mathbf{B}_{\text{DI}})^{-1} \left(\begin{bmatrix} \nu_{\phi} \\ \nu_{\theta} \\ \nu_{\psi} \end{bmatrix} - \mathbf{C}_{\text{DI}} \mathbf{A}_{\text{DI}}^2 \mathbf{x}_{\text{DI}} \right) \quad (7)$$

with,

$$\nu_{\phi} = \dot{p} + K_D e_p + K_P e_{\phi} + K_I \int_0^t e_{\phi} d\tau \quad (8)$$



where the tracking errors in the roll axis are defined as $e_p = \hat{p} - p$, $e_\phi = \hat{\phi} - \phi$. Similarly is ν_θ and ν_ψ with the corresponding tracking errors in pitch, and yaw axis defined as $e_q = \hat{q} - q$, $e_\theta = \hat{\theta} - \theta$, and $e_r = \hat{r} - r$, $e_\psi = \hat{\psi} - \psi$, respectively. K_P, K_I, K_D are the feedback compensation proportional, integral, and derivative gains, respectively.

Consider a Translational Rate Command (TRC) controller for the outer loop (OL) that maintains longitudinal, lateral, and vertical velocities in the heading frame. The control inputs for this controller are roll and pitch attitudes, as well as the collective stick. The command filter is a first-order model because the response of linear velocities to the control inputs resembles a first-order system response. The state-space representation for the approximated MIMO system is:

$$\underbrace{\begin{bmatrix} \dot{u} \\ \dot{v} \end{bmatrix}}_{\dot{\mathbf{x}}_{\text{DI}_{\text{OL}}}} = \underbrace{\begin{bmatrix} X_u & 0 \\ 0 & Y_v \end{bmatrix}}_{\mathbf{A}_{\text{DI}_{\text{OL}}}} \underbrace{\begin{bmatrix} u \\ v \end{bmatrix}}_{\mathbf{x}_{\text{DI}_{\text{OL}}}} + \underbrace{\begin{bmatrix} X_\phi & X_\theta \\ Y_\phi & Y_\theta \end{bmatrix}}_{\mathbf{B}_{\text{DI}_{\text{OL}}}} \underbrace{\begin{bmatrix} \phi \\ \theta \end{bmatrix}}_{\mathbf{u}_{\text{DI}_{\text{OL}}}} \quad (9a)$$

$$\underbrace{\begin{bmatrix} V_x \\ V_y \end{bmatrix}}_{\mathbf{y}_{\text{DI}_{\text{OL}}}} = \underbrace{\begin{bmatrix} 1 & 0 \\ 0 & 1 \end{bmatrix}}_{\mathbf{C}_{\text{DI}_{\text{OL}}}} \underbrace{\begin{bmatrix} u \\ v \end{bmatrix}}_{\mathbf{x}_{\text{DI}_{\text{OL}}}} \quad (9b)$$

Then, the OL DI control law will be given by:

$$\begin{bmatrix} \phi_{\text{cmd}} \\ \theta_{\text{cmd}} \\ \delta_{\text{col}} \end{bmatrix} = (\mathbf{C}_{\text{DI}} \mathbf{B}_{\text{DI}})^{-1} \left(\begin{bmatrix} \nu_{V_x} \\ \nu_{V_y} \\ \nu_{V_z} \end{bmatrix} - \mathbf{C}_{\text{DI}} \mathbf{A}_{\text{DI}} [\mathbf{x}_{\text{DI}_{\text{OL}}}] \right) \quad (10)$$

with,

$$\nu_{V_x} = \dot{V}_x + K_P e_{V_x} + K_I \int_0^t e_{V_x} d\tau \quad (11)$$

where the tracking error in the longitudinal speed is defined as $e_{V_x} = \hat{V}_x - V_x$, and K_P, K_I are the feedback compensation proportional and integral gains, respectively. Similarly are for lateral, and vertical speeds ν_{V_y} and ν_{V_z} with the corresponding tracking errors, $e_{V_y} = \hat{V}_y - V_y$, and $e_{V_z} = \hat{V}_z - V_z$. At cruise, $V_{x_{\text{cmd}}} = V_{\text{cruise}}$, while $V_{y_{\text{cmd}}} = V_{z_{\text{cmd}}} = 0$.

During mission segments such as take-off, climbing or descending to a certain altitude, and landing, a position command position hold controller is implemented, exhibiting the same architecture as the ACAH DI controller but with feedback states changed to inertial frame velocities and positions

$$[\mathbf{x}_{\text{DI}_{\text{OL}}}] = [\dot{x}, \dot{y}, \dot{z}, x, y, z]$$

and the tracking output

$$[\mathbf{y}_{\text{DI}_{\text{OL}}}] = [x, y, z]$$

then adding the appropriate elements in $\mathbf{A}_{\text{DI}_{\text{OL}}}, \mathbf{B}_{\text{DI}_{\text{OL}}}, \mathbf{C}_{\text{DI}_{\text{OL}}}$. Hence, the OL DI control law is:

$$\begin{bmatrix} \phi_{\text{cmd}} \\ \theta_{\text{cmd}} \\ \delta_{\text{col}} \end{bmatrix} = (\mathbf{C}_{\text{DI}_{\text{OL}}} \mathbf{A}_{\text{DI}_{\text{OL}}} \mathbf{B}_{\text{DI}_{\text{OL}}})^{-1} \left(\begin{bmatrix} \nu_x \\ \nu_y \\ \nu_z \end{bmatrix} - \mathbf{C}_{\text{DI}_{\text{OL}}} \mathbf{A}_{\text{DI}_{\text{OL}}}^2 [\mathbf{x}_{\text{DI}_{\text{OL}}}] \right) \quad (12)$$

with,

$$\nu_x = \ddot{x} + K_D \dot{e}_x + K_P e_x + K_I \int_0^t e_x d\tau \quad (13)$$



where the tracking error in longitudinal position is defined as $e_x = \dot{\hat{x}} - \dot{x}$, and $e_x = \hat{x} - x$. K_P, K_I, K_D are the feedback compensation proportional, integral, and derivative gains, respectively. Similarly are ν_y and ν_z with the corresponding tracking errors, $e_y = \dot{\hat{y}} - \dot{y}$, $e_y = \hat{y} - y$, and $e_z = \dot{\hat{z}} - \dot{z}$, $e_z = \hat{z} - z$. For hover, $x_{cmd}, y_{cmd}, z_{cmd}$ are the desired spatial point for hovering.

15.4.2 Closed Loop Stability and Control

With the control laws described in the previous section, *Huma* is capable of sustaining stable and controllable flight in all flight segments. To demonstrate this capability, time response simulations are performed in various flight conditions. Figure 15.10 shows the vertical axis control using TRC and ACAH DI controller in two cases: hover and forward flight with a velocity of 15 m/s (50 ft/s). The time responses of body velocities in the heading frame due to a doublet command of a vertical velocity of 2.1 m/s (7 ft/s), as required by the mission specifications for climb and descent mission segments, are illustrated. Figure 15.10(a) shows that the vehicle follows the command in a first-order behavior similar to the command model while maintaining the off-axis states at trim values. Figure 15.10(b) indicates that the main swash-plate input comes from the collective in hover, as expected. In forward flight, the collective is needed to follow the vertical command, along with the longitudinal cyclic to maintain the designated forward velocity. Additionally, the unloading of the tail rotor by the vertical tail can be observed from the tail rotor collective levels for both flight conditions.

Furthermore, the aircraft's time response to a unit step input in both hover and cruise conditions is represented in Figure 15.11. Inputs are applied along all three axes. In each axis, the aircraft's response shows small overshoot and plausible settling time, demonstrating that the aircraft is stable and controllable in different flight segments with the desired dynamical response characteristics.

15.4.3 Wind and Gust Rejection Simulation

The requirement is to demonstrate that the vehicle can perform a ship-board vertical take-off and landing subject to high-wind and gusty conditions, maintaining a spatial accuracy of 1 meter for aircraft recovery. The control architecture designed to meet this criterion consists of an inner loop stability augmentation system to stabilize the rigid body states and an outer loop position controller to keep the aircraft within the restricted landing zone, better than the given spatial accuracy, while recovering from adverse conditions. Additionally, the heading control ensures that the aircraft's heading attitude remains consistent during both landing and take-off.

For the gust rejection, the requirement is specifically to reject a gust of 5 m/s (16 ft/s) during launch and recovery with the most challenging direction and period. Since *Huma* is capable of rejecting a higher gust, an 8 m/s (26 ft/s) gust is used for further analysis. The gust is modeled based on a 1-cos harmonic profile for a single period, as recommended by the RFP and certification authorities [77].

$$V(t) = \begin{cases} \frac{1}{2}V_{gust} \left(1 - \cos\left(\frac{2\pi t}{T}\right)\right) & \text{for } 0 \leq t \leq T \\ 0 & \text{for } t > T \end{cases} \quad (14)$$

Side gusts were found to be more challenging than gusts along other axes during takeoff and landing. Both directions of the side gust are shown in Figure 15.13 during landing. Among these, the east-side gust, as defined in the inertial north-east-down (NED) frame, which puts the tail rotor in descent mode, is identified as the most critical and demanding one. The results align with the expected behavior of the controller on the tail rotor collective. Specifically, the collective pitch decreases in response to an east gust due to the descent state, whereas it increases in response to a west gust to counteract an unwanted



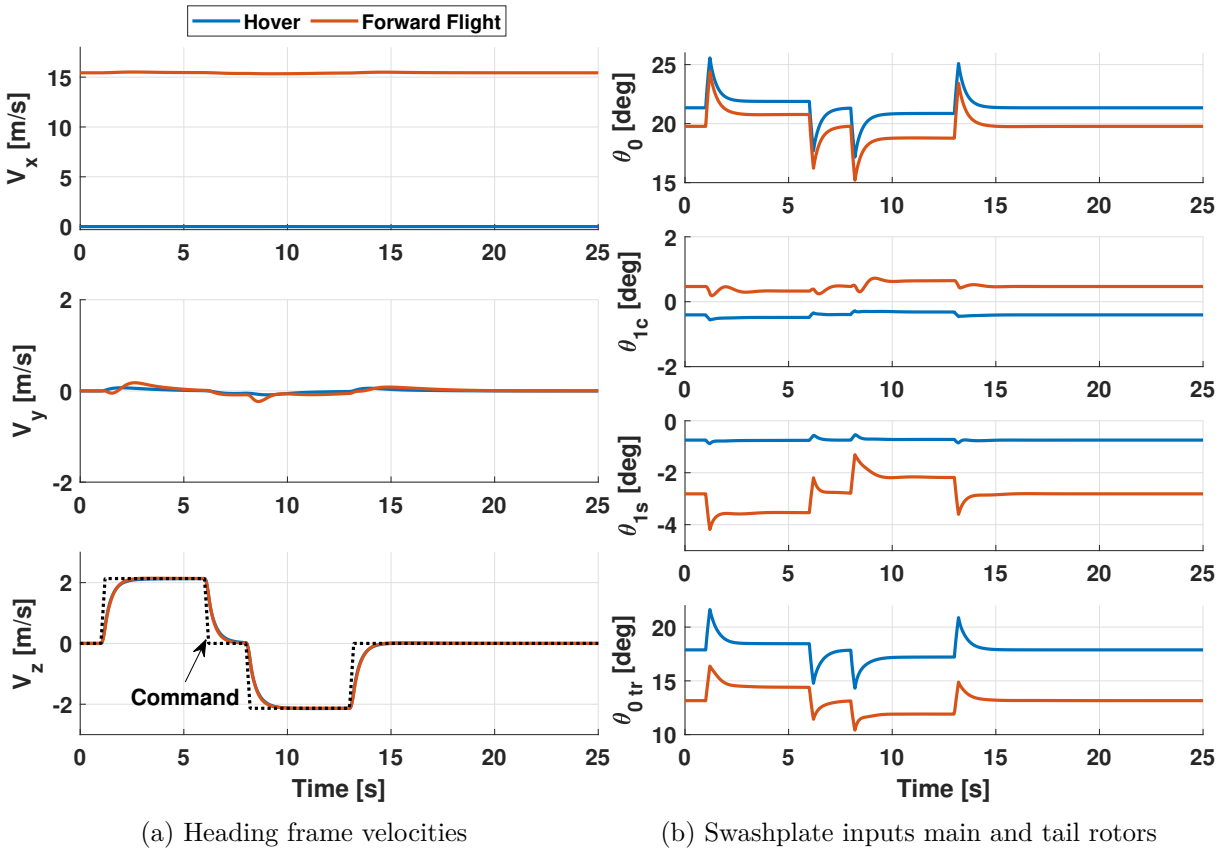


Figure 15.10: Time simulation for vertical and forward climb/descend mission segments

climb. Consequently, the yaw axis adjustments follow the tail rotor actions. Additionally, more lateral cyclic input is required for an east gust, while less longitudinal cyclic input is needed for a west gust. As the vehicle is descending, the controller on the main rotor swashplate reduces the collective pitch, showing minimal variation across different gust directions.

Add to that, various gust lengths were surveyed to determine the most challenging gust period. The first and second periods used are 0.15 s and 1.5 s respectively, similar to a recent study on helicopter gust response in hover and forward flight [78]. The third and fourth are longer ones, resulting in gust lengths of 3 seconds and 5 seconds, respectively. Consequently, these varying gust lengths are simulated with the east-side gust during landing. The respective gust shapes and *Huma*'s time response to them are illustrated in Figure 15.14. Examining the figure, a gust period of $T = 1.5$ s induces the highest excitation in body rates instantaneously, while a period of $T = 5$ s, likely too long for a realistic gust condition, results in the largest position displacement especially in lateral axis. Our controller can reject all gust periods as surveyed here. However, we will take 5 s gust, although it's too long in reality, to show our controller is capable of rejecting gust

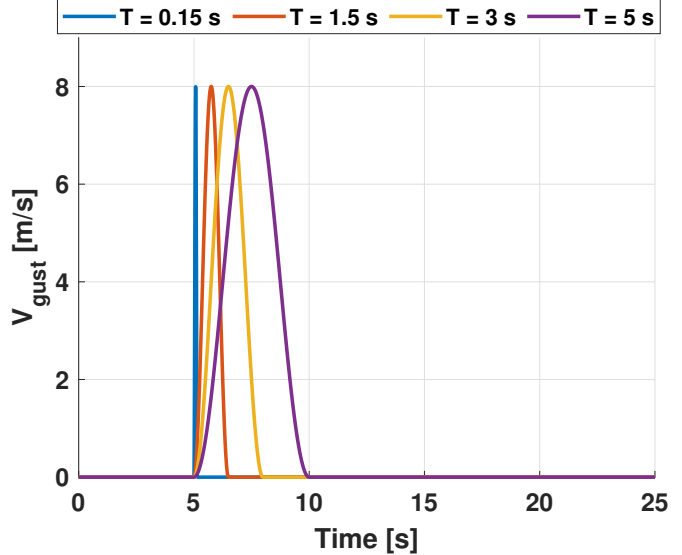


Figure 15.12: 1-cos gust with varying lengths

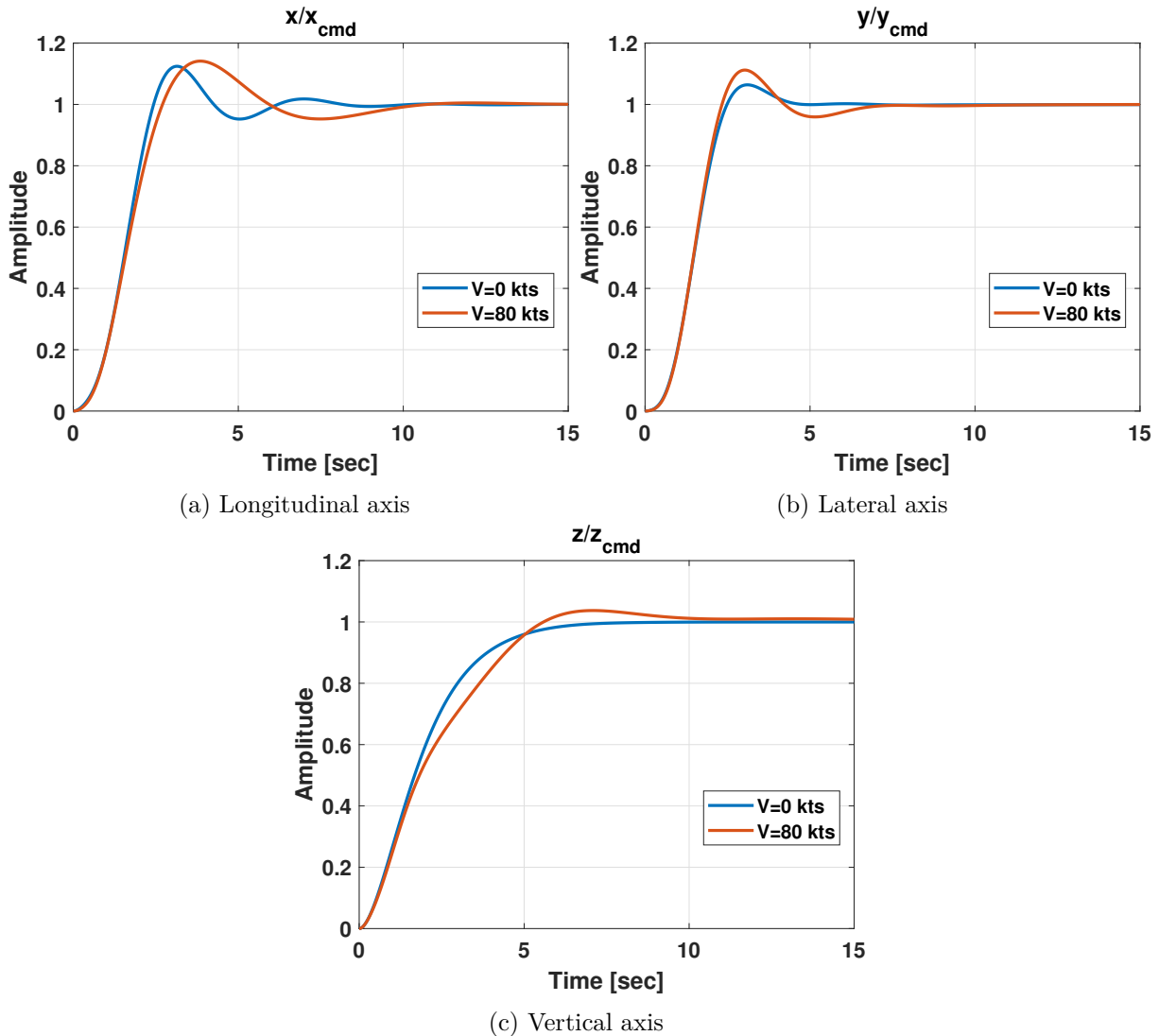


Figure 15.11: Step response at hover and forward flight at 80 kts

of this scale and being able to recover within the given, 1 m, spatial accuracy. As a result, gust rejection analysis during both vertical take-off and landing is conducted using an 8 m/s east-side gust with a 5 s period, representing the most challenging set of gust parameters.

Examining the figure, a gust period of $T = 1.5$ s induces the highest excitation in body rates especially roll, while a period of $T = 5$ s, likely too long for a realistic gust condition, results in the largest position displacement in lateral axis. We have demonstrated that our controller is already capable of rejecting all gust frequencies surveyed. However, since $T = 1.5$ s yielded the largest body rates, albeit momentarily, gust rejection analysis during both vertical take-off and landing is conducted using an 8 m/s east-side gust with a 1.5 s period.

The time histories in Figure 15.15 showing *Huma* gust rejection both during landing and take-off include rigid body Euler angles, swashplate inputs of the main and tail rotors, and the distance between the vehicle's center of gravity and the center point of the landing zone, along with the vertical take-off and landing trajectories with the gust applied. The roll axis is shown to be the most excited, as expected with a side gust. However, *Huma* is able to reject these disturbances and stabilize itself quickly due to the hingeless rotor. In doing so, *Huma* demonstrates superior spatial accuracy, minimizing drift and remaining within



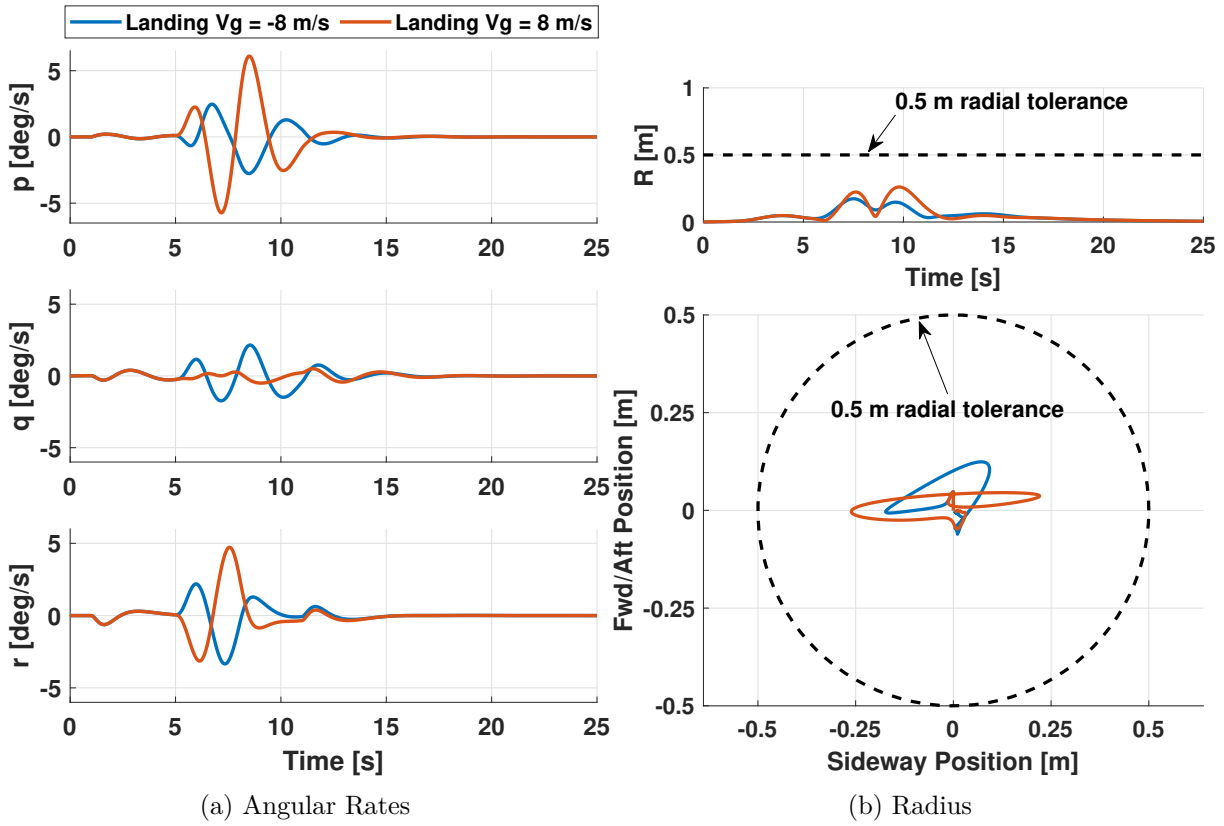


Figure 15.13: Landing with 8 m/s side gust with duration 3 sec

less than half of the permissible position tolerance of 1 meter as required by the mission specifications, while maintaining its take-off and landing trajectory as represented in Figure 15.15(d) in 3D. It also shows great command tracking despite the presence of gusts, as demonstrated in Figure 15.15(c). Thus, it is shown to be capable of resisting gust inputs, maintaining stability, and achieving spatial recovery.

Another task requirement involves testing the aircraft in adverse wind conditions within specified wind limits. It is important to note that all wind limits are defined in the inertial frame and then transformed to the body frame and the rotors' hub frames. Consequently, the simulation begins with a zero yaw angle, aligning the vehicle's heading directly north (i.e., the heading and inertial frame are aligned).

Figure 15.16 shows time simulations during a 10-meter (33 ft) vertical landing, incorporating the following adverse wind conditions: a headwind of 15 m/s (49 ft/s), a tailwind of 3 m/s (10 ft/s), and a crosswind of 8 m/s (26 ft/s) tested from both directions. Since it's shown that landing is more challenging than take-off in terms of gust rejection, this section only illustrates landing scenarios.

The impact of adverse wind conditions on the trim values is clearly reflected in the rigid body Euler angles and the swashplate angles of the main and tail rotors. These results demonstrate that headwinds, due to their large magnitude, are the most challenging for maintaining both aircraft attitude and position, showing the largest amount of drift and being the most demanding in terms of the controls required to reject them. Conversely, tailwinds are the easiest to reject. The results highlight *Huma*'s ability to maintain operation and controllability under harsh windy conditions from all different directions. The influence of different wind directions and magnitudes on the aircraft's performance parameters is evident, showcasing the robustness of the vehicle's control systems.

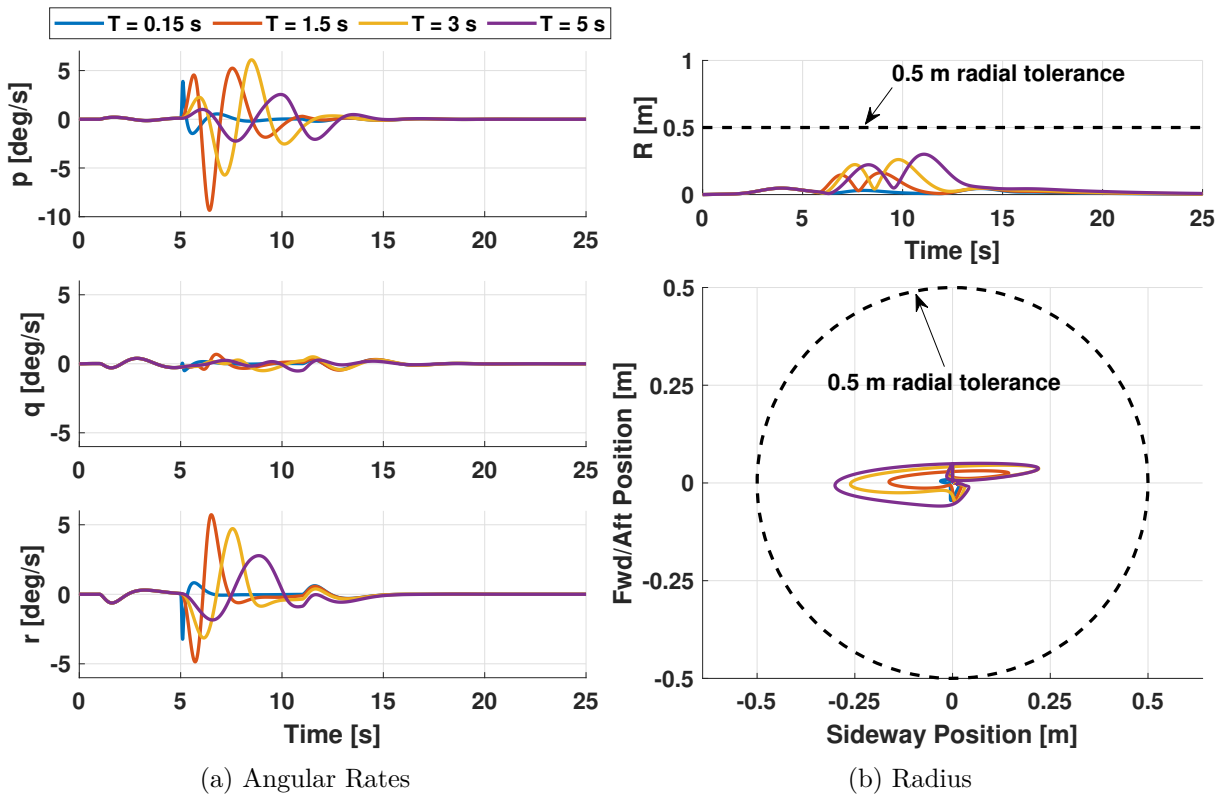


Figure 15.14: Landing with 8 m/s side gust with different gust lengths

16 Vehicle Performance

Huma was designed for superior performance during two distinct mission profiles: long endurance loiter and heavy supplies delivery. An excellent cruise efficiency in addition to a high payload capacity was the primary goal in *Huma*'s design.

16.1 Component Wise Drag Estimation

The overall drag of the vehicle is attributed to two primary factors: parasitic and wing-induced drag. We calculated the drag coefficients for each component using Computational Fluid Dynamics (CFD) simulations. For this purpose, we used our in-house solver -Mercury Framework- developed at the University of Maryland. The simulations were conducted at standard sea level atmospheric conditions at airspeed of 55 knots and 80 knots, representing long-endurance and supplies delivery missions. The wetted areas of all surfaces were accurately determined using CAD model. The resulting drag values for each component are given in Table 16.1. In line with Prouty's guidance, 10% increment was added to the calculated parasitic drag area to get a conservative estimate of the total drag. Miscellaneous drag of 5% was also added which includes drag from antennas, pitot probe and other fine structural details. The estimated parasitic drag area for the *Huma* for supplies delivery and long endurance mission comes out to be 1.31 ft² and 1.53 ft² respectively.



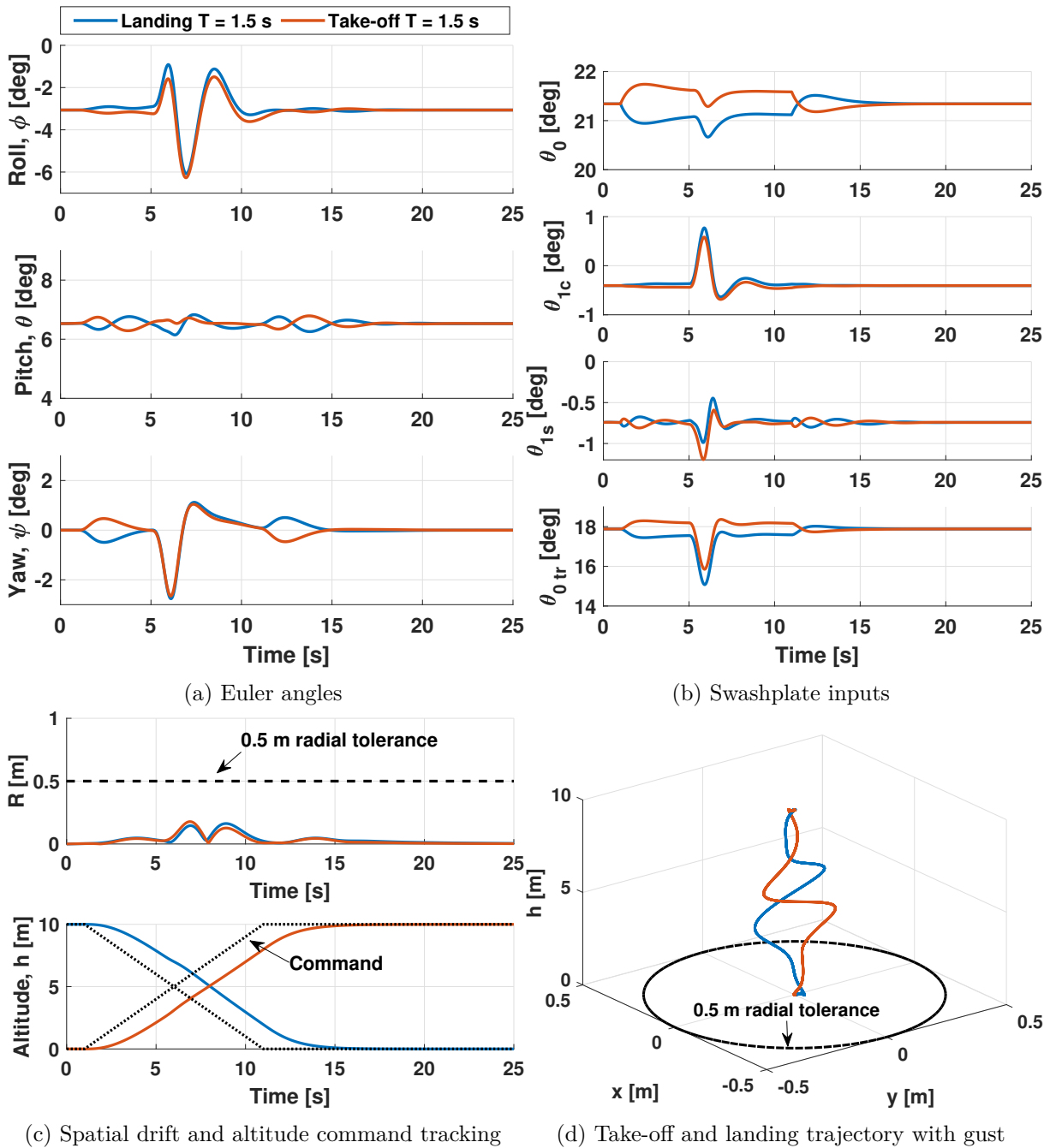


Figure 15.15: Gust Rejection during the take-off and landing phases with 8 m/s side gust

16.1.1 Fuselage

A baseline fuselage shape served as the starting point. Three-dimensional unstructured RANS analysis was conducted on this baseline design to ascertain the baseline drag coefficient and flat plate area. The CFD analysis of the baseline fuselage showed flow separation towards the aft fuselage, which led to high pressure drag (Figures 16.1(a) and 16.1(c)). The baseline design also depicted higher skin friction coefficients (Figure 16.1(c)). Modifications were made to accommodate payload, fuel tanks, transmission, engines, and other essential components, in addition to streamlining the fuselage design. Subsequent rounds of CFD analysis were then conducted on refined designs to assess their aerodynamic characteristics, ultimately resulting in



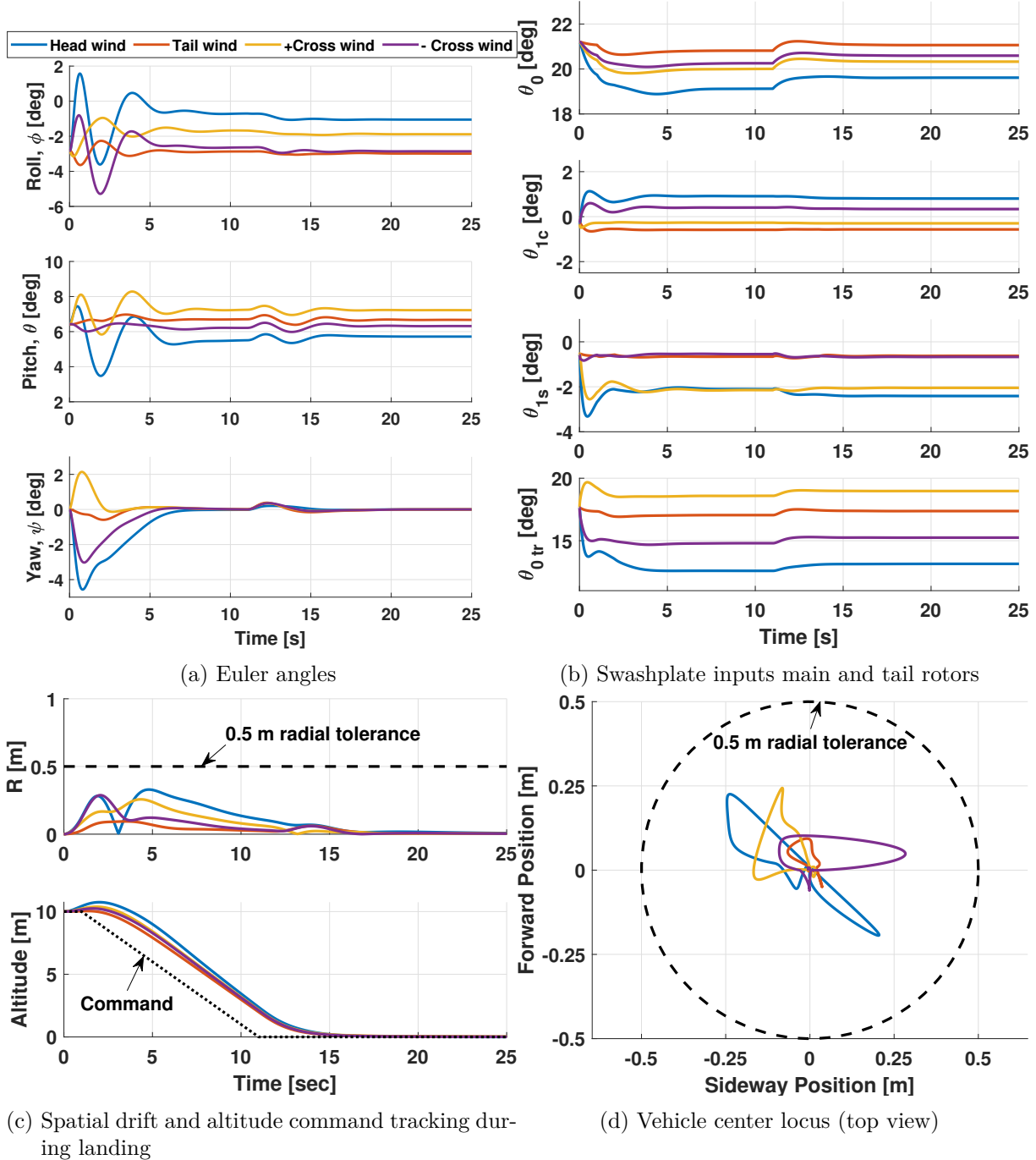


Figure 15.16: Landing with different wind limits and directions

the final refined fuselage.

CFD results of the redesigned fuselage show no flow separation, which is illustrated in Figure 16.2(a). The pressure difference between the upper and lower surfaces of the fuselage causes the airflow to move from the lower to the upper surface, keeping the flow attached to the lower surface (Figures 16.2(a) and 16.2(b)).

The comparison between the baseline fuselage and the redesigned fuselage reveals significant improvements in terms of drag. The final design exhibits relatively lower skin friction (Figures 16.1(c) and 16.2(c)). The adverse pressure gradient at the upper and lower sweeps after mid-fuselage is not high enough to cause



flow separation, ensuring the airflow remains attached and thus mitigating pressure drag (Figures 16.1(b) and 16.2(b)).

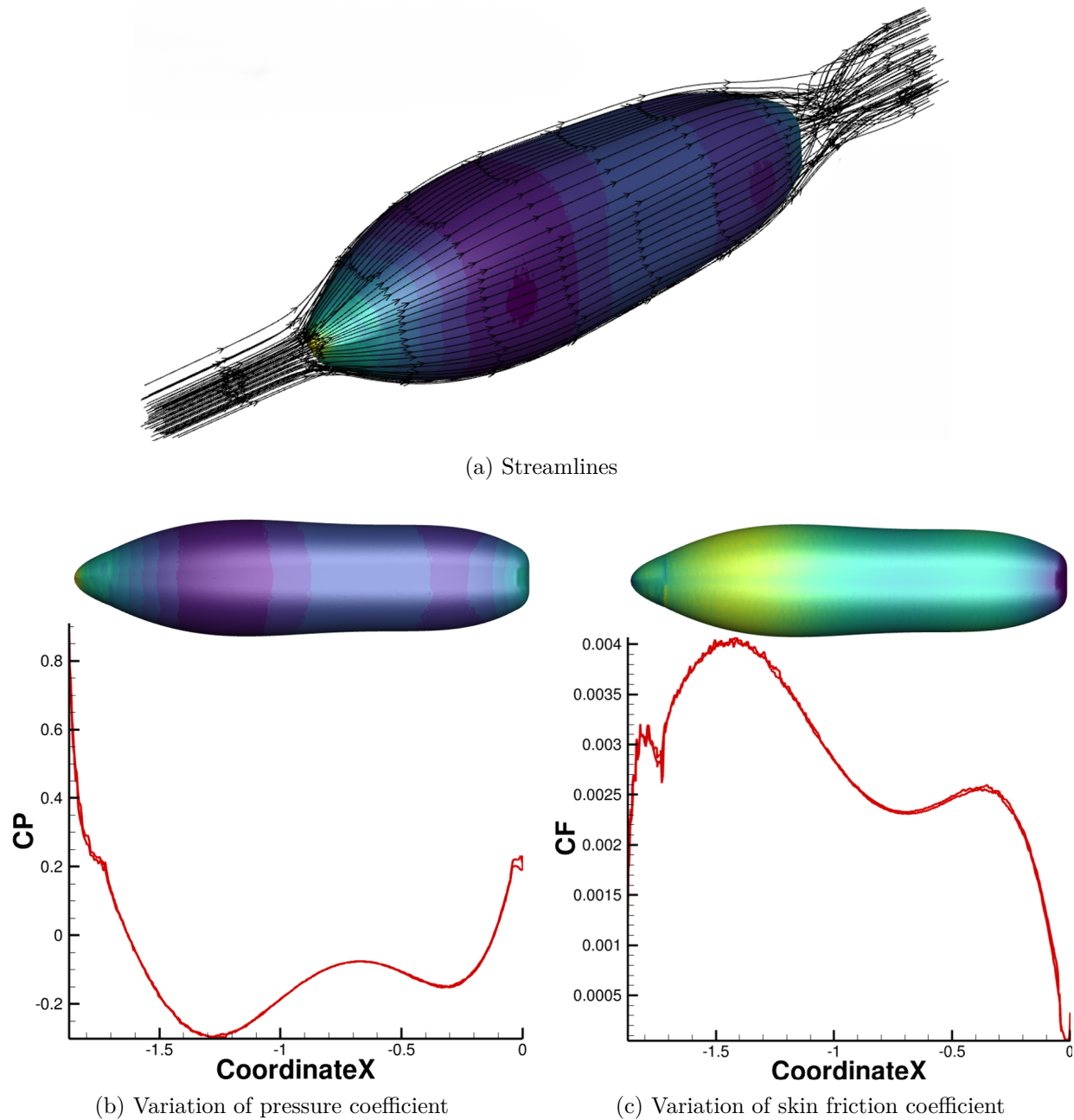


Figure 16.1: Streamlines, pressure, and skin friction along centre line (80 knots)

16.1.2 Hub Fairing

The rotor hubs are known for their significant contribution to the overall drag of the rotorcraft. To mitigate this major drag, the rotor hub was enclosed in a fairing designed to smooth the airflow around it. CFD simulations, as shown in Figure 16.3(b), were performed to estimate its drag. The resulting lower values of drag coefficient and flat plate area indicate an efficient aerodynamic design.

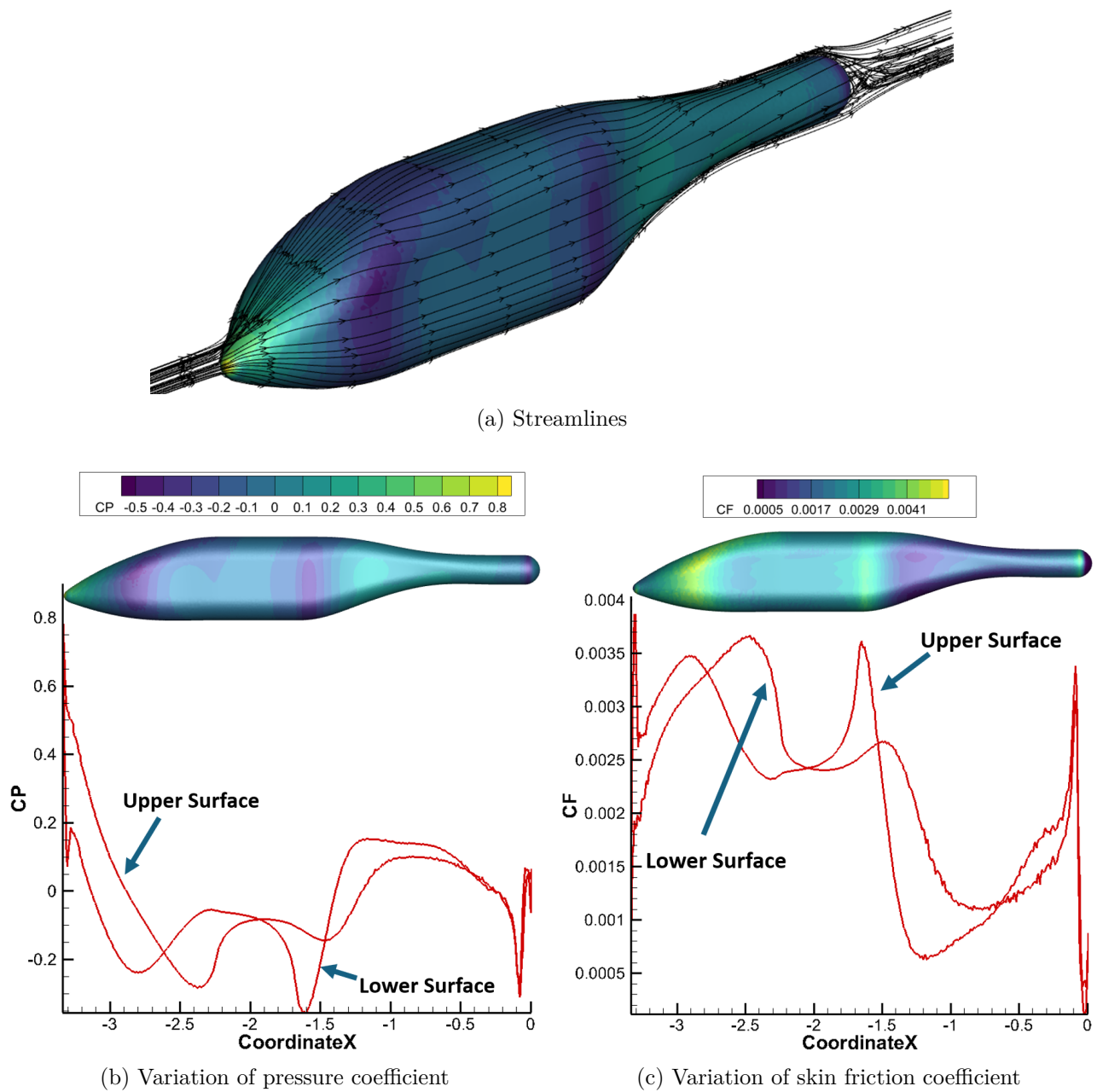


Figure 16.2: Streamlines, pressure, skin friction of re-designed fuselage (80 knots)

16.1.3 Wing and Empennage

The drag of the wing and empennage was estimated by utilizing the wetted surface area and high-fidelity data of the airfoils employed on these surfaces. Specifically, the FX 63-137 airfoil was used for the wing, while the NACA4415 airfoil was used for both the horizontal and vertical fins. The Oswald efficiency factors and aspect ratio were used to account for three-dimensional effects. The final drag coefficients and flat plate area indicated an efficient wing and empennage designs.

16.1.4 Landing Gear

Flow simulations were also conducted to estimate the drag on the landing gears. The analysis, as shown in Figure 16.3(a), revealed no flow separation around the landing gears. The landing gears incorporate an elliptical cross-section with a sleek design to minimize resistance so presents lower skin friction drag and ensures streamlined airflow around the gear.

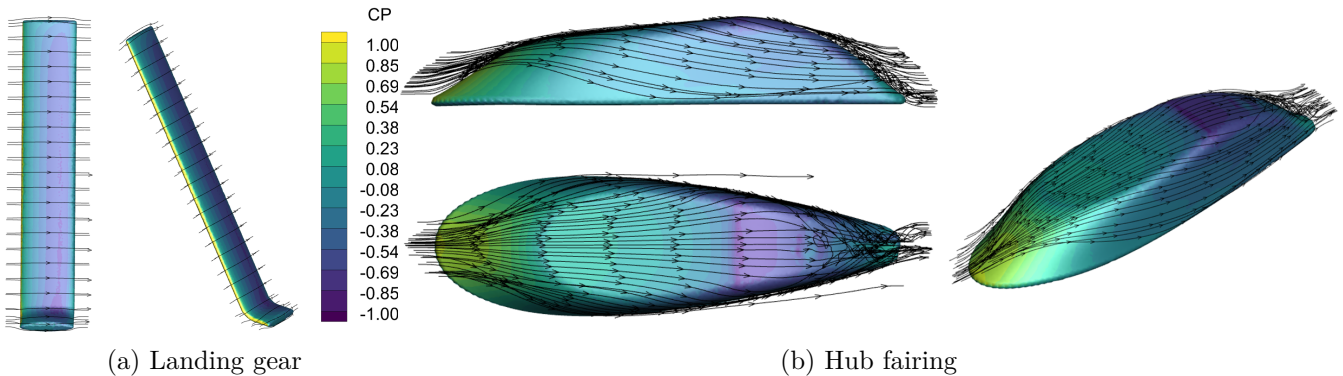


Figure 16.3: CFD of landing gear and hub fairing (80 knots)

Table 16.1: Component-wise drag and flat plate area

Component	Coefficient of Drag		Flat Plate Area			
	Supplies	Loiter	Supplies		Loiter	
			m ²	ft ²	m ²	ft ²
Fuselage	0.0240	0.0223	0.0984	1.0590	0.0915	0.9849
Wing	-	0.0210	-	-	0.0263	0.2826
Horizontal Tail	0.0191	0.0182	0.0013	0.0144	0.0013	0.0137
Vertical Fin	0.0191	0.0096	0.0021	0.0226	0.0011	0.0113
Landing Gear	0.0065	0.0057	0.0010	0.0105	0.0009	0.0092
Hub	0.0217	0.0200	0.0031	0.0336	0.0029	0.0309
Interference (10%)	0.0090	0.0097	0.0106	0.1140	0.0124	0.1333
Miscellaneous (5%)	0.0045	0.0048	0.0053	0.0570	0.0062	0.0666
Total	0.1039	0.1111	0.1218	1.3112	0.1424	1.5324

16.2 Hover Download

Rotor wash is common, especially in lift compound designs. In hover, the rotor needs to produce sufficient thrust to lift gross takeoff weight and overcome the extra downforce imposed by rotor wake on fuselage and wing. These download effects were estimated by integrating the local drag coefficient and sectional width. The download was estimated to be 5% of gross takeoff weight for the single main rotor configuration and 12% for the lift compound configuration. These estimates were more conservative than measured values at hover tests.

16.3 Airframe Aerodynamic Metrics

The airframe equivalent areas for two mission segments are presented in Table 16.2, encompassing only the fuselage and rotor hub as specified in the RFP. The lift area is relatively small due to the non-lifting nature of the fuselage and hub, which exhibit very low lift coefficients. In contrast, the drag area is within the expected parameters. The pitching moment volume is relatively high, resulting in a nose-down pitching moment. The horizontal fin has been designed to offset this moment.

Table 16.2: Aerodynamic Metrics

Metrics	Supplies		Loiter	
	m^2	ft^2	m^2	ft^2
Lift area (L/q)	-0.0076	-0.0815	-0.0066	-0.0706
Drag area (D/q)	0.1015	1.0926	0.0944	1.0158
Pitching moment volume (M/q)	m^3	ft^3	m^3	ft^3
	-0.4872	-17.2040	-0.4349	-15.3580

16.4 Hover Performance

Huma is primarily designed for high-efficiency cruise flight. The large diameter edgewise rotor also enables low-power hover out of ground effect (HOGE).

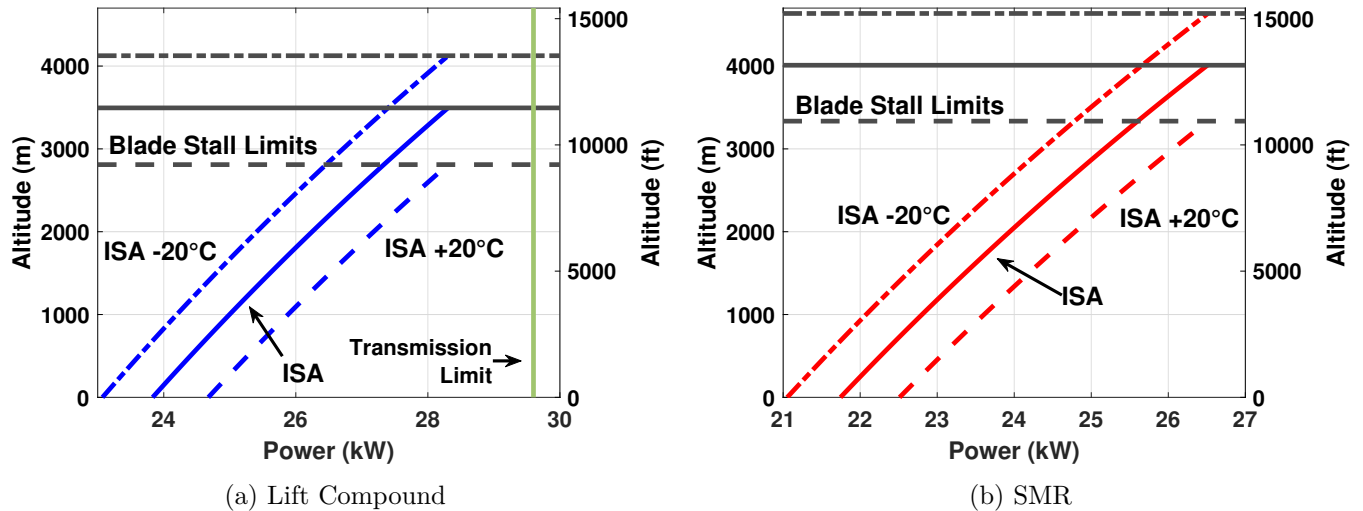


Figure 16.4: HOGE power versus altitude at the designed GTOW (160 kg)

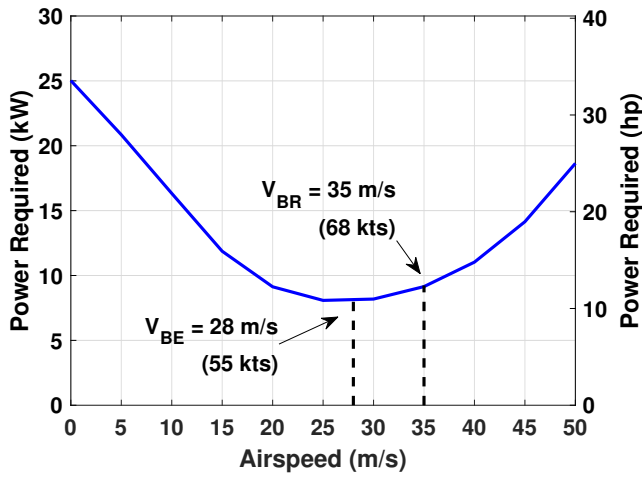
Huma is a modular vehicle and can be outfitted with equipment to complete non-RFP missions which may include hot and high hover. The installed engine is capable of 36.8 kW (50 hp), well above the hover power at sea level, enabling hot and high hovering capabilities as shown in Figure 16.4. The power required increases with altitude and temperature. The HOGE hover ceiling is limited by blade stall, defined by $C_T/\sigma = 0.16$ according to the McHugh stall boundary [11], not by the 31 kW (42 hp) transmission limit or by engine power. The power required to hover is greater for the lift compound due to hover download, hence the maximum hover altitude for the lift compound configuration is 2810 m (9219 ft) whereas the maximum hover altitude for the SMR configuration is 3335 m (10942 ft) at ISA+20°C conditions and

maximum GTOW (MGTOW). For ISA conditions and MGTOW, the two configurations are capable of hovering as high as 3495 m (11467 ft) and 4010 m (13156 ft) respectively.

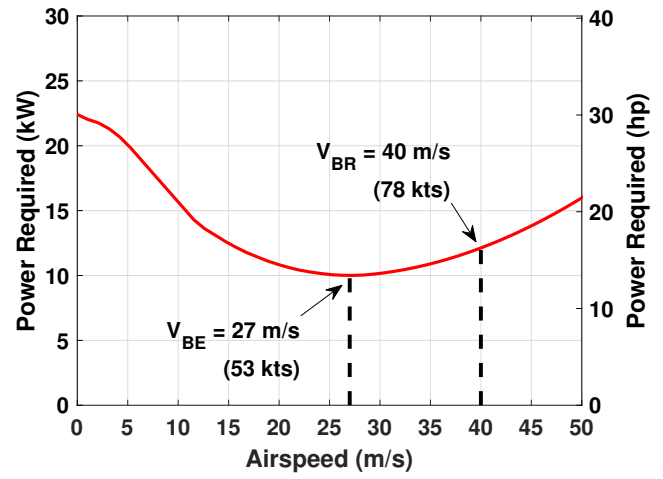
16.5 Forward Flight Performance

The long endurance loiter mission segment and 1.25-hour time constraint on the 185 km (100 nm) outbound cruise leg made cruise efficiency extremely important. *Huma*'s rotor, wing, fuselage, and landing gear were designed to produce minimal drag for superior cruise performance.

The forward flight performance was determined for *Huma* at the design gross takeoff weight of 160 kg (352 lb). Figure 16.5 shows the variation of power required with forward speed at the 500 m (1640 ft) cruise altitude for both vehicle configurations. *Huma* operates at the velocity for best endurance (V_{BE}) during loiter and the velocity for best range (V_{BR}) during the return cruise segment to maximize mission performance.



(a) Lift Compound



(b) SMR

Figure 16.5: Cruise power versus velocity at the designed GTOW (160 kg)

Lift to drag ratio, shown against velocity in Figure 16.6 at the 500 m (1640 ft) cruise altitude, is a useful metric to compare the relative effectiveness of *Huma*'s configurations for each mission. The lift compound configuration is designed for high-efficiency loiter, therefore the peak lift-to-drag ratio occurs near its 28 m/s (55 knots) V_{BE} . At higher speeds, the vehicle body pitch tilts forward due to a greater wing lift share. The wing operates far from its peak L/D angle of attack and the fuselage flat plate drag increases, quickly decreasing L/D. In contrast, the SMR configuration spends the majority of its flight time in the cruise segment favoring a higher V_{BR} . The SMR configuration does not face the same drag limitations in higher-speed flight and is a better solution to the supplies delivery mission which is dominated by higher speed

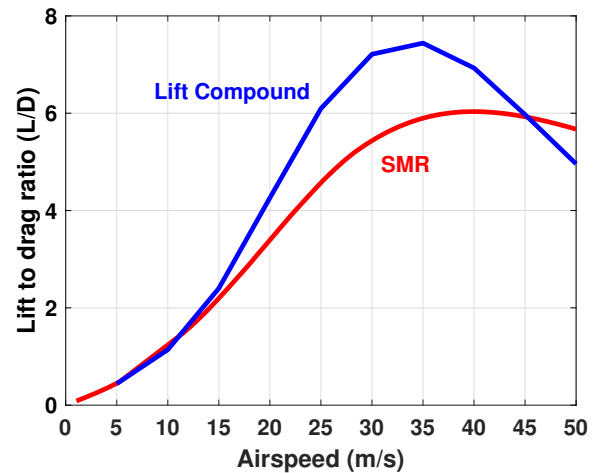


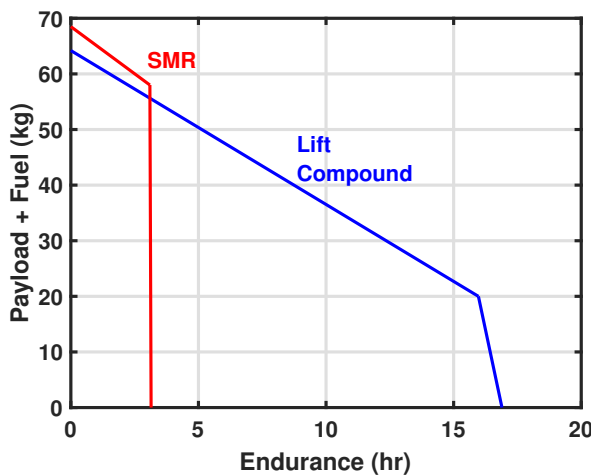
Figure 16.6: Lift to drag ratio at various airspeeds and vehicle configurations



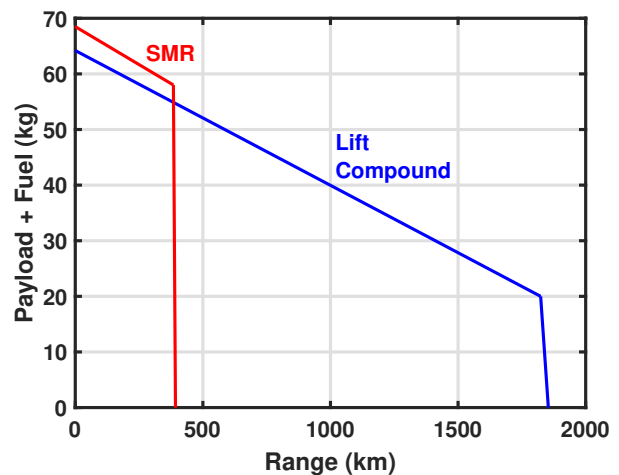
cruise segments.

16.6 Range and Endurance

Payload-range and payload-endurance curves trade fuel and payload for range or endurance. *Huma*'s excellent endurance capability is seen in Figure 16.7(a). A maximum loiter time of 16 hours is achieved at 500 m (1640 ft) for the lift compounded configuration while carrying the 20 kg (44 lb) payload. Exceptional multi-mission performance is evident as the SMR configuration can carry an additional 7% payload/fuel for a shorter mission. The SMR benefits from decreased empty weight fraction, and therefore carries a greater maximum payload. Figure 16.7(b) shows the long distance covered by *Huma* during an efficient cruise. A maximum cruise range of 1824 km (1133 nm) can be swapped out with greater payload capacity for the heavy-lift supplies mission.



(a) Payload vs Endurance for cruise at 160 kg



(b) Payload vs Range for cruise at 160 kg

Figure 16.7: Payload-range and payload-endurance diagrams

16.7 Mission-specific Performance

Mission-specific performance is outlined in Table 16.3 for the long endurance mission and Table 16.4 for the supplies delivery mission. The loiter mission segments operate at V_{BE} and the cruise segments operate at V_{BR} when not limited by the 41.1 m/s (80 knots) minimum speed. Both velocities decrease with vehicle weight as fuel is burned and the payload is offloaded throughout the missions. The listed aerodynamic power includes shaft power required for the main rotor and tail rotor. Total power includes additional payload and accessory power requirements in addition to consistent 5% engine installation losses and 3% transmission losses. The engine SFC increases with power reduction from the engine's 36.8 (50 hp) designed power, as detailed in Section 11.2.

17 Safety Considerations

17.1 Engine and Powerplant

The likelihood of turbine engine failure is very low. In this scenario, the safe termination of flight must be ensured. The single main rotor configuration is highly regarded for its safety record due to its autorotation



Table 16.3: Long endurance (lift compound) mission-specific performance data

Mission Segment	Weight at Segment Start kg (lb)	Aerodynamic Power kW (hp)	Total Power kW (hp)	Powerplant Efficiency, SFC kg/kW-hr (lb/hp-hr)	Transmission Efficiency
1	160 (352.7)	3.02 (4.05)	4.11 (5.51)	0.43 (0.70)	0.97
2	159.9 (352.4)	22.96 (30.79)	25.68 (34.44)	0.27 (0.44)	0.97
3	159.8 (352.3)	10.06 (13.49)	11.72 (15.72)	0.33 (0.54)	0.97
4	159.6 (351.8)	10.14 (13.60)	11.81 (15.84)	0.33 (0.54)	0.97
5	155.0 (341.6)	6.47 (8.68)	7.84 (10.52)	0.36 (0.60)	0.97
6	119.8 (264.0)	6.02 (8.07)	7.35 (9.86)	0.37 (0.61)	0.97
7	116.0 (255.7)	4.97 (6.67)	6.22 (8.34)	0.38 (0.63)	0.97
8	115.8 (255.3)	13.43 (18.01)	15.37 (20.61)	0.31 (0.50)	0.97

Table 16.4: Supplies delivery (SMR) mission-specific performance data

Mission Segment	Weight at Segment Start kg (lb)	Aerodynamic Power kW (hp)	Total Power kW (hp)	Powerplant Efficiency, SFC kg/kW-hr (lb/hp-hr)	Transmission Efficiency
1	160 (352.7)	2.98 (4.00)	3.64 (4.89)	0.44 (0.73)	0.97
2	159.9 (352.5)	20.22 (27.13)	22.30 (29.90)	0.28 (0.46)	0.97
3	159.8 (352.3)	13.10 (17.57)	14.59 (19.57)	0.31 (0.51)	0.97
4	159.5 (351.7)	11.10 (14.88)	12.43 (16.66)	0.32 (0.53)	0.97
5	154.8 (341.2)	8.49 (11.38)	9.60 (12.88)	0.34 (0.57)	0.97
6	153.7 (338.9)	6.04 (8.10)	6.95 (9.32)	0.37 (0.61)	0.97
7	153.6 (338.5)	17.94 (24.06)	19.83 (26.59)	0.29 (0.47)	0.97
8	95.5 (210.5)	9.42 (12.63)	10.61 (14.22)	0.34 (0.55)	0.97
9	95.5 (210.5)	7.83 (10.50)	8.89 (11.92)	0.35 (0.58)	0.97
10	95.3 (210.1)	6.81 (9.13)	7.78 (10.44)	0.36 (0.60)	0.97
11	91.7 (202.1)	3.18 (4.27)	3.87 (5.18)	0.43 (0.71)	0.97
12	91.6 (201.9)	8.19 (10.98)	9.28 (12.44)	0.35 (0.57)	0.97

performance. *Huma* can automatically estimate its flight state with onboard HUMS sensors and perform an autorotation if needed. Onboard sensor data such as gas turbine and power turbine RPM, rotor RPM, oil pressure, and fuel flow are monitored to predict failure without delay. High bandwidth actuators allow a rapid collective drop to maintain high rotor RPM when autorotation is necessary. Human reaction time is not a factor due to the automatic flight control system. Additionally, the wings for the lift compounded configuration can extend the collective-reduction window due to lift-sharing.

17.2 Avionics and Electrical

The avionics and electrical systems were designed with redundancy to avoid any single point of failure.

17.2.1 Processing Component Failures

Huma can maintain basic control in the event of a malfunction with the main flight computer, as the control loops and state estimation filters run on the flight controllers. Required position, velocity, and attitude estimates can be obtained using the IMUs, barometers, airspeed sensor, and GNSS, which are all



connected directly to the flight controllers. Additionally, as the ADS-B In receiver is incorporated into the flight controller board, the vehicle can avoid collisions with larger aircraft equipped with ADS-B Out even without camera or radar data.

A triple-redundant configuration is used for the flight controllers themselves. Control commands and state estimates are checked for consistency with all three controllers; this allows a failure on one controller to be identified by comparison to the other two.

17.2.2 Sensor Failures

The use of redundant avionics sensors ensures that *Huma* can continue operating safely even in the event of an individual sensor failure. As described in Section 13.2, both state estimation and high-level tasks are performed using a combination of multiple redundant sensors.

17.2.3 Alternator Failure

As discussed in Section 13.6, in the event of alternator failure, the battery can power critical avionics components and actuators for 34 minutes. This provides the aircraft with time to conduct an emergency landing. Also, the starter/generator on the UTP50R turboshaft can be used as a backup alternator in case of primary alternator malfunction.

17.3 Additional Safety Features

Huma is equipped with a Health and Usage Monitoring System (HUMS), described in Section 13.5. The HUMS can warn operators of potential component or system failures, allowing corrective action to be taken.

18 Acoustics

Since the main objective of *Huma* is to operate from a ship deck and land in a disaster zone near people, it is important to keep noise levels low, especially during hover. The main sources of noise for this type of aircraft are tonal noise and broadband noise. Tonal noise primarily comes from the interaction of the blade with airflow and unsteady aerodynamic loads. Broadband noise mainly comes from the interaction of the airfoil with its boundary layer and near wake.

Huma's noise levels were analyzed using ACUM (Acoustic Code of the University of Maryland). The code calculates tonal noise based on Farassat's formulation of the Ffowcs Williams-Hawkins equation [79] [80] and broadband noise using the Brooks-Pope-Marcolini (BPM) method [81]. The sectional aerodynamic data for the main rotor blade and other information were provided to the code to calculate tonal and broadband noise at 700 specific observer locations. These locations were set in a hemisphere below the aircraft at a radius of 20 meters. The results are shown in Figure 18.1. A-weighted noise levels, measured in dB(A), is more insightful since this scale adjusts sound measurements to reflect human ear sensitivity, which varies across frequencies. This weighting emphasizes mid-range frequencies (1-6 kHz) where hearing is most sensitive compared to very low and high frequencies.

The analysis revealed that broadband noise is much higher than tonal noise, making the total noise similar to the broadband noise. For instance, tonal noise is much lower directly below the aircraft, with a maximum of 71 dB(A) at the horizontal plane. In contrast, the broadband noise is higher directly below the aircraft, reaching a maximum of 66.54 dB(A). Therefore, the total overall sound pressure level matches the



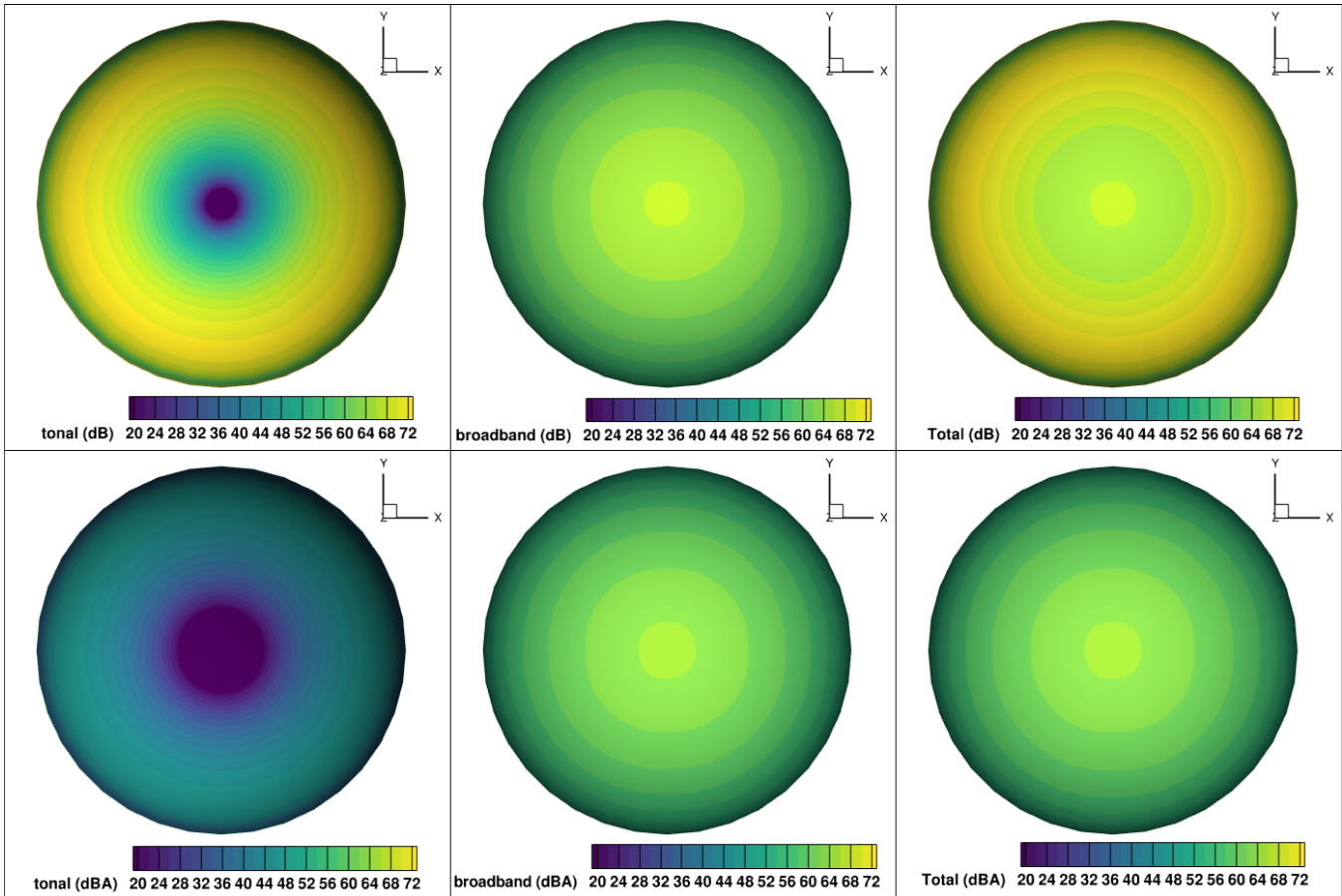


Figure 18.1: Overall sound pressure level during hover

broadband noise due to the negligible tonal noise below the aircraft. The total sound pressure levels are well below the acceptable limit of 78.5 dB(A), indicating that *Huma* is an eco-friendly aircraft with low noise levels.

19 Cost Analysis

Cost estimates were generated using the Harris-Scully cost model, as provided in the NDARC manual [9]. The model predicts the purchase price within 20% error for 96% of the 128 rotorcraft analyzed.

19.1 Purchase Price

The purchase price of the aircraft can be estimated using a statistical model, which is based on the purchase prices of existing commercial and military rotorcraft [82]. The model includes adjustments for various factors, including empty weight, engine type, landing gear, and number of main rotors. The calculated price also accounts for the known costs of the specialized avionics and electrical components. Using this model, the aircraft purchase price is estimated to be 187,000 USD.

19.2 Maintenance Cost

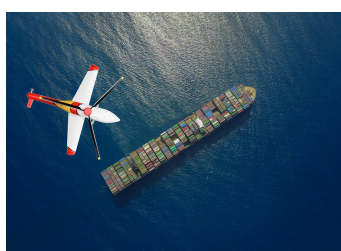
The Harris-Scully model estimates the maintenance cost of the aircraft, which includes parts and labor costs. The maintenance cost is estimated to be 63 USD per flight hour, with a predicted 0.10 maintenance man hours per flight hour.

19.3 Operational Cost

The operational cost can be estimated using a statistical relationship with aircraft purchase price [83], as well as the estimated fuel and maintenance costs. The operational cost was calculated assuming one mission is flown per day, with the additional assumption that half of these are long-endurance missions and the other half are supplies-delivery missions. With this, the estimated operational cost is 580,000 USD per year, or 205 USD per flight hour. Estimated crew, insurance, depreciation, and finance costs, amounting to 380,000 USD, account for approximately two-thirds of the operational cost.

20 Additional Mission Capabilities

Huma is capable of completing two distinct missions for disaster relief as outlined in the RFP. However, it can also be used in a number of other applications. Such applications provide value even when *Huma* is not needed at the site of a disaster.



(a) Maritime surveillance and reconnaissance.



(b) Agricultural monitoring.



(c) Medical deliveries.

Figure 20.1: Examples of additional applications.

20.1 Short-Range Deliveries

In its supplies-delivery configuration, *Huma* can be used to transport many different payloads. It is able to provide up to 400 W of bus power to its payload, opening up possibilities for specialized and sensitive cargo. One potential application is medical supplies or organ delivery; its range is adequate to reach regional medical sites and it is able to power necessary refrigeration equipment on-board. Another application is war zone supply deliveries.

20.2 Monitoring and Surveillance

With its onboard camera equipment and high potential loiter time in its long-endurance configuration, *Huma* is capable of performing missions involving aerial monitoring. Using its downward-facing cameras and thermal cameras, it can autonomously conduct long-range reconnaissance missions in maritime envi-

ronments. It can also be used in applications such as law enforcement, traffic monitoring, terrain mapping, and agricultural monitoring.

20.3 Additional Modular Equipment

With its modular payload bay, *Huma* can be equipped with customized modular components beyond those developed for the disaster relief missions. Potential additional components could include specialized sensing and surveying equipment. For agricultural applications, crop dusting or seeding equipment could be mounted inside the payload bay.

21 Summary

The University of Maryland Graduate Design Team designed *Huma*, a 160 kg (353 lb) modular UAS to assist with disaster relief efforts. With the ability to be reconfigured into either an SMR configuration with high payload capacity or a lift-compound configuration optimized for long endurance, *Huma* can exceed the requirements of both missions specified in the RFP. All portions of the design were developed with the unique challenges of a maritime and shipboard environment in mind.

1. The hingeless main rotor hub design provides high control authority and gust tolerance. The blade geometry was optimized with a genetic algorithm to obtain high performance across all mission segments.
2. The tail rotor retains control authority in up to an 8.8 m/s (17 knots) crosswind, allowing safe operation in high winds and gusts.
3. The modular payload bay allows for rapid attachment and removal of modular components, including wings, a secondary fuel tank, and a payload case. This allows the aircraft to be reconfigured as needed to efficiently perform different missions.
4. In the lift-compound configuration, the wings decrease loiter power and fuel consumption, allowing for up to a 13-hour loiter duration, a 30% increase over RFP requirements. Rotor speed reduction minimizes profile drag.
5. In the SMR configuration, the low empty weight allows for a high, 58 kg (128 lb), payload capacity exceeding RFP requirements by 16%.
6. The avionics hardware incorporates redundant sensors and provides full awareness of both the aircraft state and its surroundings. With advanced computer vision and trajectory planning algorithms, *Huma* can operate fully autonomously across all mission segments.
7. The belt-driven transmission eliminates gearbox housings, stages, and lubrication systems, reducing weight, maintenance, and cost.



References

- [1] Omer, S., "2023 Turkey and Syria earthquake: Facts, FAQs, how to help," <https://www.worldvision.org/disaster-relief-news-stories/2023-turkey-and-syria-earthquake-faqs>, Jan. 2024.
- [2] United Nations, "Türkiye-Syria Earthquake Response," <https://www.un.org/en/turkiye-syria-earthquake-response>.
- [3] Butt, R., "After devastating floods in Pakistan, some have recovered but many are struggling a year later," <https://apnews.com/article/pakistan-flood-anniversary-ebd91932d0452d47c3b0c4bd2a656f38>, Jun. 2023.
- [4] Saaty, R., "The Analytic Hierarchy Process—What It is and How It is Used," *Mathematical Modelling*, Vol. 9, No. 3-5, 1987, pp. 161–176.
- [5] Pugh, S., *Total Design: Integrated Methods for Successful Product*, Cambridge University Press, 1st ed., 1991.
- [6] Uppoor, V., Patil, M., and Chopra, I., "Aeromechanics Investigation of Dual-Wing Lift Compounded Slowed Mach-scaled Rotor," *80th Vertical Flight Society Annual Forum*, Montréal, Québec, Canada, May 7-9, 2024.
- [7] Maurya, S. K., Chopra, I., and Datta, A., "Steady and Unsteady Hover Test of a Lift Compounding Rotorcraft," *AIAA SciTech 2022 Forum*, San Diego, CA, Jan. 3–7, 2022.
- [8] Maurya, S., Chopra, I., and Datta, A., "In Search of Extreme Limits of a Compound Helicopter in High Speed Flight," *Proceedings of the Vertical Flight Society International 77th Annual Forum & Technology Display*, May 2021.
- [9] Johnson, W., "NDARC: NASA Design and Analysis of Rotorcraft," NASA-TP 20220000355, Mar. 2023.
- [10] Raymer, D. P., *Aircraft Design: A Conceptual Approach*, AIAA Education Series, AIAA, 3rd ed., 1999.
- [11] Yeo, H. and Johnson, W., "Prediction of Maximum Lift Capability of Helicopter Rotors," *Journal of Aircraft*, Vol. 52, No. 1, May 2014, pp. 1–9.
- [12] Datta, A., Yeo, H., and Norman, T., "Experimental Investigation and Fundamental Understanding of a Slowed UH-60A Rotor at High Advance Ratios," *67th American Helicopter Society Society Annual Forum*, Virginia Beach, Virginia, May 3–5, 2011.
- [13] Johnson, W., *Rotorcraft Aeromechanics*, Cambridge University Press, 2013.
- [14] Stäubli, "Quick Coupling SPT Fuel Line Connections," 2021.
- [15] Anand, A., Marepally, K., Safdar, M. M., Lee, B., and Baeder, J. D., "Generalizable Deep Learning Module for Rotorcraft Inverse Design Applications," *AIAA 2024-0460, Session: Special Session: Applied Surrogate Modeling III*, Jan 2024, Published Online: 4 Jan 2024.
- [16] Safdar, M. M., Anand, A., Marepally, K., Lee, B., and Baeder, J. D., "A Surrogate Modeling Framework for Airfoil Design and Optimization," *AIAA 2024-0458, Session: Reduced Order Aerodynamic Modeling & System Identification II*, Jan 2024, Published Online: 4 Jan 2024.
- [17] Office of the Federal Register, "Part 25.581 Lightning Protection," <https://www.ecfr.gov/current/title-14/chapter-I/subchapter-C/part-25/subpart-C/subject-group-ECFR6fd6a843ee94737/section-25.581>, April 8 1970.
- [18] Welsh, W. A., Weiner, S. D., and Blackwell Jr., R. H., "Active Vibration Control of a Rotorcraft,"



- U.S. Patent 10443675B2, Oct. 2019.
- [19] Uppoor, V., Patil, M., and Chopra, I., "Wind Tunnel Testing of a Slowed Mach-scaled Hingeless Rotor with Lift and Thrust Compounding," *Vertical Flight Society's 6th Decennial Aeromechanics Specialists' Conference*, Feb. 2024.
- [20] Hohenemser, K. H., "Hingeless Rotor Flight Dynamics," Advisory Group for Aerospace Research and Development, North Atlantic Treaty Organization AGARD-AG-197, Sep. 1974.
- [21] Patil, M. and Datta, A., "A Scalable Time-Parallel Solution of Periodic Rotor Dynamics in X3D," *Journal of the American Helicopter Society*, Vol. 66, No. 4, October 2021, pp. 1–16.
- [22] Baker, G. R. and Thompson, C. M., "The Effect of Seawater on Polymers," NRL Memorandum Report 4097, Nov 1979.
- [23] Nord-Lock Group, "Nord-Lock Original Washers," <https://www.nord-lock.com/nord-lock/products/washers/>, 2024.
- [24] Falls, J., Datta, A., and Chopra, I., "Integrated Trailing-Edge Flaps and Servotabs for Helicopter Primary Control," *Journal of the American Helicopter Society*, Vol. 55, No. 3, 2007.
- [25] Mcgeer, B. T. and Von Flotow, A. H., "Variable-twist rotor blade controlled by hub pitch angle and rotational speed," U.S. Patent 7857598B2, Dec. 2010.
- [26] Wiens, T. and Deibert, B., "A Low-Cost Miniature Electrohydrostatic Actuator System," *Actuators*, Vol. 9, No. 4, 2020.
- [27] Zakir, J., Quraishi, M. H., Zia, U., and Safdar, M. M., "Investigation of High Angle of Attack Characteristics of Blended Wing Body Configurations," *AIAA Scitech Forum 2024*, January 2024.
- [28] Naval Air Systems Command, "Structural Design Requirements (Helicopters)," Department of the Navy AR-56, 17 Feb. 1970.
- [29] Tsai, S. W. and Wu, E. M., "A General Theory of Strength for Anisotropic Materials," Technical Report AFML-TR-71-12, August 1972.
- [30] Scanlan, R. H. and Rosenbaum, R., *Introduction to the Study of Aircraft Vibration and Flutter*, Macmillan, 1951.
- [31] Gudmundsson, S., *General Aviation Aircraft Design: Applied Methods and Procedures*, Butterworth-Heinemann, 2022.
- [32] White, W., "Unanticipated Right Yaw in Helicopters," FAA Advisory Circular AC 90-95, Dec. 1995.
- [33] National Transportation Safety Board, "Loss of Tail Rotor Effectiveness in Helicopters," NTSB Safety Alert SA-062, Mar. 2017.
- [34] Prouty, R. W., *Military Helicopter Design Technology*, Krieger Publishing Company, 1998.
- [35] Weisner, W. and Kohler, G., "Tail Rotor Performance in Presence of Main Rotor, Ground, and Winds," *Journal of the American Helicopter Society*, Vol. 19, No. 3, July 1974, pp. 2–9.
- [36] Robinson Helicopter Company, "Robinson R22 Illustrated Parts Catalog," Robinson catalog, May 2021.
- [37] Wiesner, W., "Tail Rotor Design Guide," Boeing Vertol Company. Prepared for the Army Air Mobility Research and Development Laboratory AD-775391, Jan 1974.
- [38] ASTM-International, "B117-19 Standard Practice for Operating Salt Spray (Fog) Apparatus," Tech. rep., 2019.
- [39] Roberge, P., *Handbook of Corrosion Engineering*, McGraw-Hill handbooks, McGraw-Hill, 2000.
- [40] Prasad, N., Gokhale, A., and Wanhill, R., *Aluminum-Lithium Alloys: Processing, Properties, and*



- Applications*, Elsevier Science, 2013.
- [41] Bamsey, I., "UAV Turbines UTP50R 50 hp recuperated gas turbine," <https://www.uavturbines.com/wp-content/uploads/2017/02/UAV-Dossier.pdf>, Jan. 2017.
- [42] Hirth Engines, "Engine 3503 Basic Data," October 2021.
- [43] Hirth Engines, "42 Engines Series Metric," 2021.
- [44] Zoche, M., "Zoche Aero-Diesels," April 2007.
- [45] LiquidPiston, "XTS-210," 2022.
- [46] Launchpoint Electric Propulsion Solutions, "40 kW Hybrid Power System," 2022.
- [47] FusionFlight, "ARC Specification Sheet," April 19 2024.
- [48] Mills, B. T., *Fabrication and Fundamental Studies of a 4-kW, Variable-Voltage, Distributed Hybrid-Electric Powertrain for eVTOL Aircraft*, Ph.D. thesis, University of Maryland, College Park, 2022.
- [49] Ng, W., Patil, M., and Datta, A., "Hydrogen Fuel Cell and Battery Hybrid Architecture for Range Extension of Electric VTOL (eVTOL) Aircraft," *Journal of the American Helicopter Society*, Vol. 66, 2021.
- [50] Colozza, A. J., "Hydrogen Storage for Aircraft Applications Overview," Nasa/cr-2002-211867, September 2002.
- [51] Sridharan, A., Govindarajan, B., and Chopra, I., "A Scalability Study of the Multirotor Biplane Tailsitter Using Conceptual Sizing," *Journal of the American Helicopter Society*, Vol. 65, 01 2019.
- [52] Gorton, S., Yamauchi, G., Johnson, W., and Zakrajsek, J., "Fundamental Aeronautics, Subsonic – Rotary Wing Reference Document," May 26 2006.
- [53] Sorbothane Inc., "Sorbothane Isolation Rings," 2024.
- [54] Office of the Federal Register, "Part 23 – Airworthiness Standards: Normal Category Airplanes," <https://www.ecfr.gov/current/title-14/chapter-I/subchapter-C/part-23>, Dec 30 2016.
- [55] Robinson Helicopter Company, "R66 Pilot's Operating Handbook - RTR 661," Oct. 2010.
- [56] Currawong Engineering, "Datasheet CE370.d02 - Mini High Pressure Fuel Pump," Feb. 2024.
- [57] Federal Aviation Administration, "Sec. 23.971 – Fuel Tank Sump," May 6 1993.
- [58] Optibelt GmbH, Corveyer Allee 15, 37671 Höxter, Germany, *Optibelt Technical Manual: V-belt Drives*, 2023.
- [59] Townsend, D., *Dudley's Gear Handbook*, McGraw-Hill, 1992.
- [60] Budynas, R. and Nisbett, K., *Shigley's Mechanical Engineering Design*, McGraw-Hill Education, 2010.
- [61] American Gear Manufacturer's Association, Alexandria, Virginia, *ANSI/AGMA 2005-D03, Design Manual for Bevel Gears*, 2003.
- [62] Carpenter Technology, "CarTech ACUBE 100 Alloy," 2020.
- [63] F., H. G. and Bossler Jr., R. B., "Advanced Rotorcraft Transmission (ART) Program - Final Report," Nasa contractor report 191057, 1993.
- [64] Radzevich, S. P., *Dudley's Handbook of Practical Gear Design and Manufacture, Second Edition*, CRC Press, Taylor & Francis Group, Boca Raton, Florida, 2012.
- [65] Jocher, G., Chaurasia, A., and Qiu, J., "Ultralytics YOLO," Jan. 2023.
- [66] Langlois, R., "Ship flight deck motion parameters for ensuring safety of helicopter operation," *Mississauga: Indal Technologies Inc*, 2003.

- [67] Britcher, V., Shastry, A., and Chopra, I., “Exploration of Feature-Based Algorithm for Autonomous Ship-Deck Landing under Visually Degraded Conditions,” *79th Vertical Flight Society Annual Forum*, West Palm Beach, Florida, May 16–18, 2023.
- [68] Britcher, V., Chopra, I., and Datta, A., “Development and Validation of 3D Feature-Based Vision Algorithm for Autonomous Ship-Deck Landing,” *80th Vertical Flight Society Annual Forum*, Montreal, Quebec, Canada, May 7–9, 2024.
- [69] Fasano, G., Accado, D., Moccia, A., and Moroney, D., “Sense and avoid for unmanned aircraft systems,” *IEEE Aerospace and Electronic Systems Magazine*, Vol. 31, No. 11, 2016, pp. 82–110.
- [70] Federal Aviation Administration, “FAR Part 23 Sec. 23.1353 — Storage battery design and installation,” 2009.
- [71] Pitt, D. M. and Peters, D. A., “Theoretical Prediction of Dynamic-Inflow Derivatives,” *Vertica*, Vol. 5, No. 1, Mar. 1981, pp. 21–34.
- [72] Saetti, U. and Horn, J. F., “Load Alleviation Control Design Using Harmonic Decomposition Models, Rotor State Feedback, and Redundant Control Effectors,” *American Helicopter Society 74th Annual Forum Proceedings*, May 14–17, 2018.
- [73] Prouty, R. W., *Helicopter Performance, Stability, and Control*, Krieger Publishing Company, Inc., 1st ed., 1986.
- [74] Padfield, G. D., *Helicopter Flight Dynamics: Including a Treatment of Tiltrotor Aircraft*, John Wiley Sons, 3rd ed., 2018.
- [75] Horn, J. F., “Non-Linear Dynamic Inversion Control Design for Rotorcraft,” *Aerospace*, Vol. 6, No. 3, 2019.
- [76] Saetti, U., Rogers, J. D., Alam, M., Jump, M., and Cameron, N., “Dynamic Inversion-Based Flare Control Law for Autonomous Helicopter Autorotation,” *AIAA SciTech Forum*, San Diego, CA, Jan 3-7, 2022.
- [77] European Aviation Safety Agency, *Certification Specifications for Large Aeroplanes, CS-25*, European Aviation Safety Agency, Cologne, Germany, amendment 3 ed., September 2007.
- [78] Wang, L., Dai, Y., and Yang, C., “Gust Response Analysis for Helicopter Rotors in the Hover and Forward Flights,” *Hindawi Shock and Vibration*, June 2017.
- [79] Ffowcs Williams, J. E., Hawkings, D. L., and James, L. M., “Sound Generation by Turbulence and Surfaces in Arbitrary Motion,” *Philosophical Transactions of the Royal Society of London. Series A, Mathematical and Physical Sciences*, Vol. 264, No. 1151, 1969, pp. 321–342.
- [80] Farassat, F., “Linear Acoustic Formulas for Calculation of Rotating Blade Noise,” *AIAA Journal*, Vol. 19, No. 9, 1981, pp. 1122–1130.
- [81] Brooks, T., Pope, D., and Marcolini, M., *Airfoil Self-Noise and Prediction*, Vol. 1218, National Aeronautics and Space Administration, Office of Management, Scientific and Technical Information Division, Washington, DC, 1989.
- [82] Harris, F. D. and Scully, M. P., “Rotorcraft Cost Too Much.” *Journal of the American Helicopter Society*, Vol. 43, No. 1, Jan. 1998, pp. 3–13.
- [83] Harris, F. D., “Introduction to Autogyros, Helicopter, and Other V/STOL Aircraft,” NASA-SP 2012-215959, Oct 2012.

